POROSITY IN GRAPHITES

Thesis submitted

for the

degree of

Doctor of Philosophy

at the

University of Newcastle upon Tyne

by

MARGARET EVANS (B.Sc)

November, 1978.

VOL I

TO

GEOFF

ABSTRACT

Graphite is a porous material with a complex porous structure. It is used as a moderator in nuclear reactors and as such undergoes radiolytic oxidation in carbon dioxide. The main objective of this study is to measure, quantitatively, the changes in the pore shapes and sizes which occur during this radiolytic oxidation.

Methods of pore measurement are assessed. Quantitative methods include photogrammetry which is the analysis of stereopairs (in this study, stereo-micrographs) and stereology which is the development of three-dimensional space from two-dimensional sections made through a material. Microscopic methods including optical, scanning electron and high-resolution scanning electron microscopy are used to study pores of diameters from ~500 μm to 5 nm. Optical and scanning electron microscopy coupled with the "Quantimet 720 Image Analysing Computer" proved to be the best techniques for the study.

Optical microscopy coupled with the Quantimet 720 enables the size-distributions of macropores and their shape factors to be measured before and after oxidation.

By studying the same area of polished surfaces of graphites, using optical microscopy and scanning electron microscopy, the optical texture can be correlated with the surface topography induced by gasification in carbon dioxide and air. Fizzures develop in directions parallel to the basal planes in flow-type anisotropy, but near-circular pores develop in positions of mozaics. However, similar forms of optical texture behave similarly when oxidised with molecular oxygen, carbon dioxide and atomic oxygen to comparable weight losses.

A comparison of radiolytic oxidation and thermal oxidation, using scanning electron microscopy, of Lima graphite to about 9% weight loss, shows that during radiolytic oxidation pores between 10 μm and 20 μm develop evenly over the surface whereas during thermal oxidation, pores between 50 μm and 150 μm in diameter develop in some areas, while other areas remain non-porous.

Progressive polishing of graphites is a new approach to the study of porosity in three-dimensions. This is carried out using scanning electron microscopy. The surface is polished and overlapping scanning electron micrographs are

taken to build-up a photo-montage of each polished section. The pore shapes of each section can be drawn out on transparent sheets and placed on top of each other so enabling the tortuosity and the interconnections of the pores in three-dimensions to be measured.

ACKNOWLEDGEMENTS

I would like to acknowledge the U.K.A.E.A. (Springfields) for financial support which enabled me to carry out this investigation and Professor D. H. Whiffen, Hon. Director of the Northern Carbon Research Laboratories for his support which enabled me to study in his Department.

I would like to express my sincere thanks to Dr. H. Marsh, who advised and encouraged me throughout my research at the University of Newcastle upon Tyne.

For the preparation of this Thesis, my thanks go to Miss B. Clow and Mrs M. Poad for the typing and Mrs. P. Wooster for help with the diagrams. I thank the staff of the Electron Optical Unit for help with electron microscopy, my colleagues in the Northern Carbon Research Laboratories for helpful discussions and Mr. A. Stacey (B.C.R.A. Chesterfield) for his help with the Quantimet analyses.

CONTENTS

CHAPTER 1

THE MECHANISM OF FORMATION AND STRUCTURE OF POLYCRYSTALLINE GRAPHITES.

1.1. Crystallographic Structure of Graphite.

The structure of single-crystal graphite was deduced by Bernal[1] from X-ray diffraction studies. The structure consists of flat parallel layers of regular hexagons made up of carbon atoms, in an ABABA... stacking sequence (Figure A1(a)). This gives to the graphite a hexagonal unit cell. The interatomic spacing within a graphite sheet is 0.142 nm and the interlayer spacing is 0.335 nm. The bonds in the layer plane (or basal plane) are co-valent, σ- and π- bonding, with the basal planes being held together by the relatively weak van der Waals bonding.

Figure A1 also shows a second structure found in graphite, i.e. the rhombohedral structure[2]. In this configuration the carbon layers are arranged in an ABCABC... stacking sequence (Figure A1(b)). The rhombohedral structure accounts for extra diffractions found during electron diffraction studies of graphite[3]. Some natural graphites contain as much as 30% of the rhombohedral form. Mechanical treatment, e.g. grinding[4], can increase the proportion of the rhombohedral form in a well-crystallized graphite. With continued grinding, Bacon[5] found a

steady deterioration in the crystalline perfection of both natural and artificial graphites. The rhombohedral form is thermodynamically unstable; above 1700 K it is converted to the stable hexagonal structure. This conversion may, however, not be complete until about 3000 K[6]. This accounts for the fact that the rhombohedral structure is almost always completely absent in synthetic polycrystalline graphites. Chemical treatments can also alter the relative proportions of the rhombohedral to the hexagonal form. Treatment with a mixture of hot concentrated nitric and sulphuric acid rearranges successive layers[7], and reduces the rhombohedral structure to the hexagonal form. This treatment involves no appreciable loss of carbon; therefore the layers of carbon must become mobile in strong acid and move to new positions with respect to neighbouring layers.

Graphite is never obtained in a perfect defect-free form[8]. Dislocations, stacking faults, vacancy and interstitial defects[9] occur in graphitic materials. The structures of these defects have been reviewed in detail by Amelinckx et al.[10]. The presence of stacking faults can be deduced from X-ray studies[2]; the structure of these faults and their relation to dislocations has been studied by electron microscopy[11, 12].

Simple stacking faults can be classified according to the number of violations of the stacking rule[10]. More complicated ones are combinations of the simple types.

Type I can be represented by:

abab<u>ac</u>aca... or ab<u>abc</u>bcbc...

This contains one triplet of layers in the rhombohedral arrangement and is generated by removing part of a single sheet and closing the gap.

Type II can be represented by:

<u>abab</u><u>c</u>acac... or <u>aba</u><u>cb</u>cbc...

This contains two overlapping triplets of layers in the rhombohedral arrangement, and is generated if one crystal part is shifted with respect to the other part such that a <u>b</u> or an <u>a</u> layer is shifted into a <u>c</u>-position, <u>i.e</u>. it is a single slip motion.

Type III can be represented by:

<u>ababc</u><u>a</u>bab... or <u>aba</u><u>cb</u>abab

This contains three overlapping triplets of layers in the rhombohedral arrangement and is generated if a single sheet is inserted in the normal sequence, either between <u>b</u> and <u>a</u> or between <u>a</u> and <u>b</u> layers.

Dislocations in graphite can be considered as two types; basal dislocations and non-basal dislocations. Basal dislocations are responsible for glide between successive layer planes in directions parallel to the layers. This type of dislocation usually includes stacking faults[10]. Basal dislocations

do not involve breaking the strong covalent bonding, but only the weak van de Waals bonding between the layer planes. Non-basal dislocations, e.g. screw dislocations, edge dislocations, have very low mobility, since their movement would require the breaking and restoring of the covalent bonds. Optical surface studies[13] suggest the existence of these dislocations intersecting the c-planes.

1.2. Graphitizing and Non-graphitizing Carbons.

Graphitizing and non-graphitizing carbons form two distinct, well-defined groups. If, upon heat-treatment to above 2000 K the structure of the carbon partially develops the three-dimensional structure of graphite as distinguishable by diffraction studies, then the carbon is a graphitizing carbon. Otherwise it is a non-graphitizing carbon.
(Note: these non-graphitizing carbons can develop graphitic 'crystallites' (nm in size) at 3000 K, but these 'crystallites' do not give rise to three-dimensional diffractions[14].

The term 'crystallite' has been used quite generally in the literature and its meaning needs a few words of explanation. Many methods have been used to study the structure of carbonaceous materials, such as, optical microscopy to analyse optical texture, electron microscopy and phase-contrast electron microscopy to analyse the relative arrangements or positions of constituent molecules, electron and X-ray diffraction methods and the more theoretical methods, e.g. electrical resistivities

and magnetic susceptibilities. All these methods can be interpreted to derive models of structures of graphitic materials and measurements of the structural modules. When comparing various methods there are considerable discrepancies in the sizes of the structural modules in the structural model. These are often called 'crystallites', implying the smallest regular unit of structure in the system. In optical microscopy, the 'crystallite' size of the optical texture is micrometres in size, whereas in X-ray diffraction the 'crystallite' size is in the nanometer range. In phase-contrast electron microscopy the 'crystallite' size can be smaller (hundreds of picometres). However, the most powerful of the analytical tools, i.e. the phase-contrast electron microscope suggests that the term 'crystallite' has really no reality as such in carbonaceous materials. It is not an identifiable constituent which is detected and measured by independent analytical methods. Dimensions given to a 'crystallite' are dependent on the method of analyses and interpretation of data. The term 'crystallite' is perhaps a theoretical term, having no existence as envisaged by the model.

Franklin[15] investigated the structure of carbons of different origins treated at temperatures between 1300 K and 3300 K, by X-ray diffraction techniques. She classified graphitizing and non-graphitizing carbons on the basis of

the structural differences, apparent from the earliest stages of carbonization. Franklin attributed these structural differences mainly to the formation at low temperatures, in the non-graphitizing carbons,of a strong system of cross-linking uniting the 'crystallites', leading to a random orientation of the 'crystallites' into a rigid, finely porous material. In the graphitizing carbons the cross-linking was much weaker, the structure more compact and neighbouring 'crystallites' had a tendency to lie in nearly parallel orientations. It is now possible to be rather more precise about these original, basically correct ideas of Franklin (see Section 1.5).

Mrozowski[16] also classified carbon into the two broadly equivalent groups; 'soft' carbons (graphitizable) and 'hard' carbons (non-graphitizable), according to the high or low order in arrangements of 'crystallites' on a microscopic scale, i.e. dimensions of namometres rather than micrometres. Soft carbons are usually formed from organic materials which melt on heating and solidify at temperatures above 673 K whereas hard carbons are formed from organic materials which do not melt at all (polymers) or which solidify at low temperatures.

Kipling et al.[17, 18] extensively studied both graphitizable and non-graphitizable carbons prepared from a wide range of

polymeric materials. They found that fusion during carbonization was necessary for the formation of graphitizable carbon. The fused stage allows mobility of constituent molecules which enables planar molecules to align in approximately parallel layers, giving an ordered structure which can readily be graphitized at higher temperatures[18]. Kipling and Shooter[18] carried out studies using polarized light microscopy and found that graphitizable carbons contain regions of anisotropy, whereas the non-graphitizable carbons do not contain regions of anisotropy. The presence and absence of anisotropy using optical microscopy provides a method of distinguishing between graphitizable and non-graphitizable carbons.

1.3.Origins of Graphitizable Carbon.

The suggestions of Franklin[15] and Mrozowski[16] imply that the graphitizability of a carbon must be controlled by the processes occurring during the early stages of carbonization of the parent material. A graphitizing carbon is formed when the temperature range for the occurrence of pyrolysis (often dehydrogenative polymerization) (usually about 673 K to 773 K) coincides with the fluid range of the material undergoing pyrolysis. This often occurs during the carbonization of aromatic hydrocarbons[19] and pitch materials derived from petroleum and coal-tar as well as other model compounds[20].

During the carbonization of pitch the chemistry of pyrolysis provides for a continuous increase in molecular weight (size) within the pyrolyzing system. When such a carbonization is monitored using a hot-stage in conjunction with polarized light optical microscopy[20], initially, the pitch possesses the properties of an isotropic liquid and its surface appears purple when the polarized light is used with parallel polars and a half-wave retarder plate placed in the reflected beam. At a heat-treatment temperature (HTT) between 670 K and 720 K (~ 400 to 450°C) a new phase appears from within the isotropic liquid. This phase is anisotropic, i.e. exhibits optical activity, and is coloured (yellow and blue) when viewed in the microscope (Section 1.4). This new phase, termed the mesophase, is plastic and must be considered the precursor to the anisotropic semi-coke.

To explain the origins of this mesophase it is necessary to re-examine the chemistry of pyrolysis of the pitch system. It would appear that in this situation molecular weights increase by both inter-and intra-molecular reactions from about 200 to 300 amu to 1000 to 2000 amu. Such large molecules would normally be considered 'insoluble' in the original solvent and a process of precipitation would be anticipated. This is essentially what happens in this pitch system except that the 'precipitate' has rather unusual properties. The increasing pyrolysis (carbonization)

temperature promotes a continuous increase in molecular weight to produce large molecules with a planar shape. At a critical concentration these molecules interact, flat surface to flat surface, to form a stable phase quite different from the parent pitch material. This new phase grows at the expense of the surrounding isotropic material to form ultimately an anisotropic solid which is a graphitizing carbon. But, before reaching the stage of a solid carbon, this anisotropic mesophase can exhibit properties of considerable fluidity.

The mesophase in its initial stages can be present as spheres with the constituent lamellae aligned perpendicular to the sphere surface[21] (see Figure A2). But it must be stressed that spherical mesophase arises only because of the low viscosity of the carbonizing system. There is no other significance. In systems of high viscosity the mesophase is not spherical.

The mesophase forms via a lamellar, nematic liquid-crystal[22]. This is a very important new concept and explains many of the structural characteristics of the resultant anisotropic carbons[20, 22, 23].

These liquid crystals are physical in nature with no chemical bonds between the lamellar molecules as stacked into a parallel preferred orientation. Lewis[20] has demonstrated that

this phase is physical rather than chemical in composition. He grew anisotropic spheres from a petroleum pitch very slowly at minimum temperatures. These anisotropic spheres 'dissociated' following a rapid, but small increase in temperature (5 K) and reappeared on cooling. The initial step is therefore a purely physical "phase change". The formation of the lamellar nematic liquid-crystal probably originates with the high enthalpies of physical adsorption which are possible when two large lamellar molecules 'come together', flat surface to flat surface.

It is considered that the development of this anisotropic, lamellar, nematic liquid-crystal is insensitive to the detail of chemical composition of molecular constituents, but is very sensitive to size and shape (i.e. essentially lamellar) of these constituent molecules. As the liquid-crystals are essentially a physical, rather than a chemical entity, a critical size/shape factor is necessary to ensure sufficient "physical adhesion" between molecules resulting from van der Waal's forces with some polar interactions to overcome the disruptive, dissociative effects of kinetic and vibrational energies of molecules resulting from the progressive increase in HTT of the system.

The large planar molecules (formed during the pyrolysis of the pitch) associate with anisotropic parallel stacking (but with no vertical registry), to create a new phase, i.e. the lamellar,

nematic liquid-crystal, which contains the structural order which leads directly to a graphitizable carbon. But, once having been formed by an essentially physical process, then chemical processes within the liquid-crystals soon become dominant and dictate subsequent events.

Those same processes which lead to the increased molecular weight and size in the pitch system, by being both time and temperature dependent, as are rates of chemical reactions, now promote bonding and chemical-linkage between the lamellar constituent molecules, either edge-on or across the planes. The extent of this 'cross-linkage' increases with time and temperature to produce a three-dimensional, aromatic polymer of increasing viscosity leading eventually to the non-plastic coke substance. This polymeric material is termed "THE MESOPHASE". Thus, a distinction can be made between the lamellar nematic liquid-crystal and mesophase.

Mesophase from different parent materials possess different viscosities and different dependencies of viscosity with temperature. It is the viscosity, itself controlled by molecular size and reactivity which controls the ability of the growth units of mesophase (spherical or otherwise) to grow beyond a certain size and eventually, when they are large enough

to touch each other, to coalesce into each other such that the individual growth units lose their original identity. It is here that there are major differences in the properties of the mesophase from different pitches. The anisotropic structure referred to as the optical texture (Section 1.4) formed within the graphitizable carbon, depends on the type of growth of the mesophase and its subsequent coalescence characteristics. For instance, a Gilsonite pitch will produce small anisotropic units of mesophase (<5 μm diameter) which on contact only 'adhere' together where they touch such that their original identity is not lost. (The mode of this adherence is not understood in detail). These growth units thus are the origins of the mozaic optical texture (Section 1.4) seen in polished surfaces of the carbon by optical microscopy and preserved from the semi-coke stage of carbonization to the graphitic stage in Gilso-carbons. However, Ashland A200 petroleum pitch grows larger units of mesophase (~25 μm diameter) which, on contact, coalesce into each other with total loss of original identity and create an optical texture of large, isochromatic domains, hundreds of micrometres in size. (In one sense, these mozaics or domains are a measure of the macro-crystallinity of the carbon).

These growth characteristics of mesophase are influenced by properties of the parent material such as the size, structure

and chemical reactivities of the molecules present in the starting materials, the rate of carbonization and the 'soak' temperature and time. The plasticity of the mesophase being a function of temperature of carbonization as well as shape, size and reactivity of constituent molecules, also affects the coalescence characteristics, together with any additional physical parameters such as applied pressure, bubble percolation caused by evolution of volatile materials and thermal convection currents.

The study and understanding of the mesophase[23, 24] has widened our knowledge considerably of the formation of graphitizing carbons. Different relative degrees of chemical polymerization within the lamellar, nematic liquid-crystals account for variations observed in optical textures of carbons. Marsh et. al[25, 26, 27, 28] carried out extensive studies of the origins in terms of liquid-crystals, of the many different optical textures of mesophase formed from coals, pitches and organic model compounds. It is emphasized that mesophase is the intermediate phase between the transitory liquid-crystal and the semi-coke. Also, when the anisotropic components of the carbonization system become visible in optical microscopy (about 0.5 μm in diameter) these components are essentially the polymeric mesophase material. They are, of course, present before

their detection by optical microscopy and can be detected (in size < 0.5 μm) by electron microscopy. The experiments of Lewis[20] who demonstrated the reversibility of formation of the anisotropic phase in heated pitch are of a very specific nature, being isothermal, as distinct from the progressive heating of usual carbonization systems.

1.4. Origins of Optical Texture.

When carrying out studies on graphitic materials, a most useful piece of equipment to have is a reflecting polarized light optical microscope. When polarized light reflected from the polished surface passes through a crossed-polarizer, called an 'analyzer', then isotropic materials appear black and anisotropic carbonaceous materials exhibit dark bands running across light areas. These dark bands are called 'extinction contours' and move on rotation of the stage of the microscope. It is possible, by rotation of the microscope stage and making a photographic record of the surface, to map out these contours so producing a lamelliform structure of the graphitic material[24, 29].

If the microscope is fitted with a half-wave retarder plate which is placed in the path of light reflected from the polished surface of the specimen before the analyzer, then a series of interference colours[30], can be obtained across the surface.

Isotropic materials appear purple and anisotropic materials appear yellow, blue or purple depending on the orientation of the graphitic layers relative to the plane of the polarized light[31]. With a parallel setting of the polarizer and analyzer of the microscope, and a known setting of the half-wave retarder plate, the colours of yellow and blue can be interpreted, (see Figure 1). This means, e.g. that within the areas coloured yellow the planes of the graphite structural unit are arranged East-West (E-W), prismatic edges only are projected at the surface, not basal planes. Within areas coloured blue the planes of the graphite structural unit are arranged North-South (N-S). Purple colours are also exhibited when basal planes compose the surface of the polished structural unit.

The polished surface therefore appears as a series of coloured areas of varying shapes and sizes, merging into each other. These variations in shape and size are caused (or determined) primarily by the pyrolysis chemistry of the parent materials (as discussed above and below) and, to a less degree, by manufacturing procedures. These isochromatic areas, i.e. areas of a single colour, are referred to as the optical texture. The analysis and description of the optical texture is considered of major importance in assessing the properties of the material under examination. The size of the isochromatic

areas on the surface can range from <0.1 μm to 500 μm and different terms are used to describe different size ranges. Isochromatic areas of size 0.1 μm to 5 μm are termed 'mozaics' and areas of size 5 μm to 500 μm are termed 'domains'. These terms have divisions of fine, medium and coarse, within the size ranges. Some of the domains have elongated structures and are known as 'flow-type anisotropy'.

Experience in the use of optical microscopy permits one to distinguish between two types of contact or relationship between isochromatic areas. One type, probably the most easy to detect, is essentially a boundary between two particles, i.e. the structure in non-continuous. The second type of boundary between contact areas is a continuous situation where the orientation of the lamellar of the graphite undergoes a significant change, relative to the optic axis of the microscope (a convenient reference standard). The change in orientation can be extensive over short distances and is to be associated with what are called disclinations[32]. These defect structures have their origins in the growth process of anisotropic substance from the liquid phase of the parent pitch.

Hence, optical microscopy in terms of optical texture reveals detailed information of the size, juxtapositioning, orientation and defect structure associated with the macro-crystalline components

of graphite. Macro-crystalline is a term to describe the isochromatic areas of optical texture which contain lamellae stacked in an approximately parallel orientation (tertiary structure). Within these isochromatic areas exist micro-crystallites (< 0.1 μm in size) or more discrete graphite crystals (secondary structure) such as are detected and measured (by line-broadening) by X-ray diffraction methods. Even within these micro-crystallites, there exists detail of molecular ordering and mis-alignment (primary structure).

Hence, the measure of crystallinity of a graphite, is, in one important sense, determined by the experimental procedure used to measure the crystallinity.

1.4.1. Causes of Differences in Optical Texture.

Cokes which have an optical texture made up of small mozaics, as from a Gilsonite pitch, are considered to be formed from a pyrolysis system in which the growth units of mesophase have not been able to grow beyond a few micrometres or to coalesce on contact. It is probable that within such materials polymerization occurs within these units at a relatively early stage of the carbonization process to a significant extent across the planes of stacking (in the c-axis of the lattice). This type of cross-linkage in the c-axis is directly attributable to the chemical reactivity associated with the chemical composition

of such molecules. For example, pyrolyzed Gilsonite pitch is still essentially non-aromatic; the molecules will not be made up of in-plane, complete aromatic rings but of partially hydrogenated six-, seven- or eight- membered ring systems with methylene or other linkages and heteroatoms, and may adopt buckling or folding with projecting side-groups, e.g. alkyl, hydroxyl[33].

This cross-linkage in the c-axis and other forms of polymerization of the mesophase from a Gilsonite pitch effectively restrict slip of plane over plane so that at an early stage of carbonization coalescence involving the plasticity and flow of the mesophase is not possible.

The mesophase on growth from the pitch cannot adopt a spherical shape but hence adopts the observed irregular shape[33]. (N.B. the surface energy available is not sufficient to create a spherical shape). Further, growth by adoption or squeezing-in of molecules from the liquid phase with the resultant yielding or growth of the mesophase to accommodate new molecules is not possible. The size of the growth units therefore remains small and a relatively high density of nucleation centres results (another characteristic of mesophase growth from a Gilsonite pitch).

Cokes which have an optical texture made up of large isochromatic domains are considered to be formed from a pyrolysis system, more homogeneous in chemical composition, in which the molecules are relatively more planar and aromatic. With e.g. Ashland A200 petroleum pitch, once the lamellar molecular products of pyrolysis are orientated by the formation of the liquid-crystal phase, then subsequent polymerization within the nematic liquid-crystal appears to be predominantly between the edges (in-plane) of the molecules to establish larger sheets, stacked above and below each other. This polymeric, plastic deformable mesophase, like the conventional liquid-crystals[34], has quite unique flow properties, quite different from liquid and other polymeric phases. These unique properties of flow are responsible for the structure seen in optical textural analyses of cokes made from such material. This structure is defective in terms of crystal perfection; the nature of the defects being characterized and recognizable in terms of the properties of conventional liquid-crystals.

Thus, these flow properties allow the initially spherical growth units of mesophase to coalesce into larger spherical units without (unexpectedly) the serious disruption of the lamellar stacking sequences within the spheres. The original ordering of arrangement of molecules of the liquid-crystal is accordingly perpetuated. At the point of complete conversion of pitch substance to mesophase, the units of mesophase finally

coalesce to form the larger isochromatic domains. Here, some distortions are introduced because of some loss of facility of movement to relax the distortions of coalescence. These distortions are again quite specific to liquid-crystal systems, and exhibit an identifiable series of bends, folds, twists, and flow patterns, to establish the disclinations, domains and flow-type anisotropy as seen in the optical textures of Ashland A200 petroleum pitch.

Hence, the shape/size of molecular constituents of carbonizing systems are probably the important parameters controlling liquid-crystal formation. But, it is the detailed chemical composition and resultant chemical reactivity which then control subsequent growth and coalescence so establishing the optical texture which, in turn, influences the development of porosity in resultant graphitic material.

The chemistry is quite specific and must allow two functions. One is the dehydrogenative polymerisation of some of the constituent compounds of the pitch to establish the liquid-crystals. The second is the stability of other constituents to maintain the solvent in which the lamellar molecules move in order to orientate themselves to form the liquid-crystals.

1.5.Mechanisms of Graphitization.

The process of graphitization essentially is the development of an ordered crystallographic structure from an initially disordered carbonaceous substance. In general, the initial disordered carbon is not completely devoid of crystallographic order. The term 'amorphous carbon' is erroneous and should be avoided. There is significant organization of the carbon into graphitic-like sheets, (i.e. from the mesophase as discussed above) but the ordered stacking arrangement of the layers, as in graphite, is not present.

In one sense, graphitization i.e. the perfection of structure in carbon, takes place between 700 K (the temperature of its formation) and the highest of attainable temperatures, i.e. about 3300 K. There are many variables which condition the transformation of carbon to graphite, the principal ones being the heat-treatment temperature, heating rate, duration at the maximum temperature, applied mechanical pressure, the presence of graphitization catalysts and the pressure of the gas surrounding the sample during heat-treatment[35].

Workers studying graphitization mechanisms have approached the problem from different view-points. Franklin[36] first described the structural transformations undergone by graphitizable carbons during graphitization. She stated that graphitized carbon is

formed from disordered stacks of graphitic atomic layers, graphitization being simply a form of annealing, leading to an ordered arrangement of the layers amongst themselves. This concept depended essentially on the assumption that the elementary layers were perfect and their structure did not change throughout the process of graphitization. This theory is now known not to be correct (see below). The movement of whole layers cannot be accepted.

Maire and Mering[37] reconsidered Franklin's model when they carried out bromine sorption experiments on graphitizable carbons. These experiments suggested that the graphitization process takes place essentially through the perfection of the internal structure of each layer with the removal of interstitial carbon atoms; the rearrangement and the creation of three-dimensional spacing would be only a secondary consequence of this elementary transformation.

Pacault and co-workers[38] studied the kinetics of graphitization by measuring such parameters as the interplanar spacings, magnetic susceptibility, magnetic anisotropy and the degree of graphitization, and suggest that graphitization takes place by a step-wise process. This step-wise process is evident when one of the above parameters is plotted as a function of heat-treatment time.[35] However, discussions with other workers in

this field of study casts doubt upon the graphitization process being step-wise, that type of curve being an artefact of method and error in measurement. It is perhaps more logical to accept a continuous change.

Fischbach[39] reviewed the kinetics and mechanism of graphitization and states that at temperatures above 2300 K, the graphitization process in graphitizable carbons is a thermally activated kinetic process which proceeds isothermally to conclusion, given sufficient time, without the aid of catalysts. He also states that there is available evidence which strongly suggests that a vacancy mechanism parallel to the layers plays a dominant role. However, some evidence suggests that diffusion normal to the layers occurs by an interstitial mechanism with an activation energy similar to that for the vacancy mechanism. Fischbach[39] does not rule out the fact that defects, which may be specific interstitial defects or interlayer and inter-crystallite defects[40] may be eliminated during the graphitization process. This is quite feasible because the structure of graphitizing carbons is such that only a small proportion of the atoms in the disordered carbon must be rearranged to produce the parallel stacking of graphite. However, gross defects i.e. disclinations[34], which can be observed in the optical microscope in graphitizing carbons, cannot be removed

by heat-treatment. Graphitization does not produce single crystal graphite. Therefore, the optical texture of the carbon does not change on graphitization. Probably one observes only a sharpening of the intensity of the colours. The size of the optical texture and the analysis of the disclination structures are therefore important in governing the extent of polycrystallinity of a carbon[23]. Shrinkage takes place during graphitization, producing cracks which alter the pore structure of the graphite, this being another factor limiting the formation of single crystal graphite.

The mechanisms of graphitization for a graphitizing and a non-graphitizing carbon (if possible) are quite different. With non-graphitizing carbons, a complete re-organisation of the entire matrix is required rather than just a rearrangement of carbon atoms in order to remove defects as in graphitizing carbons. This complete re-organisation can only be brought about by catalysts. Most studies of catalytic graphitization have been carried out using non-graphitizing carbons. Marsh and Warburton[41] reported that the detailed mechanism of the catalytic graphitization varies with the catalyst and the carbon.

1.6. Manufacture of Graphite.

Synthetic graphites vary a great deal in their optical texture, density, electrical resistivity, mechanical strength and pore size distributions. This is because graphites have

many uses and the detail of their specification is controlled by the mode of manufacture and the source materials used for manufacture. Most manufactured graphites contain (among other components) a petroleum-coke filler and a coal-tar pitch binder, and are then shaped by extrusion or moulding. It is difficult to define the compositions of graphites completely as the details of manufacture are of a proprietary nature.

Petroleum-coke is used as a filler because, amongst other things, it is easily graphitized, has a low electrical resistivity and is responsible for low values of CTE. The shapes of the petroleum-coke particles (the needle-cokes of electrode graphite) have a significant effect on the packing of the particles during manufacture. Since coke particles are irregular in shape they tend to become orientated in the extrusion process. This particle orientation leads to preferred crystallite orientation which creates a bulk anisotropy in the extruded unbaked carbons. The shapes of these particles have been studied by several workers[42, 43, 44]. Rusinko and Parker[42] obtained a correlation between porosity and shape factors for ground petroleum-coke, but stated that there were many factors, e.g. weight, orientation, packing density, which they had not studied but which should be taken into account. Although the particle shape determines, in part, the ability of particles to orientate,particles of

any given shape can be arranged in various orientations by differences in packing techniques. Amstein and Watson[44] showed a correlation between particle angularity and porosity of carbon grist particles, by measuring mean size, particle density and specific surface of the particles. The angularity is the ratio between the specific surface determined experimentally and the specific surface calculated by assuming the particles to be spherical. The greater the angularity the more the particles depart from the spherical shape.

Coal-tar pitch is the generally preferred material for use as a binder[45]. It softens at temperatures around 350 K, has a large temperature zone of plasticity, and it hardens again on cooling after the extrusion process. It has a high carbon content of approximately 93 per cent, which makes it very suitable as a binder because of high yields and the development of little porosity.

Hence, the porosity developed in a graphite manufactured from pitch and coke is related to the size/shape of the coke-grist particles, the binder properties and the mode of volatile evolution (see below for a more detailed discussion).

In the actual manufacturing process the filler and binder are mixed together at a sufficiently high temperature (~ 450 K)

to reduce the viscosity of the pitch to a level which allows it to flow freely around the petroleum-coke and for the mix to be extruded. The primary function of the mixing operation is to obtain a uniform distribution of the pitch in the petroleum-coke filler.

The mixture is then extruded or moulded, details of which have been presented[46]. During the extrusion process of the pitch-grist system, the coke-grist particles may become aligned with their long dimensions parallel to the direction of extrusion, so giving rise to a degree of pre-established bulk anisotropy (the coke-grist is already anisotropic in terms of molecular stacking). This bulk anisotropy originates from the predominant orientation of the crystallite layer planes parallel to the long dimensions of the particles (that is, in the needle-coke particles). Thus, physical properties will be affected by the alignment of particles in the extrusion process. Properties measured in a direction parallel to the aligned particles will have different values when measured in a direction perpendicular to the aligned particles. But some graphites are required with isotropic bulk properties. Hence more isometric particles are used or particles of coke with a more mozaic type of optical texture.

The moulding technique consists of compressing the filler-binder mixture in an enclosed area of the desired shape, fitted

at one, or both ends with moving plungers. In this operation, the elongated particles of filler coke align themselves with their long dimensions perpendicular to the moulding direction and orientated randomly about it (see Figure A3).

The moulded or extruded blocks are then baked. This pyrolyzes the binder, distilling off about 9% of the weight of the block, as volatile material[47]. The firing process must be carried out very carefully and is of critical importance to manufacturers. The loss of volatile material and the shrinkage of the binder takes place during this process. Baking is normally carried out at about 870 K with slow heating rates varying from 2 K to 10 K per hour[47]. Pneumatic pressure[48] used during the baking operation has been found to increase the density of the baked material. The effect of this pressure is to raise the boiling point of some of the constituents of the binder and hence, increase the relative extent of polymerization; it also creates carbon from what would otherwise be volatile matter.

After baking, an impregnation stage(s) may take place (using a pitch or resin) before the final graphitization in order to increase the density. The blocks are sealed in an autoclave which is evacuated and filled with the molten pitch, etc.. The pitch is forced under pressure into the pores of the blocks.

Graphitization is carried out at temperatures in the range of 2700 K to 3300 K. The blocks are placed in electrical furnaces which are brought up to temperature over a few days and held at the maximum temperature for a few hours. The furnace is allowed to cool until the temperature is low enough for the blocks to be safely exposed to the air.

The manufacture of graphite is a slow process. The baking stage in particular could benefit from conversion to a faster process.

1.7. Properties of Nuclear Graphite.

Nuclear graphites, used as moderators for the neutrons in nuclear reactors are polycrystalline with bulk isotropy (where possible) as distinct from single crystal material. This polycrystallinity associated with manufacturing methods gives rise to a porous system within the graphites. For use in nuclear reactors, in order to increase the density before graphitization, one or two pitch impregnations are made into the material. This material is frequently referred to as double-fired graphite, having a density ranging from 1610 to 1720 kg m^{-3} (1.61 to 1.72 g cm^{-3})[49].

During the manufacture of nuclear graphite, special care must be taken to exclude impurities, especially those with significant neutron capture cross-sections, i.e. neutrons absorbed in any reactor component are lost from the chain reaction e.g. boron. Careful selection of starting materials can eliminate the need

for purification. However, if purification is necessary, it can be carried out by treating the graphite with halogens at about 2800 K, either during graphitization, or at a later stage.

In order to select a moderator material, several moderator parameters must be compared[50]. These moderator parameters involve measurements of the loss in energy for each neutron collision in the moderator, the absorption cross-section and the scattering cross-section. The moderator parameters can be combined to give moderator properties such as the ability of a moderator to slow down neutrons (energy loss X scattering cross-section). These moderator parameters/properties are discussed in detail by Nichols and Woodruff[50].

There are two main requisites of a moderator material[50]. Firstly, it must slow down high energy neutrons produced from fission, so that they are more readily captured by fissionable material and secondly, it must have a small cross-section for neutron absorption. Graphite is used as a moderator because of its low atomic number, its low neutron cross-section and because of its purity. The slowing down of neutrons results mainly from energy transfer during elastic collisions between the neutrons and the moderator nuclei. For a material to be an efficient moderator, the collision rate per unit volume must be relatively high.

During its life as a moderator, graphite undergoes irradiation damage. Fast neutrons move freely through the graphite lattice until they collide with an atom. The atom is then ejected from its lattice site, with high energy. Irradiation damage in graphite is a very complex phenomenon, which causes changes in all the physical properties i.e. dimensions, porosity, chemical reactivity, etc., as well as raising problems in the design and and operation of nuclear reactors. Hence, the effect of radiation on graphite has been studied very extensively[51, 52, 53] in elaborate research programmes of the U.K.A.E.A. and C.E.G.B.

CHAPTER 2

POROSITY IN CARBONS AND GRAPHITES

2.1. Introduction.

The theoretical density of graphite is 2265 kg m^{-3} (2.265 g cm^{-3})[54]. All manufactured graphites have a density which is lower than this, so indicating the presence of porosity or pore volume.

The pore volume in graphite is distributed between pores ranging in diameter from about 1 nm to 500 μm. The porosity present in graphite is of two types, i.e. open and closed porosity. Open porosity is accessible to penetrating gases and liquids and is interconnecting throughout the graphite, whereas closed pores are not accessible to fluids and are not connected to the open pores. There are some pores, probably not a significant number, which are closed to gases at room temperature but which may progressively become open to gases at temperatures up to about 1300 K.

Pore sizes fall into three categories; macro-, meso- and micro-pores of diameter above 50 nm, 50 nm to 2 nm and less than 2 nm respectively[55]. In this study, we are interested essentially in macro- and meso-porosity as micro-porosity is not involved with the problems encountered during radiolytic oxidation in a nuclear reactor.

Porosity in graphite is closely associated with the structural units comprising the graphite body, hence the pores vary a great deal in both shape and size. Porosity can be formed from trapped bubbles of volatile material (irregular or spherical-shaped pores) and from macro- and micro-fizzures or shrinkage cracks. These pores are more likely to be slit- or slot-shaped and may constitute part of the open pore volume, which are made up of wide pores with narrow entrance diameters.

Extensive studies[56, 57] have provided interpretive measurements of porosity and use such methods as mercury porosimetry, surface area assessments, permeability and diffusivity, such that pore volumes and pore entrance diameters can be calculated. However, little information has been obtained quantitatively of the more difficult descriptions of pore-shapes, sizes (and their distributions) and interconnections in such porous systems as those of graphite. This thesis describes microscopic techniques to provide quantitative descriptions of pore-shapes and sizes, and also describes the use of these techniques to describe changes in porosity induced in graphites by gasification treatments.

2.2. Origins of Porosity.

Porosity in carbons and graphites does not occur by a random process, but the shape, size and distributions of porosity are

closely associated with manufacturing methods and the intrinsic properties of parent metrials as exhibited during pyrolysis of the liquid phase, and by properties of resultant lamellar nematic liquid-crystals, mesophase, green semi-coke, coke-grist and graphite.

Carbons as solids exhibit many forms (e.g. carbon blacks, chars, cokes etc). An approximate divisions of carbons as solids is into non-graphitizable and graphitizable carbons, i.e. a measure of structural change on heat-treatment to 3300 K. These two forms of carbon have different structures.

The non-graphitizable 'active' isotropic carbons and graphitized, graphitizable carbons (i.e. the synthetic polycrystalline anisotropic graphites) are both structurally heterogeneous materials with considerable porosity. This porosity originates (in part) with the mode of 'packing' of the crystallites and constituent particles. The crystallites themselves contain structural distortions (defects) in association with which are voids or pores. The micro-porosity of isotropic carbons is associated with the basic structural units of such carbons, i.e. the sheet of carbon atoms (in an imperfect hexagonal arrangement). These sheets have various sizes, and shapes and degrees of deformity from planarity. Hence, the random packing arrangement of these sheets creates a

specific micro-porosity, i.e. voids between the sheets and the shapes and sizes of the voids is a function of the shape and size of the carbonaceous sheets.

The anisotropic graphitizable carbons generally exhibit probably no micro-porosity but possess meso- and macro-porosity. Phase-contrast high-resolution electron microscopy[58] reveals the size and shape of the imperfect graphite sheets which constitute the structural units of graphitizable and non-graphitizable carbons. Imperfections in shape and planarity of the constituent units prevent parallel stacking. This accounts for the relatively low bulk densities (~1500 kg m^{-3} (1.5 g cm^{-3}) in graphitizable carbons and ~900 kg m^{-3} (0.9 g cm^{-3}) in non-graphitizable (micro-porous) carbons). Diagram 2.1. (below) shows a diagrammatic representation of the structure of graphitizable and non-graphitizable carbons showing the micro-pores between the structural units in non-graphitizable carbons. Graphites can be produced with different densities (pore volumes) with the porosity in different ranges of size.

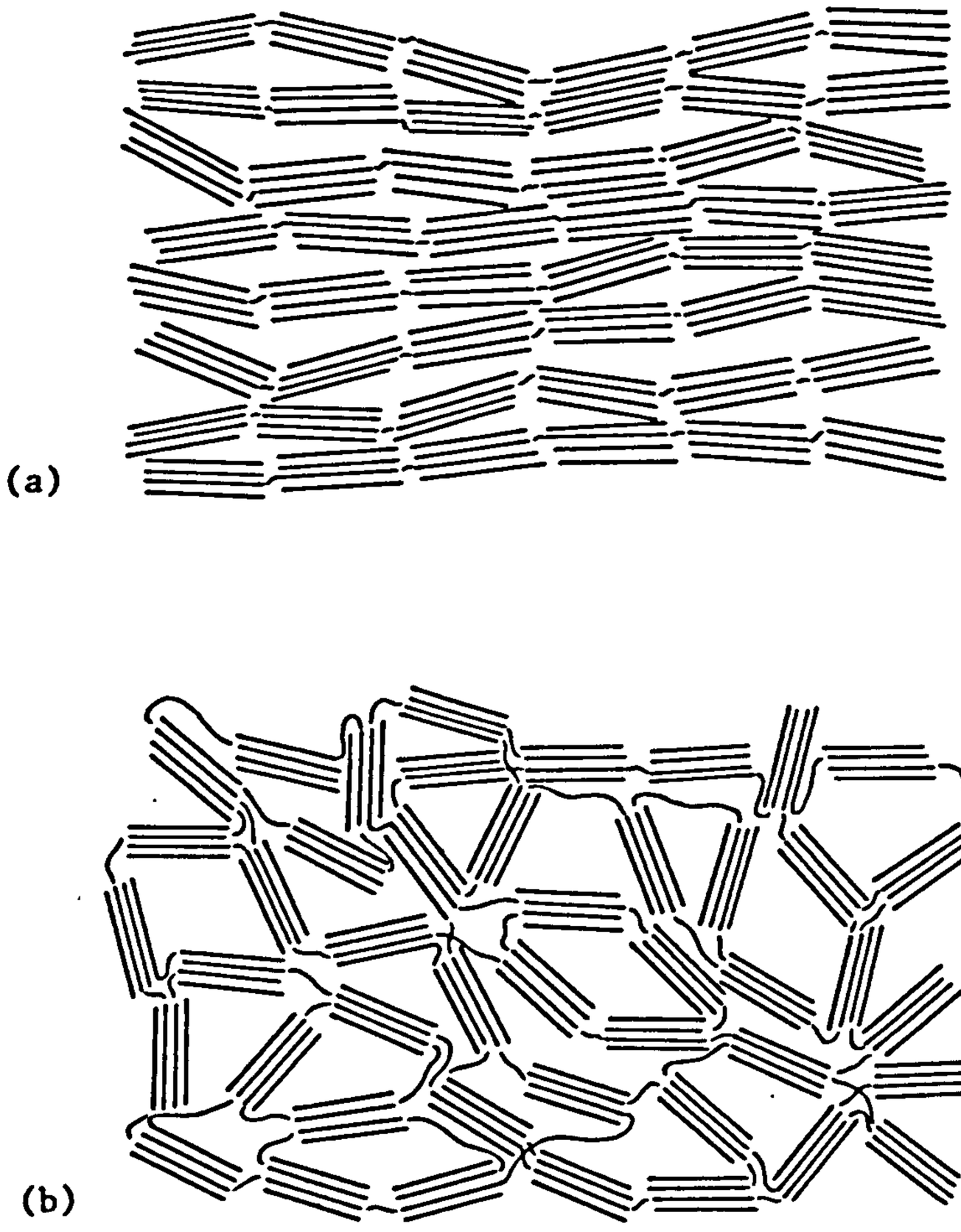

Diagram 2.1. Structure of a) graphitizable and b) non-graphitizable carbons.

2.2.1. Origins of Porosity - Graphitizable Carbon, Pitch to Mesophase Transition.

Manufacturing procedures leading initially to the formation of coke via the mesophase undoubtedly influence the size and shape of resultant porosity in graphites. The baking/carbonization process involves loss of volatile material (gases and vapours) which accumulates as bubbles within the fluid pitch. With the onset of mesophase growth within the pitch, two effects are observed:-

(1) The movement of the bubble may exert a shearing force upon the mesophase (fluid, nematic liquid-crystal, anisotropic precursor to graphitizable cokes which adjusts by adopting

a flow-type anisotropy, i.e. the optical texture is elongated to give needle-like 'crystallites'. It actually flows with the bubble and may encapsulate it.

(2) This encapsulation at a late stage of formation of mesophase may trap the bubble such that it never reaches the outer surface as volatile material but remains within the system as a pore. Convection currents within the pitch influence the shape of these bubbles which ultimately become incorporated into the graphite. Bubble size is usually >5 μm. The chemistry of pyrolysis of the chemical constituents of the pitch influences the fluidity of the pitch and this fluidity influences the size of the optical texture (macro-'crystallinity') which in turn influences the size of the porosity (within or at boundaries of 'crystallites'). Decreased fluidity implies a small size of optical texture or crystallinity'[59].

It must not be overloooked that within graphites, made by extrusion processes from conventional pitch/grist systems, the mesophase to be found there is formed from two different materials. There is mesophase made from the pitch (usually coal-tar pitch) and formed during the actual baking of the extruded rod. The second material is the coke grist. This

coke-grist (usually from petroleum pitch) is made in a delayed coker in which pre-heated pitch material is pumped into the coking unit. Here, the resultant anisotropy is dictated by the type of residue material being charged to the delayed coker and the mechanical processes of e.g. flow and volatile evolution within the coker.

Some industrial manufacturing procedures appear to manipulate these processes to establish optical textures (and hence structure) in graphites which reflect desirable commercial properties. Many are proprietary and not fully documented. As an example, inspection of Figure 3 (a Gilso-carbon graphite) shows not only the small, individual mozaics of texture, but also that these are compounded in the manufacturing process into spherules (not to be confused with the spheres of mesophase) in such a way that super-mozaics are established. Here, each mozaic is not independently orientated but forms part of a larger unit of organization within the spherule. (Note the large areas of blue and yellow mozaics).

Clearly, such porosity as is seen in a petroleum coke graphite (Figure 8) is quite different from that of the Gilso-carbon system (Figure 3). With the Gilso-carbon, there is a larger irregular central pore in the centre of the spherule and there are small

pores (< 5 μm) to be found within the mozaics. This illustrates the important point that shrinkage or other voids (i.e. porosity) have shapes and sizes which are not independent of the basic structural units of the graphites. These Gilso-carbon graphites will thus never exhibit porosity similar to the large acicular pores associated with isochromatic domains or disclinations as found in cokes from Ashland A200 petroleum pitch.

2.2.2. Origins of Porosity-Graphitizable Carbon. Mesophase to Graphite Transition.

The density of mesophase is quoted as 1460 kg m^{-3} (1.46 g cm^{-3}),[22] so that considerable shrinkage occurs during its transformation to graphite of theoretical density 2265 kg m^{-3} (2.265 g $.cm^{-3}$). This increase in density does not occur by a uniform shrinkage of the bulk of the material - the structural anisotropy prevents this. Instead, shrinkage voids, or pores, appear within the particles, not entirely at random, but in positions somewhat predictable from the optical texture.

Consider the optical texture of cokes from Ashland A200 petroleum pitch made up of isochromatic domains. Examination of the mesophase material itself (HTT 800 K, (527°C)) reveals that the shrinkage processes have already commenced at this low HTT; the optical micrograph reproduced below shows several shrinkage cracks passing through the mesophase/semi-coke material.

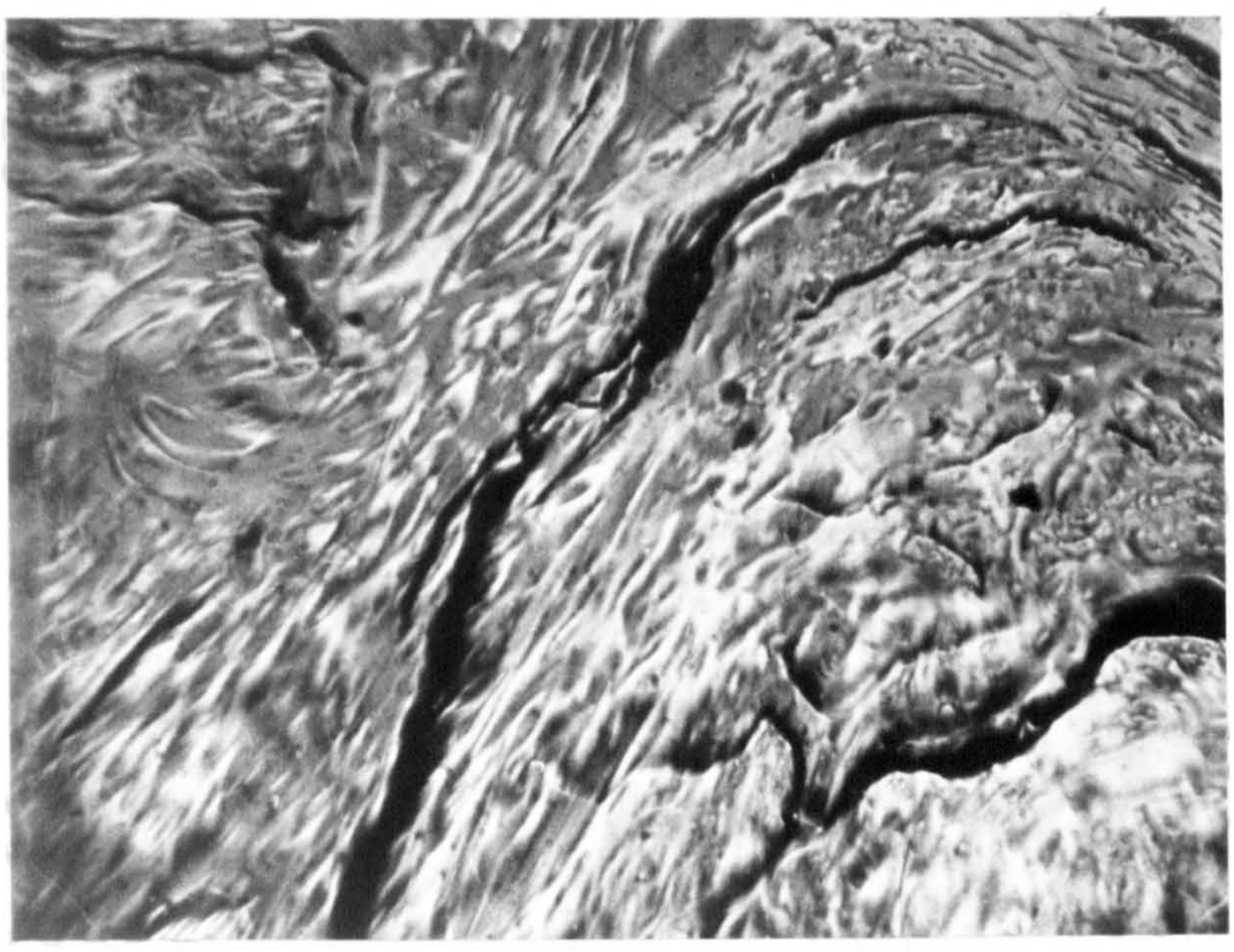

Optical micrograph of a semi-coke (HTT 800 K), from a mixture of 50% Gilsonite Pitch and 50% Ashland A200 Petroleum Pitch.

These cracks are running in directions parallel to the planes which contain the lamellar constituent molecules. As these planes bend and dip as they follow the flow-pattern of the plastic mesophase, so these shrinkage pores bend and dip as they follow the flow-patterns. The situation is most marked when the plastic mesophase has been subject to considerable shearing forces (see above) to produce '<u>thick sheets or rods</u>' of mesophase, flat, bent or twisted. Shrinkage of such material produces long, acicular cracks or voids.

Thus, the process of shrinkage introduces cracks, later recognized as porosity, the shape and size of which is a direct function of the shape and size (i.e. the macro-crystalline (tertiary) components) of the anisotropic, isochromatic constituent units of the graphite. These pores widen/develop with increasing HTT to the 3300 K of graphitization.

Other types of shrinkage pores can occur, usually at temperatures higher than that required to form the slit-like pores associated with the flow-type anisotropy of the mesophase. These shrinkage pores occur at the positions of disclinations[32] within the semi-coke/graphitic substance. These disclinations are usually positions of extreme distortion and are created by the bending, folding or twisting of the plastic mesophase. Under conditions of graphitization, the induced shrinkage forces are released at these disclination centres and pores appear within the fold of the disclination.

Like the majority of all shrinakge cracks, the pore wall is composed, predominantly, of basal plane surfaces and not prismatic edges. This is of importance when considering the development of the pore by gasification when the end of a pore appears to be more reactive than the wall of the pore. The prismatic edge of the graphite crystal is more reactive than the basal plane, to molecular oxygen, by a factor of about 10^3.

Shrinkage cracks are to be found where coke from the binder pitch and coke-grist have not formed a bond and where, on graphitization, they have separated at the interfacial position.

The porosity considered above is monitored by optical microscopy and hence its size is greater than about 0.5 μm. Pores with dimensions 0.05 to 1 μm are associated with the secondary crystalline structure, i.e. within the isochromatic domains and mozaics. Unpublished studies of Crawford and Marsh[60] using phase-contrast electron microscopy reveal 'crystallites' of graphite material within the 'macro-crystalline' isochromatic areas and that these grow separately and distinctly creating pores or voids, ~0.01 μm wide and 0.1 μm in length. Pores are also to be found within these secondary crystallites but their dimensions are less than 0.01 μm and they probably constitute closed porosity.

2.3. Methods of Characterization of Porosity.

Methods based on microscopic techniques that are studied in this thesis are described in Chapter 5. This Section describes other methods which give information concerning pore structure.

2.3.1. Gas-Adsorption Studies.

The term adsorption is used to describe a higher concentration of gas (vapour) molecules at the surface of a solid or liquid than is present in the gas phase in equilibrium with the material. The term absorption describes a penetration of gas, vapour or liquid into the bulk of the material. In reality, with microporous materials a sensible differentiation between adsorption and absorption is not possible. Rates of adsorption, incorporating a knowledge of diffusion in porosity can be used to provide information about pore sizes[61].

There are two types of adsorption, physical adsorption and chemical adsorption, (chemi-sorption). Physical adsorption is caused by molecular interaction forces (usually van de Waals), causing the formation of a physically adsorbed layer, and chemi-sorption involves the transfer of electrons between the solid (adsorbent) and the gas (adsorbate) to form a chemical compound between the adsorbate and the outermost layer of the adsorbent molecules.

The distinctions between physical adsorption and chemi-sorption in the majority of systems is quite clear. However, there are boundary systems where one is not sure if they should

be called physical adsorption or chemi-sorption. Criteria to distinguish between these two types of adsorption include[62]:

(a) The extent of physical adsorption decreases with increased temperature at constant pressure, whereas the extent of chemi-sorption increases with increased temperature.

(b) Physical adsorption processes are reversible, chemi-sorption processes are usually not reversible.

(c) Physically adsorbed material can be removed by reduction of pressure, whereas removal of chemically adsorbed material requires conditions of prolonged evacuation at elevated temperatures.

(d) Heats of adsorption for physical adsorption are a little greater than the enthalpies of vapourisation (~80 $kJ\,mol^{-1}$) whereas chemi-sorption processes can easily have heats of adsorption approaching 400 $kJ\,mol^{-1}$.

Gas adsorption is a method widely used to measure surface areas which are determined by the amount and size of contained porosity. The surface area is measured in m^2g^{-1} and, for carbon,

it varies from <1 m^2g^{-1} for non-porous, glassy carbons to >1000 m^2g^{-1} for highly porous, active carbons. Adsorption studies can only be used to give pore size distributions of micro- and meso-porosity. In order to study distributions of macro-pores other methods must be used.

The volume of a gas adsorbed on the surface of a given solid is a function of the temperature of the adsorbent and the gas pressure. As the temperature decreases (constant pressure) or the pressure increases (constant temperature) more gas is adsorbed. The adsorption isotherm of a porous solid is measured at a constant temperature, by determining the volume of gas adsorbed as the relative pressure (P/P_o) increases. P is the pressure at which adsorption takes place, and P_o is the vapour pressure of the gas at the temperature of the adsorbent. The most commonly used adsorbent is nitrogen.

A plot of the amount adsorbed against the relative pressure gives an adsorption isotherm. Adsorption isotherms vary a great deal over a very wide range of solids, but the majority can be classified into five types,[63, 64] as shown in Figure A4. The Type I isotherm indicates a monolayer of adsorbate on a microporous material; the volume of gas adsorbed reaching a

limiting value as the gas pressure increases. The Type II isotherm indicates a multilayer adsorption on a material with open surfaces, i.e. no internal porosity. The Type III isotherm indicates a rather unusual adsorbent with an 'inert' type of surface where the adsorbate molecules are attracted to each other to a greater extent than to the adsorbent (e.g. water on graphite). The Type IV and V isotherms correspond to the Type II and III isotherms where there is a cut-off in the meso- and macro-porosity so causing the isotherms to flatten off.

Langmuir[65] described the Type I isotherm, and derived an equation (to calculate surface areas) based on a model of monomolecular layer of adsorbate on the surface of an adsorbent. He assumed that all sites were equivalent and that there was no interaction between the adsorbate molecules. Dubinin[66] developed a semi-empirical adsorption equation (to calculate micropore volume) which has been used for studies of adsorption of many adsorbates in microporous adsorbents[67]. A very comprehensive survey of the use of adsoption data in evaluating surface areas and pore size distributions of porous solids is given by Gregg and Sing[68].

2.3.2. Mercury Porosimetry

Mercury porosimetry[69] provides a measurement of pore size distributions from a knowledge of mercury penetration by forcing mercury into the pores of the solid at successively increasing pressures. Washburn[70] first suggested the use of penetration of liquids into porous solids in order to measure capillary volume. He proposed that for a constant surface tension and contact angle, the diameter of a pore entered by a liquid is a direct function of the applied pressure. He developed the relation:

$$d = \frac{4T\cos\theta}{P}$$

where d is the smallest pore diameter impregnated, T is the surface tension of the penetrating liquid, θ is the contact angle between the liquid and the solid and P is the applied pressure.

Ritter and Drake[71] applied this method to the determination of the macropore size distribution in a porous solid. They used mercury as the penetrating liquid at pressures up to 70 MN m^{-2} (700 atmosphere), filling pores down to 20 nm diameter. Drake[72] extended the lower diameter limit to 3.5 nm by using pressures up to 400 MN m^{-2}.

Mercury porosimetry gives a pore size distribution by impregnation at increasing applied pressures. Each increment of applied pressure causes the next smaller set of pores to be filled, so gradually increasing the volume of mercury impregnated into the solid.

Certain uncertainties and assumptions are made when using mercury porosimetry. The most important assumption is that the pore entrances are circular, and the open pore entrances only are measured. Other uncertainties include the value of the surface tension and the angle of contact of mercury. The precision of contact angle measurements is limited[73] due to the large influence exerted by simple experimental factors, such as the humidity of the air, and by the purity of the liquid phase and of the surface of the solid. However, literature values for mercury on the same solid are in close agreement whereas the use of different solids can lead to significant changes in the value of the contact angle.

Impregnating mercury into the pores of solids can cause damage if high pressure is used. Dickinson and Shore[74] carried out porosity measurements in graphites using mercury porosimetry. They found that after impregnation with mercury up to 100 MN m^{-2} (15,000 psi) most of the graphites retained

a small fraction of mercury when the pressure was removed, even on heating under vaccum to 1043 K. For most of the graphites the accessible porosity derived from mercury porosimetry at maximum pressure was greater than that calculated from helium density measurements. The mercury porosity was equal to the helium porosity at an intermediate pressure of about 18 MN m^{-2} (2600 psi) corresponding to a pore diameter of 80 nm. Dickinson and Shore[74] concluded that in some graphites some of the closed porosity becomes open under high mercury pressure, which could be caused by breakage of thin pore walls. Baker and Morris[75] confirmed this structural damage by repeating mercury porosimetry measurements on the same sample of graphite. They concluded that damage certainly occurred at pressures of 15-20 MN m^{-2} (2000 - 3000 psi) and above and stated that when mercury porosimetry indicates substantial volumes of pores smaller than about 100 nm, care should be taken in its interpretation.

2.3.3. Metal Impregnation Methods.

Porous materials can be impregnated with other metals (but at higher temperatures) e.g. silver, in a similar manner to mercury. The samples are degassed under vacuum, immersed in molten silver and a suitable pressure is applied to force

the silver into the pores. The impregnated samples are cooled down to room temperature and cut from the solidified mass of silver. The impregnated samples can be examined by the following methods[76]:

(1) X-radiography of thin sections of the sample,

(2) Examination of the metal skeleton remaining after the carbon has been removed by oxidation (see Section 5.3.5).

In order to carry out X-radiography, the sections must be less than 100 μm thick. The simplest method of taking radiographs is by using a tungsten X-ray tube, and taking a contact print on a radiographic film. The radiograph itself is essentially a shadow pattern (by absorption of X-rays by the silver) and reveals changes in the total absorption of the radiation passing through the object. The detail is provided by the variations in intensity of the transmitted X-ray beam and so enables open and closed porosity to be distinguished[77].

CHAPTER 3

GASIFICATION REACTIONS OF CARBON AND GRAPHITE

3.1. Gasification in Air (Molecular Oxygen).

Rates of oxidation of graphite by oxygen are very sensitive to traces of catalytic impurities, particularly metals in the graphite[78]. The metal particles are often mobile and can burrow or channel through the bulk graphite. Two important kinetic aspects of the carbon-molecular oxygen reaction are stated here: (1) the reaction is inhibited by carbon monoxide and (2) during the oxidation, both with pure and impure carbon, oxygen is chemisorbed on the surface as surface oxygen complexes. Some of these surface oxygen complexes are of relatively short life and may truly be reaction intermediates. Hence, discussions of the kinetics of oxidation must include the role of surface oxygen complexes which may be mobile over the carbon surface, and (to add to the complexity of the reaction) have different thermal stabilities during the progress of an isothermal reaction and of a non-isothermal reaction.

Rhead and Wheeler[79] were early workers who indicated that oxygen combines with (adsorbs onto) carbon to form this surface

oxygen complex, $C_x O_y$, of variable composition. This complex decomposes over a wide range of temperatures in vacuum to give a mixture of carbon monoxide and carbon dioxide. These observations were confirmed by Lowry and Heulett[80] who found that the gases could be evolved up to 1173 K. Carbon dioxide is evolved predominantly at lower temperatures (below ~873 K) and carbon monoxide is evolved at higher temperatures. Marsh and Foord[81] showed that, during oxidation of a carbon with molecular oxygen, the relative extent of formation of carbon dioxide by the direct route (as distinct from oxidation of gaseous carbon monoxide) is a function of structural parameters and purity of that carbon under investigation.

Phillips et al.[82] investigated the influence of reaction temperature on the product ratio of the reaction of Graphon (a graphitized carbon black) and oxygen. They determined the amounts of stable oxygen complexes on the surface, by decomposing them at elevated temperatures. Increasing the temperature of chemi-sorption can initially increase the extent of chemi-sorption, but eventually at about 673 K, a maximum is reached, decomposition begins and the standing concentration of surface oxygen complexes decrease[83, 84]. A minimum in the ratio of CO:CO_2 evolved during decomposition occurs with maximum concentration of surface oxygen complexes. There is also

a certain optimum pressure of oxygen, ~0.07 to 0.08 MPa for maximum fixation of oxygen at 673 K. Lobenstein and Deitz[85] studied chemi-sorption of oxygen on a few carbon adsorbents at 473 K.

The mechanism of formation of carbon monoxide and carbon dioxide during the carbon-oxygen reaction can be described by the following reaction stages:

$$C_f + O_2 \rightarrow C(O_2) \qquad (1)$$

$$C(O_2) \rightarrow C(O) + C(O) \qquad (2)$$

$$C(O) \rightarrow CO \qquad (3)$$

$$C(O) + C(O) \rightarrow C_f + CO_2 \qquad (4)$$

$$CO + C(O) \rightarrow C_f + CO_2 \qquad (5)$$

$$O_2 + 2C(O) \rightarrow 2CO_2 \qquad (6)$$

where C_f is a free site on the carbon surface where reaction is possible, $C(O_2)$ is chemi-sorbed molecular oxygen and $C(O)$ is a chemi-sorbed atom of oxygen. The above sequence of reactions give an indication of the complexity of the

mechanism of the carbon-oxygen reaction. The species C(O) and $C(O_2)$ probably represent surface oxygen complexes with a range of thermal stabilities associated with different environments, within the carbon surface, of the carbon atom to which the oxygen is attached. As the carbon atoms attached to the surface oxygen complexes are removed by outgassing as carbon monoxide and dioxide, so the intermediate environment of surface carbon atoms still bonded to oxygen will change together with their 'reactivity'. These changes make it very difficult to correlate thermal stability of surface oxygen complexes with surface structure of the carbon atoms.

The surface oxygen complexes after formation, may decompose to give carbon monoxide (reaction (3)), or they may interact with each other to give gaseous carbon dioxide (reaction (4)), or they may interact with gaseous carbon monoxide or molecular oxygen to form carbon dioxide (reaction (5) and (6)). As the reaction proceeds, with the progressive removal of carbon atoms from the surface of the carbon, so the physical and electronic structure of the carbon surface will change. This implies that the progressive oxidation of a carbon surface can cause a change in the bonding of surface oxygen complexes.

Medalia et al.[86] using electron microscopic techniques found that after oxidation of carbon black with oxygen, in the temperature range 630 K to 730 K, the interior of some particles burned away as soon as the relatively stable outer shell of the particles are penetrated, leaving only a hollow, or porous shell of high surface area. This mechanism accounts for the time-dependence of the rate of oxidation of a sample of carbon black.

Oxygen chemi-sorption studies have been made on graphite of high grade purity and graphite to which 0.3% of iron was added[87]. Walker et al.[87] concluded from the investigation that: a) a surface complex is produced but the rate constant is independent of the extent of surface coverage; b) the values of entropy of activation indicate that the activated complex chemi-sorption is an immobile complex; c) the total active surface area is about 4% of the total BET surface area, suggesting that the reaction is confined to the edge atoms of the crystallite planes, and d) iron is an active catalyst for the chemi-sorption of oxygen onto graphite. However, little reliable information was obtained on the mechanism of the catalysis.

Vastola et al.[88] using O^{18} as a tracer, showed that the oxygen atoms of the carbon dioxide produced during the reaction of carbon with oxygen do not always come from the same molecule

of oxygen. This implies a dissociation of the oxygen molecules into oxygen atoms on the carbon surface and the independent migration to new sites of the mobile oxygen atoms (not necessarily atomic oxygen).

Studies, using gold decoration techniques, of the topographical changes in surfaces during oxidation of graphite indicate that sites on basal planes of preferred attack can often be identified with the cores of non-basal screw and edge dislocations on the surfaces of graphite crystals and with point defects[89]. Kinetic studies on the carbon-oxygen reaction have been carried out using pure graphite to eliminate the effects of impurities in order to establish reliable kinetic parameters[90]. Activation energies of the carbon-molecular oxygen reaction are dependent upon the structure of the carbon being oxidised. Therefore unlike the majority of chemical reactions e.g. a hydrolysis of an ester, it is not possible to publish one, unique value of an activation energy which is common for all studies. Activation energies for reactions of carbon with oxygen vary from about 120 kJ mol^{-1} to about 270 kJ mol^{-1}. Carbons containing a high concentration of impurities yield values of about 147 kJ mol^{-1} (35 kcal mol^{-1}) and graphites containing less than 5 ppm impurities yield values of about 252 kJ mol^{-1} (60 kcal mol^{-1})[90].

3.2.Gasification in Carbon Dioxide.

The reaction between different forms of solid carbon and gaseous carbon dioxide has been investigated for many years by different investigators[91-93], covering different aspects including:- pore structure, kinetics, topography, surface complexes and gasification products. Some of these aspects are discussed in a summary by Thomas[94]. According to Lind and Wright[95], graphite has been reacted with carbon dioxide in conditions ranging from small quartz bulbs in the laboratory to the carbon dioxide coolant of working nuclear reactors.

Reaction rates of different grades of graphite are seldom the same. This may be attributed in part to differences in crystalline imperfections and porosity. These differences are also related to the impurity level of inorganic compounds in the graphite[96].

It was suggested by Long and Sykes[97] that impurities affect carbon reactivity by interaction with the π-electrons of the carbon basal planes. This interaction is attributed to a change in the bond order of the surface atoms so affecting the ease with which they can leave the surface as oxides of carbon. According to this theory, removal of an electron by an impurity increases the rate of reaction, whereas addition of an electron decreases the rate of reaction. Since the π-electrons are known

to have high mobility in the basal plane, the impurity does not need to be adjacent to the reacting carbon atom. However, currently this theory has little support. The mechanism now generally accepted is that catalytic gasification occurs at the point of contact of catalyst with carbon and that the catalyst can be an oxygen carrier.

The overall thermal reaction between carbon and carbon dioxide at high temperatures is represented by the following equation:-

$$C + CO_2 \rightarrow 2CO \text{ (gasification reaction)} \qquad (7)$$

During this reaction, the first step is the dissociative adsorption of carbon dioxide at free active sites on the carbon, C_f.

$$C_f + CO_2 \rightarrow CO + C(O) \text{ (oxide formation reaction).} \qquad (8)$$

This results in the formation of a carbon monoxide molecule and a bound surface oxide[98] on the graphite which subsequently decomposes at temperatures above 873 K[90] removing a carbon atom from the solid to the gas phase, evolving carbon monoxide.

$$C(O) \rightarrow CO \qquad (9)$$

Since C(O) is actually attached to the graphite lattice this equation can be written as:-

$$C(O) \rightarrow CO + nC_f \qquad (10)$$

to account for regeneration of active sites C_f. In this case n is an integer having a value from zero to two; if a steady state reaction can be maintained, then n has a value of one[99].

Ergun[100] postulated the existance of active sites on the carbon surface and suggested that the differing reactivities of various carbons arose from variations in the number of active sites. He proposed that equation (8) was reversible:

$$\underline{i.e.}\ C_f + CO_2 \rightleftarrows CO + C(O) \qquad (11)$$

This proposal was supported by Bonner and Turkervich[101]. They used $^{14}CO_2$ to show that the rate of oxide formation is greater than that of decomposition, i.e. the forward reaction in equation (11) is very rapid, resulting in a large build-up of surface oxide. They also found no evidence for the reverse of equation (9).

Harker et al.[102] showed that the presence of surface oxide on the carbon retards the rate of the carbon dioxide reaction, but enhances the rate of carbon dioxide formation from carbon monoxide.

$$C(O) + CO \rightarrow CO_2 + C \qquad (12)$$

Two mechanisms have been proposed to account for the inhibiting action of carbon monoxide. In the first, carbon monoxide is assumed to adsorb reversibly on the active sites forming an inactive complex C(CO):

$$C_f + CO \rightarrow C(CO) \qquad (13)$$

The inactive complex C(CO) blocks off the active sites and so reduces the rate of reaction.

In the second mechanism adsorption of carbon monoxide is assumed to be negligible and the inhibition is due to the reversibility of equation (11) and the existance of equation (10)[90]. There is strong doubt, from kinetic studies, that the latter mechanism is correct.

Two strong arguments against the first mechanism were given by Reif[103] who showed that chemi-sorption of carbon monoxide is negligible and Ergun[100] who, using three very different carbons, obtained an equilibrium constant for reaction (11) which was independent of the purity and surface area of the three carbons. Turkdogan and Vinters[104] contributed to this field, and carried out work on the poisoning effect of carbon monoxide. The reaction kinetics implied that the carbon monoxide has a two-fold poisoning

effect: (1) covering the surface sites due to strong adsorption and (2) increasing the activity coefficient of the activated complex for the dissociation of carbon dioxide on the surface of carbon. No direct evidence for carbon monoxide adsorption was provided. The adsorption was assumed for the model.

Grabke[105] carried out kinetic studies and confirmed the following reaction mechanisms:

$$CO_2 \rightleftarrows CO + O \text{ (adsorbed)} \qquad (14)$$

$$O \text{ (adsorbed)} + C \rightleftarrows CO \qquad (15)$$

From the kinetics he showed that these two reactions predominantly take place at different sites, although the kinetics of both reactions are correlated. A uniform oxygen activity is established at the carbon surface by the interplay of the oxygen surface diffusion of both reactions. Grabke concluded that no general explicit rate equation can be given for the oxidation of carbon in carbon dioxide.

Various degrees of coverage by surface oxide have been reported for the reaction between graphite and carbon dioxide. Gulbransen and Andrew[106] using spectroscopic graphite in 0.01 MPa of pure carbon dioxide, obtained 5, 20 and 30% coverage at 770 K, 870 K and 970 K respectively, but zero coverage above 1170 K. Tonge[130] obtained a 4% coverage on nuclear graphite at

720 K and a 20% coverage at 820 K. However, Lang et al.[107] concluded that coverage on purified nuclear graphite was less than 0.5% over the same temperature range. Sykes and Thomas[108] detected no adsorbed oxygen in the surface of graphite at temperatures between 1020 K and 1170 K.

Board[109] oxidised nuclear-grade graphite (PGA) with carbon dioxide in the temperature range 970 K to 1070 K, and showed that the rate of oxidation of the graphite was independent of the carbon dioxide pressure. When carbon monoxide is present, the rate decreases as the ratio of the partial pressures increases, i.e. P_{CO_2}/P_{CO}.

Grabke[110] confirmed this, at slightly higher temperatures. He showed that the amount of oxygen adsorbed on graphite at temperatures between 1170 K and 1370 K is independent of the total pressure, but is critically dependent on the carbon dioxide/carbon monoxide ratio of the gas. Board[109] showed that the rate of oxidation of Pile Grade A graphite (PGA) increased with burn-off up to 4% burn-off and then the rate became nearly constant. Different values of the rate constants and activation energies have been obtained by different authors. Walker et al.[96] have extensively reviewed the earlier work in this field.

The gasification of carbon by carbon dioxide can be described by the following rate equation[96, 99].

$$\text{Rate} = \frac{k_1 P_{CO_2}}{1+k_2 P_{CO} + k_3 P_{CO_2}}$$

P_{CO_2} and P_{CO} are partial pressures of carbon dioxide and carbon monoxide, k_1 k_2 and k_3 are constants related to the rate constants of steps in a reaction sequence.

There is no simple order for the carbon-carbon dioxide reaction. The reaction will be first order at low partial pressures of carbon dioxide and zero order when $K_3 P_{CO_2} \gg 1$. Therefore, experimentally, reaction orders are reported varying from zero to one dependent on the experimental conditions and the structure and porosity of the carbon reacted.

The approach of Ergun and Mentser[99] explains the relevant kinetic and mechanistic information for the uncatalyzed carbon - carbon dioxide reaction at temperatures below 1300 K and at pressures up to one atmosphere.

At temperatures below about 1700 K the rate of gasification progressively increases with temperature according to the

Arrhenius Equation, but in the region of about 1700 K it begins to level off to become temperature independent and eventually beyond 1700 K to show a negative temperature coefficient i.e. the rate of oxidation decreases with increasing temperature. Beyond about 2300 K, the rate again assumes a positive temperature coefficient. An explanation[90] put forward for these effects states that up to about 1700 K any damage sustained by the graphite surface during oxidation remains. Beyond 1700 K, because of the possibility of surface diffusion of carbon atoms, the damage of the graphite is 'annealed' and the reactivity of the carbon surface exhibits a marked decrease. Eventually, with increasing temperature, the rate of diffusion of carbon atoms reaches some limiting value and the rate of oxidation begins to increase again with increasing reaction temperature.

The activation energy for the carbon-carbon dioxide reaction is about 330 kJ mol^{-1} and about 160 kJ mol^{-1} for the catalytic gasification of carbon by carbon dioxide.

The development of pore structure within solid carbon during reaction with carbon dioxide has been studied by several investigators. Dubinin et al.[111] carried out studies on the porous structure of active carbons obtained by activation of carbonized

sucrose with carbon dioxide at 1120 K. He used adsorption and small angle X-ray scattering and found that during activation nearly the entire volume of the oxidised carbon formed micropores, increasing their volume by a factor of 2.5 to 3.

Kalback et al.[112] studied aspects of pore growth within porous graphitized carbons which were oxidised in carbon dioxide at temperatures of 1200 K, to different percentage burn-offs. He used mercury porosimetry to obtain pore-size distributions, to follow the increase in macroporosity during oxidation.

He concluded that the major portion of early pore development apparently occurred by preferential burning of the single crystallites of carbon parallel to the basal planes of the crystallites. This yielded pores of approximately the same size as the original carbon crystallites (50 nm to 300 nm)[112]. The pores developed by this mechanism reached a maximum volume, where further development in this range of pore size ceased. It was suggested that this was due to exhaustion of exposed crystallites of the correct orientation, i.e. when a single crystallite has completely burned away, the crystallite at the end of the resulting pore could have a different orientation.

After this pore development ceased, the walls of the larger pores constituted a major portion of the gasified carbon.

Walker and Raats[113] studied pore growth in a reaction between a type of graphitized carbon rod and carbon dioxide. Pores were developed by a two step process, first, by burning small amounts of one type of graphitic material, which removed pore constrictions, followed by burning at the surfaces of larger particles of a second type of graphitic material.

Marsh and Rand[114] used adsorption measurements and mercury density measurements in order to study changes in porosity of an 1123 K polyfurfuryl alcohol carbon during gasification in carbon dioxide. They showed that all the closed porosity is opened to adsorbate and the reacting gas in the initial stages of gasification.

3.3. Gasification in Atomic Oxygen.

A number of workers have studied the reaction between carbon and atomic gases in order to obtain a better understanding of the reaction with gas atoms and molecules. Streznewski and Turkevich[115] reacted evaporated carbon films and carbon particles with oxygen atoms produced in a discharge tube. They found that the carbon was readily oxidised but the rate of oxidation was independent

of temperature in the range 293 K to 373 K and dependent directly on the oxygen atom concentration.

Otterbein and Bonnetain[116] studied the kinetics of the reaction of atomic oxygen with carbon. They showed that at temperatures below 373 K, reaction rate is determined by the decomposition of surface oxides, whereas at temperatures over 473 K, gas phase diffusion of atomic oxygen is determining the rate.

Blackwood and McTaggart[117] oxidised natural graphite in oxygen atoms produced by a radio-frequency discharge. They found that carbon monoxide was the primary product, but carbon dioxide was formed by oxidation of the carbon monoxide at the surface;

$$\underline{\text{i.e.}}\ C + O \rightarrow CO \qquad (16)$$

$$CO + O \rightarrow CO_2 \qquad (17)$$

Vastola et al.[118] confirmed that carbon monoxide was the major product and found that an extensive reaction occurred between atomic oxygen and carbon whether the carbon was inside or outside the actual discharge area.

Marsh et al.[119, 120] prepared atomic oxygen by dissociation of nitrogen free molecular oxygen in a microwave discharge. They measured the temperature dependence of the oxidation of

carbon and the amounts of surface oxide formed in the temperature range 273 K to 673 K. The extent of surface oxide formation was measured by outgasing in vacuum over selected temperature intervals, collecting the desorbed gases and analysing in a mass spectrometer. They found that oxidation of 1573 K polyvinylidene chloride carbon and purified Ticonderoga graphite crystals were both temperature dependent. The surface-oxides retard the rate of oxidation[121] and decompose on heating to give both carbon monoxide and carbon dioxide. Rates of gasification are controlled by both chemical and diffusion processes.

Marsh et al.[122] in earlier work had found that unlike the reaction with molecular oxygen, atomic oxygen produced a general background of conical pits, as well as etch pits associated with defect structures, on surfaces of crystalline graphite but not on pyrolytic graphite. There was much less structural reaction anisotropy during oxidation by atomic oxygen than by molecular oxygen.

The presence of iron on the surface of Ticonderoga graphite promoted recombination of atomic oxygen, so decreasing the oxidation rate. Areas of the graphite surface, in the vicinity

of small globules of iron therefore remain unoxidised and develop into hexagonal hillock structures orientated at right angles to the hexagonal pits produced by oxidation in molecular oxygen[122].

Marsh et al.[123] also showed that graphite crystals irradiated with neutrons behave differently from unirradiated crystals on oxidation with atomic oxygen at 473 K. Instead of small conical-shaped pits being observed, much larger flat-bottomed pits were produced with average diameters of 5 μm.

Lang et al.[124] examined the reaction of very pure graphite with oxygen atoms produced by the thermal decomposition of ozone. They considered that the formation of atomic oxygen by electrical excitation of molecular oxygen gave rise to secondary products such as ions, excited molecules and free radicals, which could react with the carbon and give erroneous results. Examination of the carbon after oxidation showed that reaction had taken place to some extent in the pores as well as on the external surface.

Rosner and Allendorf[125] studied the kinetics of the reaction of graphite and atomic oxygen and diatomic oxygen using a microwave discharge, in the temperature range 1100 K to 2000 K. They found that the oxidation probability for atomic oxygen

attack (a) exceeds that for molecular oxygen by factors from 5 to as much as 80, (b) passes through a maximum in this temperature range, as does the molecular oxygen attack, and (c) is independent of oxygen partial pressure in contrast to the kinetic order of the molecular oxygen-carbon reaction. From this study, the conclusion is that atoms of oxygen do not behave like the dissociated oxygen in the molecular oxygen reaction.

An extensive study of the kinetics and mechanisms of the carbon-oxygen reaction are covered by Foord[126].

3.4. Gasification in Atomic Hydrogen.

The reaction between atomic hydrogen and carbon has been studied by a few workers, although not as much work has been carried out as with atomic oxygen.

Blackwood and McTaggart[117] obtained methane from carbonized wood at room temperature, by gasifying with atomic hydrogen. Shahin[127] obtained a mixture of methane, acetylene, ethylene and ethane from graphite at about 973 K with the specimen located outside the discharge, but found no reaction at room temperature.

Vastola et al.[118] found that the reaction between atomic hydrogen and graphite would only take place if the carbon was located inside the discharge. They obtained small amounts of

hydrocarbons, gaseous and solid when the carbon was directly in the hydrogen discharge.

King and Wise[128] obtained a mixture of methane and acetylene from carbon films at temperatures between 365 K and 520 K. They concluded that the predominating reaction was the recombination of hydrogen atoms.

3.5. Radiolytic Oxidation of Graphites.

The type of gas used as a coolant in a nuclear reactor depends initially on the temperature at which the reactor is to operate. Unless an inert gas, such as helium is used, corrosion of the graphite material would become serious above about 850 K.

Air could have been used as a coolant with little adverse effect on the graphite for reactors operating below 500 K. This was used in several large production reactors as well as test reactors and is discussed by Clark *et al*.[129]. But 500 K is too low a practical temperature.

At temperatures approaching 600 K oxidation of graphite by air becomes serious and carbon dioxide has been used as a coolant in Advanced Gas-Cooled Reactors up to a temperature of 850 K. However, even below 800 K radiolytic oxidation in carbon dioxide is not negligible[130].

In a graphite-moderated nuclear reactor, which is cooled by carbon dioxide, the graphite undergoes radiolytic oxidation by oxidising species created by radiolytic decomposition of the carbon dioxide. In the mid 1950s it was thought that the extent of the thermal reaction between carbon dioxide coolant and the graphite moderator was insufficient to cause any concern over the life-time of the graphite[131].

However, in operation, rates of weight loss of graphite (as moderator) were unacceptably high and some method of reducing these rates was required for the successful operation of the Advanced Gas-Cooled Reactors. A resultant programme of studies included development of more resistant graphites as well as examining the effects of additions of inhibitors to the carbon dioxide gas.

Early experiments on the protection of graphite by covering it with a layer of impervious material were terminated due to difficulties in obtaining a sufficiently impervious layer to prevent diffusion of the gas into the internal graphite structure. Silicon carbide layers were the most successful.

An alternative to this protection was the production of a closed pore graphite[132]. The most effective technique for

reducing the open pore volume was to impregnate the baked carbon four times, two of these being with pitch. This caused a reduction in the open pore volume by a factor of three. Now, inhibitors such as methane are added to the coolant gas.

Work has been carried out[133] on the mechanism of oxidation of graphite by carbon dioxide under gamma radiolysis studying the relationship between the pore structure of graphites and the radiolytic oxidation rates in carbon dioxide with traces of carbon monoxide. A correlation was obtained between the radiolytic oxidation rates and the mercury pore size distributions.

Hutcheon et al.[132] reported results for a variety of synthetic graphites for the radiation-induced reaction with carbon dioxide and showed that the oxidation rate was proportional to the open pore volume.

Standring and Ashton[134] showed that during radiolytic oxidation of graphite in carbon dioxide, up to 40% of the original closed pore volume is opened up at weight losses of < 2%. Thereafter, the remaining closed pores only become accessible in direct proportion to the graphite consumed. The pores thus opened are probably similar in character to the original open pores. Lind and Wright[95] reported, from

initial results of in-pile oxidation experiments, that radiolytic attack opens up some of the closed porosity rapidly but even after 13% weight loss, a substantial proportion of the porosity remains closed.

Feates and Walker[135] studied the primary gasification products during the radiolytic reaction between graphite and carbon dioxide. They used ^{14}C-labelled graphite, and found that when the graphite was conditioned by prolonged exposure to radiolytic carbon dioxide, the ratio of carbon monoxide to carbon dioxide rose from 0.2 at 470 K to 0.5 at 770 K. The ratio was not affected by pressure in the presence of up to 30% carbon monoxide.

This is consistant with a mechanism in which a relatively stable surface oxide is formed which can follow alternative routes during further radiolysis:

$$CO_2 + C \rightarrow C(O) + CO \qquad (18)$$

$$C(O) + O^* \rightarrow CO_2 \qquad (19)$$

$$C(O) + C(O) \rightarrow CO_2 \qquad (20)$$

$$C(O) \rightarrow CO \qquad (21)$$

Reaction (18) forms a surface oxide with evolution of carbon monoxide but no gasification. Subsequently the oxide may decompose either as a result of reaction with active species, (see below), reaction (19), or as a result of surface interaction, reaction (20). It may also desorb as carbon monoxide, reaction (21).

As the temperature is raised, surface oxide decomposes more readily so that reaction (21) will increase and the extent of reactions (19) and (20) will fall. Consequently, at the higher temperatures, the overall extent of gasification as carbon monoxide will increase, and since this requires the consumption of only one active oxygen atom, whereas carbon dioxide requires two, the efficiency of gasification will also increase.

Feates and Fryer[136] carried out studies on surface oxide formation on graphite exposed to radiolytic carbon dioxide, at 425 K. They found that the oxide formed radiolytically, was at least partially decomposed on heating the graphite to 775 K. The oxide formation appeared to be an essential preliminary to gasification since negligible gasification takes place from an oxide-free surface.

The absorption of radiation energy in the carbon dioxide gas results in the formation of an active oxygen species O^*,

which attacks the graphite after migrating to the surface. These excited oxygen species react readily with graphite to produce gaseous oxides of carbon:

$$CO_2 \rightarrow CO + O^* \qquad (22)$$

$$O^* + C \rightarrow CO \qquad (23)$$

The loss of carbon from the graphite by conversion to carbon monoxide reduces its strength, the moderator efficiency and ultimately, the life of the graphite within the reactor.

The active species may be destroyed by the deactivation reaction:

$$O^* + CO \rightarrow CO_2 \qquad (24)$$

At high pressure, gas radiolysed externally to the graphite contributes little to its attack, most of the reaction arises from excitation of the gas in the pores[134]. The gas is activated by secondary particles, electrons and heavy ions produced by interaction of gamma and fast neutron components. Excitation of the gas in the pores is thus largely a consequence of absorption of the primary radiation in the graphite itself.

The rate of oxidation of graphite has been found to be directly proportional to[95]:

(a) the volume of the open pores

(b) the pressure of the carbon dioxide in these pores

and (c) the radiation dose rate of the carbon dioxide.

The rate of attack of the graphite will increase with burn-off because oxidation opens up the pore structure. Increase in the total open pore volume will be due to widening of already existing open pores and opening up of initially closed pores.

The graphite-carbon dioxide reaction in the reactor is promoted by reactor radiation but Copestake et al.[137] reports that this radiation-induced process is unlikely to be dependant on temperature and the limiting temperature for operating the process is probably set by the thermal reaction. However, it is reported elsewhere[95] that temperature can affect the radiolytic reaction in two ways:

(a) by altering the gas density and hence energy absorption.

and (b) by changing the reaction rates.

These effects may counteract each other, hence a simple correlation with temperature may not result.

The influence of carbon monoxide added to the coolant gas (carbon dioxide) on the radiolytic oxidation of graphite is to increase the rate of removal of active species (O^*)

$$\underline{i.e.}\ CO + O^* \rightarrow CO_2 \qquad (24)$$

and to decrease the oxidation rate of the graphite. Carbon monoxide also reduces the rate of weight loss of the graphite.

The degree of inhibition of carbon monoxide depends on the distribution of the gas, its purity and the gas pressure and temperature[138]. The effect of carbon monoxide on the gamma-radiation induced reaction between graphite and carbon dioxide has been investigated at temperatures of 498 K to 648 K using ^{14}C-labelled graphites[139]. This labelling of graphites gives a unique and sensitive way of distinguishing effects on the basic structure of graphite. The ^{14}C-labelled graphites were used so that the carbon monoxide produced during the reaction could be distinguished from the carbon monoxide present at the start of the reaction which contained ^{12}C. A gas scintillation counter recorded the total ^{14}C activity in the outlet gas stream and ^{14}CO and $^{14}CO_2$ concentrations were determined by a scintillation detector in the gas chromatograph. ^{14}C-labelled graphites were developed in various ways, e.g. by incorporating ^{14}C carbon black in standard components of the graphites, or by reacting the graphite with ^{14}CO at 2273 K. However, it is difficult to obtain uniform labelling throughout the graphite.

Carbon monoxide only acts as an inhibitor to a limited extent. The degree of inhibition is unsufficient for successful operation. The radiolytic oxidation rate of graphite in a graphite-moderated nuclear reactor is so great that an additional inhibitor must be added to the carbon dioxide to minimise the radiolytic gasification. This will reduce the weight loss of graphite and hence prolong its life-span to an acceptable level. Gases such as methane have been used as inhibitors[140]. Methane interacts with carbon dioxide to yield species (complex organic material not yet identified) in the presence of radiation to protect the graphite surface. These species are:

(a) deposited on the surface of the graphite and form a protective barrier,

(b) responsible for inhibition,

(c) heterogeneously distributed, i.e. not a unimolecular layer,

(d) mobile on the surface

and (e) preferentially oxidised.

Therefore methane must be continuously injected into the coolant circuit to maintain its inhibition because methane depletion occurs continuously throughout the graphite blocks.

The surface concentration of the protective species depends on the radiolytic methane oxidation rate. Active oxygen atoms which reach the graphite pore walls react with the graphite and desorb as carbon monoxide. Other active oxygen atoms react preferentially with the protective species either on arrival at the graphite surface or during migration across the surface.

CHAPTER 4.

OBJECTIVES OF THE STUDY

The overall objective of the study is to characterise the pore structure, in terms of size, shape and interconnectivity, of nuclear-grade graphite. The study is sub-divided into several sections describing different experimental approaches which are presented in Chapters 5 to 10.

Objective 1. The assessment of methods of pore analyses. (Chapter 5).

Methods of pore analyses are assessed to elucidate those which are most useful in analyses of pore structure. The information from the several methods are used to compile a model of porosity for each type of graphite and to compare the models of the different graphites.

The methods of assessment of pore structure include:-

(a) Optical microscopy.

Optical microscopy gives a measure of the size and shape of the porosity in graphites. The limits of resolution are about 0.5 μm.

(b) Scanning electron microscopy.

Scanning electron microscopy can investigate porosity to a resolution of about 100 nm. The scanning electron microscope has a high depth of focus making it a useful instrument for studying depths of pores, and their internal structures by taking stereopairs. With stereopairs, two micrographs are taken at

different angles to the incident electron beam and viewed to obtain a three-dimensional image, capable of analysis.

(c) High-voltage transmission electron microscopy.

The high-voltage electron microscope (1,000kV) has an electron beam which penetrates specimens to about 4 μm in depth. Thus a specimen more representative of the whole sample can be studied; e.g. interconnecting pores in the structure can be detected in thin samples, especially if the pores are filled with an electron dense material.

(d) High-resolution scanning electron microscopy.

High-resolution scanning electron microscopy (based on a TEM instrument) can be used to study pores in graphite, with a limiting resolution of about 5 nm. This enables the meso-pores to be studied, in terms of their shape and size, and the associated morphology of the graphite substance.

(e) Metal impregnation methods.

Metal impregnation of graphites i.e. the filling of accessible pore volume, enables the open and closed pores to be investigated individually, by both optical and scanning electron microscopy. A three-dimensional replica of the open pore structure can be obtained by oxidizing the graphite and investigating the residual metallic replica of the porosity, including the interconnecting system.

(f) Thermal oxidation in air.

Graphites were thermally oxidized in air to investigate the relative rates of growth of pores of different sizes. Growth

is influenced significantly by pore size, whether or not it forms part of the 'transport system', and by the size of any interconnecting pores. Comparison with virgin graphites, using optical and electron microscopy, shows the development of pores during gasification.

(g) Oxidation by atomic oxygen.

Graphites were oxidized with atomic oxygen to obtain information on the changes introduced to the porosity by this species which will react at room temperature and has some resemblance to radiolytic oxidation.

(h) Photogrammetry and stereology.

Porosity in graphite must be quantified. Using photogrammetry, depths of pores, surface contours and the topography of the surface can be measured from a three-dimensional image. Using stereology, the shapes, sizes, frequency of distribution etc. of porosity can be assessed, initially in two-dimensional analyses, and subsequently in three-dimensional analyses.

Objective 2. Thermal gasification processes in graphite. (Chapter 6).

As well as studying dimensional changes in porosity following gasification, the mechanism, (e.g. topographical changes on different surfaces), of gasification has to be elucidated as this explains the development of pore size and shape. The topographical changes are examined and related to the original optical texture as observed in graphites following gasification in air, carbon dioxide, atomic oxygen and atomic hydrogen. This is done by examining the graphites before and after gasification.

Objective 3. Ultrasonic testing of graphites. (Chapter 7).

Non-destructive ultrasonic testing of graphite samples is undertaken before and after gasification, in order to monitor the extent of internal pore growth during gasification.

Objective 4. Radiolytic oxidation processes in graphites. (Chapter 8).

The surfaces of graphites which have been subject to radiolytic oxidation in a nuclear reactor (and their controls) are studied using:

a) Optical microscopy

b) Scanning electron microscopy

c) High-resolution scanning electron microscopy

in order to monitor changes in their pore structures following oxidation by measuring pore sizes, surface roughness and changes in the topography of the internal pore walls.

Objective 5. Image analyses using the Quantimet 720. (Chapter 8).

The Quantimet with a feature data module, is used to produce pore shape/size data on radiolytically oxidised graphites and their controls. From the data, changes in porosity, pore diameters, pore wall thicknesses, pore perimeters and Feret diameters are assessed.

Objective 6. Microscopic examination of irradiated graphite. (Chapter 9).

Neutron-irradiated (non-oxidised) samples of graphite are examined by microscopy. It is known that these samples differ from the

radiolytically oxidised samples in that the closed pore volume decreases preferentially when compared with the open pore volume. These samples are studied by optical microscopy to determine any difference in the optical texture after irradiation, and by scanning electron microscopy to determine changes in the topography and pore wall surfaces. An essential objective is to determine the origins of the porosity generated by the neutron-irradiation.

Objective 7. Progressive polishing of virgin graphites (Chapter 10).

Progressive polishing is carried out in order to monitor the interconnections of pores throughout the bulk of the graphite body, and to build-up a three-dimensional model of the pore structure from data obtained principally from scanning electron microscopy.

CHAPTER 5

METHODS OF ASSESSMENT OF POROSITY.

5.1. Samples.

Eight different nuclear graphites were investigated in this study as listed in Table 1; AGLMP and BAEL GCMB are manufactured from Gilso-carbon (see Section 1.3); AGLHP and Morgans EYC 9106 are unipore graphites, AGLHP is manufactured from petroleum coke and coal-tar pitch; Lima and PGA L18 graphite are manufactured from petroleum coke; BAEL VQMB and BAEL VNMC graphites are manufactured from pitch coke[141]. The open pore volume values given in Table 1 were obtained from pore size distribution curves, drawn up from mercury porosimeter measurements. It can be seen from this Table how the open pore volumes of the different graphites vary with the pore entrance diameters. Figures A5 to A12 give the mercury pore size distributions for the eight graphites examined. Table 2 lists properties for AGLMP graphite in the virgin state and after thermal oxidation to 5.4% and 10.5% weight loss. These graphites were used to investigate the effects of thermal oxidation on porosity. During oxidation the bulk density decreases and many of the closed pores become open. The open pore volume increases by about 100% at 10.5% weight loss.

5.2. Sample Preparation.

5.2.1. Optical Microscopy.

The graphite samples were prepared, for optical microscopy, by polishing the surfaces. The degree of polishing depends very much

on the hardness of the sample and certain difficulties are encountered especially if relief and pluck-out are to be avoided. Small pieces of sample are held in an epoxy resin block, by placing them in a small container, 2.5 cm diameter cylinder, and pouring resin over them. When the resin has set, the surface is ground on a rotating diamond plate to expose the sample surface. Polishing can then begin. Some samples are brittle and soft and may rupture or break-up during polishing. These must then be vacuum-impregnated with a slow-setting epoxy resin. This impregnation technique[142] is also useful for impregnating the open pores in graphite for use with the Quantimet 720 image analyzer. The sample can be ground and polished to reveal three degrees of contrast: open pores, closed pores and the graphite body. In this case the resin must have several properties: low viscosity, reasonably long setting time, good carbon wetting properties, non-contraction during setting, stability under moderate vacuum and it should be hard and chemically resistant to support the sample during grinding and polishing.

When the sample has been mounted and impregnated it is ground and polished. Polishing begins by rubbing the sample on 600- and 360-grade emery paper using water as a lubricant and cleanser. The scratches produced by cutting or grinding are removed at this stage. The virgin graphite samples, that were not mounted for polishing, were about 1 cm cube. Polishing is carried out using a paste of 5/20 alumina powder (to remove most of the scratches), 3/50 alumina

powder (to obtain a polish) and finally gamma alumina powder which has a particle size of <1.0 μm (to up-grade the polish). The specimen is rotated by hand on a Selvyt cloth which is kept taut and wet with the alumina paste. After polishing, the specimens were thoroughly washed and ultrasonically cleaned to remove residual alumina powder and debris.

5.2.2. Scanning Electron Microscopy.

For scanning electron microscopy the surface of the sample was prepared in the same way as for optical microscopy and then coated with gold in a vacuum coating unit to prevent the specimen charging during examination with resultant loss of image quality. The specimen was glued with durafix onto an aluminium stub to fit in the holder of the microscope.

5.2.3. High-Voltage Transmission Electron Microscopy.

For high-voltage electron microscopy the graphite was impregnated with mercury using the mercury porosimeter. The pressure used enabled pores down to 15 nm to be impregnated. The specimens studied were prepared in two ways. One sample was ground finely with a pestle and mortar to obtain small particles, < 0.5 μm diameter. From the other sample a thin slice, ~ 0.5 μm was cut using a microtome. Each sample was mounted on a grid 3 mm in diameter, and placed in the instrument holder.

5.2.4. High-Resolution Scanning Electron Microscopy.

For high-resolution scanning electron microscopy the samples were polished coarsely, ultrasonically cleaned, cut down to 2 mm x 2 mm x 0.8 mm, coated with Pt/Pd and adhered to a stub with a conducting adhesive.

5.2.5. Impregnation Methods.

The preparation and impregnation of metal impregnated samples was carried out by U.K.A.E.A. at Springfields[141]. The samples were cut to size, about 10 mm diameter and 5 mm high and placed in a quartz tube. Gold pellets were added in sufficient quantity to ensure complete immersion during impregnation and the tube was evacuated to remove air and moisture from the graphites. The quartz tube was heated up to 1620 K, quickly transferred to a pressure vessel and pressurized to pressures between 20 and 30 MPa. Unfortunately, with this apparatus, the gold cannot be heated during pressurization. Hence, there are some instances where incomplete filling is observed. After the impregnated graphites are removed from the chamber, any excess gold is sawn off. The graphites are examined either by polishing for optical and electron microscopy or the metallic replicas of the open pore spaces are studied by microscopy after oxidation.

5.2.6. Oxidation Methods.

The thermally oxidized samples were oxidized at U.K.A.E.A. Springfields. Oxidation was carried out in air at a temperature

of 753 K (~480°C) for several days, the oxidation rate being 55.6 μg $ksec^{-1}$ (200 μg hr^{-1}). One sample was oxidised to 5.4% weight loss, and a second sample was oxidised to 10.5% These samples were polished for optical and scanning electron microscopy. Some of the graphites that were oxidised by atomic oxygen were polished and cleaned, making sure there were no traces of alumina present in the sample. They were oxidised and examined by scanning electron microscopy. Others were not polished but were oxidised and examined in the same way.

5.3. Experimental Methods.

Figure 2 is a flow diagram of the methods which have been investigated. These are all discussed in detail in this Section.

5.3.1. Optical Microscopy.

5.3.1.1. Capability.

The optical microscope used is a Vickers M41 polarizing light microscope. Using plane polarized light and introducing a half-wave plate into the reflected path of the optical system, (Section 1.4) the optical texture of the specimen surface can be assessed and related to the structure and crystallographic orientation of the graphite. Optical microscopy gives a measure of the shapes and sizes of the macropores, the limits of resolution being about 0.5 μm. A comparison of the porosity in different graphites can be made from optical micrographs.

5.3.1.2 Technique.

Six graphites were investigated by optical microscopy: AGLMP, BAEL GCMB, AGLHP, Morgans EYC 9106, Lima and PGA L18. They were prepared by polishing the surface (Section 5.2.1.) and mounting on a glass slide

making sure that the specimen was flat. Coloured micrographs were taken of representative, characteristic areas of each graphite for analysis.

5.3.1.3 Results.

Optical micrographs are shown in Figures 3 to 8. From these micrographs information on pore-shape and size, and optical texture can be obtained. Figures 3 and 4 are micrographs of virgin Gilso-carbon, nuclear graphites, i.e. AGLMP and BAEL GCMB respectively. Figure 3 is a micrograph of AGLMP graphite showing a macropore (200 μm diameter) with thin (5 μmwide), crack-like pores orientated concentrically around the central pore. This concentric structure is very characteristic of the Gilso-carbon graphites, with the pore walls parallel to the basal planes of the graphite, and the pore surrounded by concentric layers of graphitic sheets, as demonstrated by the blue and yellow colours. Around the circular grist structure there are anisotropic mozaics, (5 μm to 10 μm diameter), arranged in such a way as to establish super-mozaics (500 μm). This demonstrates the change in optical texture in the grist structure. Figure 4 is a micrograph of BAEL GCMB graphite, showing the characteristic concentric structure, but the macro-structure here tended to be smaller than in the AGLMP graphite. The concentric grist structures are again delineated by anisotropic mozaic areas, and there are many long (100 μm), thin (10 μm) pores similar to shrinkage cracks.

Figures 5 and 6 are micrographs of virgin unipore graphites, i.e. AGLHP and Morgans EYC 9106 respectively. These two graphites are more uniform throughout their bulk than the other graphites studied and have a fine-grain optical texture. The micrograph of AGLHP graphite

has several anisotropic areas, (coloured yellow), 10 μm to 50 μm wide and 50 μm to 200 μm long. There are also several mozaic areas around the pores. The pores are either approximately circular in shape (30 μm to 50 μm diameter) or elongated (50 μm wide, and 100 μm long). The micrograph of Morgans EYC 9106, (Figure 6) has several isotropic (plain purple) areas about 50 μm diameter which are delineated by pores or by anisotropic mozaic areas. The pores in this graphite interconnect more than in the nuclear graphite. Most of the pores tend to be long (150 μm) and fairly narrow (30 μm) whereas a few others are circular pores (70 μm diameter).

Figure 7 is an optical micrograph of virgin Lima graphite, manufactured from petroleum-coke. Lima graphite is heterogeneous with large isochromatic areas indicating a large-grained graphite. The pores tend to be fairly circular, (30 μm diameter) in this micrograph. Figure 8 is an optical micrograph of virgin PGA L18 graphite, manufactured from petroleum-coke. PGA L18 is also a large-grained heterogeneous graphite. It exhibits flow-type anisotropy (from flow-deformation of the mesophase) as seen by the acicular areas of the micrograph. The pores vary in shape and size, some being circular (50 μm diameter) and probably originating as bubbles, others being irregularly shaped (left-hand-side of the micrograph) or long and narrow (10 μm wide) in the flow areas (bottom right-hand-side), originating as shrinkage cracks.

Optical microscopy thus gives a clear indication of size and shape of polycrystallinity in the different types of graphite and their orientations in the material.

5.3.2. Scanning Electron Microscopy - (SEM).

5.3.2.1. Capability.

The scanning electron microscope used was a Cambridge "Stereoscan", working at 20 kV with the sample tilted at 45° to the electron beam to ensure efficient collection of secondary electrons. In the scanning electron microscope, secondary electron emission from the specimen surface is used to create the image. An advantage of the scanning electron microscope is its high depth-of-focus. This makes it very useful for taking stereopairs, which facilitates the study of the relative depths of the pores in the graphites. The resolving power of the microscope is about 50 nm depending on the type of specimen and the mode of operation.

5.3.2.2. Technique.

Six graphites were investigated by scanning electron microscopy: AGLMP, BAEL GCMB, AGLHP, Morgans EYC 9106, Lima and PGA L18. They were prepared as described in Section 5.2.2. Micrographs were taken at increasing magnifications from x 50 to x 2000. At above x 2000 the resolution was no better than x 2000 and so micrographs were not taken. For stereopair production[143] the first micrograph was taken

at 45^{o} to the electron beam, and the specimen stage was tilted by 10^{o}, to 35^{o} to the electron beam to take the second micrograph, making note of the following:

(1) the specimen tilt must not be too great otherwise the background and foreground will not both be in focus;

(2) the magnification and field of view must be the same to avoid eyestrain and distortion;

(3) the contrast of the micrographs must be similar.

To view the stereopairs[144], the tilt axis must be perpendicular to the line of viewing, (Diagram 5.1). This is so because any parallax created by tilting the specimen in the electron microscope exists in the direction perpendicular to the tilt axis and for correct viewing this must be along the line joining the two eyes.

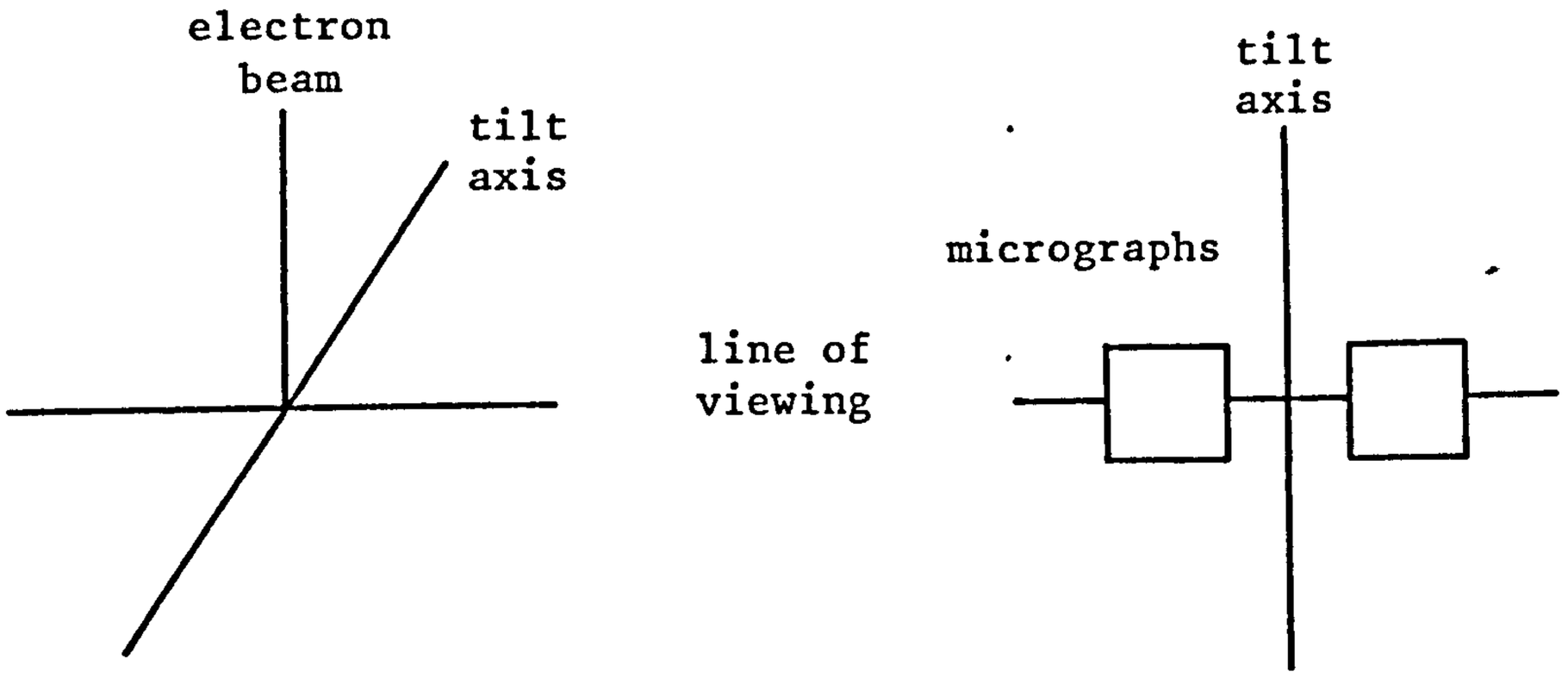

Diagram 5.1. Viewing stereopairs.

The stereopairs taken with the Cambridge "Stereoscan" must be rotated through 90° for correct viewing to fulfill the above requirement.

5.3.2.3. Results.

Some of the micrographs taken using the SEM are shown in Figures 9 to 41. Figures 9 to 16 are micrographs of virgin AGLMP graphite (manufactured from Gilso-carbon) taken at increasing magnifications. At the lower magnifications (Figures 10 and 11) the characteristic pore structure of the Gilso-carbon material can be seen. The width of the long, thin pores vary from 1 μm to 10 μm, with the central pore (in Figure 10) 30 μm wide and 200 μm long. The stereopair (Figure 11) when viewed stereoscopically, gives a three-dimensional image from which a clear indication of the pore depth can be obtained. In this stereopair the depth of the large central pore is about 30 μm.

Figures 12, 13 and 14 each show a macropore (120 μm to 150 μm) with many narrow pores (shrinkage cracks) inside the larger pores. These narrow pores vary in width from 0.2 μm to 5 μm, and in length up to about 100 μm. Figure 12 shows some rather narrow pores (1 μm to 2 μm) on the surface of the graphite. All these long, narrow pores are evident in a large number of macropores in the two Gilso-carbon graphites. These pores may interconnect with larger pores throughout the pore system. Figures 15 and 16 are higher magnification SEM micrographs

inside a macropore. They illustrate pores in the size range of 100 nm. Figure 16 shows the pore system (shrinkage fizzures) developing from the walls of the macropore in Figure 14. These micrographs show the different types of pores that are present in AGLMP graphite.

Figures 17 to 21 are micrographs (SEM)of virgin BAEL GCMB graphite, (manufactured from Gilso-carbon), taken at increasing magnifications. Figure 17 shows a typical, pore structure in the Gilso-carbon material with a large central pore (80 μm diameter). The concentric pores, probably shrinkage cracks, around the central pore, range in size from about 1 μm to 20 μm. Figure 18 illustrates a large macropore (200 μm wide) with many small pores (0.5 μm to 5 μm wide), in the surface of the macropore. The stereopair in Figure 19 gives an indication of the pore depth (about 60 μm) and shows that some of the pores appear to have 'flaps', as if the pore surface has been pulled away. With increasing magnifications (Figures 20 and 21), pores are seen of size about 100 nm. In one pore, on the left-hand-side of Figure 21, a pore can be seen inside the thin pore. The inner pore has a width of about 100 nm. There are many of these long narrow pores, which may connect macro- and meso-pores through the graphite body.

Figures 22 to 26 are micrographs (SEM) of virgin AGLHP unipore graphite. In the low magnification micrograph (Figure 22), many

of the pores are approximately circular in shape with diameters about 20 μm to 30 μm, but there are also irregularly shaped pores (Figure 23), which are thin in one part (10 μm wide), but which open out into a circular shape (20 μm diameter). A stereopair of this pore is illustrated in Figure 24. The pore depth cannot be measured accurately from this stereopair because the bottom of the pore is not visible. The pore at the bottom of the stereopair has a thin pore (2 μm wide), on its surface which may be an interconnecting pore. Figures 25 and 26 are higher mangification micrographs of macropores. It is difficult with this graphite to take micrographs inside the macropores because they are smaller (up to 50 μm), than the Gilso-carbon graphites (up to 200 μm). However, in Figure 26, the pore structure inside the macropore (30 μm diameter) can be seen, as a series of overlapping material with thin pores (100 nm) inbetween.

Figures 27 to 31 are micrographs (SEM) of virgin Morgans EYC 9106 unipore graphite taken at increasing magnifications. Many of the pores in this micrograph are long and thin, varying from about 20 μm to 150 μm in length and 1 μm to 10 μm in width. Some pores are interconnecting, (bottom-right, Figure 27 and Figure 28). These may form part of the open pore system. From the stereopair, (Figure 29), it is difficult to measure the depths of the pores because the pores are narrow and become very dark towards the bottom of the pore. Figures 30 and 31 are higher magnification micrographs with more detail of individual pores. The side of the macropore, (30 μm diameter)

in Figure 30, has a flakey appearance, with flakes, about 1 μm wide, having pores 100 nm to 500 nm, in between them. Flakiness can also be detected inside the pores.

Figures 32 to 36 are micrographs (SEM) of virgin Lima graphites (manufactured from petroleum coke) taken at increasing magnifications. This graphite is heterogeneous with irregular pore shapes and sizes as seen in Figure 32. Figure 33 shows a macropore about 200 μm long and 60 μm wide, which consists of three, almost separate macropores (70 μm long) which have become interconnected. The pores are deep, especially the centre area, which is about 80 μm to 100 μm deep. At higher magnifications, (Figures 35 and 36) the macropores do not have any easily visible pores inside them, as seen in the Gilso-carbon and the unipore graphites. The pore in Figure 35 has a diameter of about 40 μm, whereas in Figure 36, the pores are smaller. One pore is circular (3 μm diameter) with long thin off-shoots (0.2 μm wide) and other pores are long and thin (~ 0.5 μm wide).

Figures 37 to 41 are micrographs (SEM) of virgin PGA L18 graphite, (manufactured from petroleum coke), taken at increasing magnifications. Figure 37 shows an uneven distribution of pores within the graphite, i.e. there are areas of many pores and areas with very few pores. The area with very few pores is a flow area which is associated with flow deformation of the material during the mesophase stage, (compare Figure 8). This graphite is similar to Lima graphite in that it has irregularly shaped pores (Figure 38).

The stereopair (Figure 39) shows part of a macropore. The inside surface of the macropore is very smooth and very thin pores (below 1 μm) are situated on this surface. The depth of the macropore varies in different parts, from about 15 μm to 70 μm at the top of the stereopair. Figures 40 and 41 are higher magnifications, of PGA L18 graphite, of the interior structures of two macropores. The pores walls are very rough with smaller pores (of size ~ 100 nm) evident in the walls, among the rough flakey areas. The macropores here (50 μm wide), are made up of several smaller pores (20 μm wide) which join together forming off-shoots in different directions, making up a complex pore structure.

The scanning electron micrographs discussed here show how the different graphites vary in pore shape and size according to their structure and mode of manufacture. Measurements have been made on the micrographs and stereopairs, to build up a model of the porosity in each graphite.

5.3.3. High-Voltage Electron Microscopy (HVEM).

5.3.3.1. Capability.

The high-voltage electron microscope (1,000 kV) was used because the electron beam at this voltage can penetrate thick samples (~3 μm maximum, compared with 100 nm maximum for a 100 kV electron microscope). Thus, a specimen, more representative of the whole sample, can be studied. In addition, the improved penetration of

the high-voltage electron beam enables high-resolution studies to be made of the structure of the material under examination.

The million-volt generator and the electron beam are each housed in large pressure vessels, filled with sulphur hexafluoride gas at three atmospheres pressure to provide the necessary electrical insulation. The microscope column incorporates six large electromagnetic lenses. These provide the high magnetic field necessary to focus the million-volt electron beam and also the required degree of X-ray shielding to enable the instrument to be operated safely. The specimen chamber is large enabling special experimentation to be carried out within the microscope, e.g. cooling, heating, straining and reaction studies in a controlled environment.

5.3.3.2. Technique.

Two samples of Lima graphite were investigated using high-voltage electron microscopy. One problem with this microscope is that there is a lack of contrast in the image produced. The samples to be examined must therefore be impregnated with an electron-dense material to fill the pores, making them detectable. The samples examined here were prepared and impregnated with mercury as described in Section 5.2.3. The mercury adopts the size and shape of the pores. The entry stage used for this study was the Harwell Mark II, side entry stage, which can be tilted ± 60^{o}, enabling stereopairs to be taken. The image was viewed through a thick lead glass window,

using either one of the two flourescent screens for either bright image or high resolution work. The specimen and aperture movements are controlled by 'joystick' controls with a wide range of speed and direction of motion.

5.3.3.3. Results.

Some of the micrographs taken with the high-voltage electron microscope are shown in Figures 42 to 49. The pores depicted with letters are described in Table 3. Figures 42 to 48 are micrographs of a ground sample of Lima graphite impregnated with mercury, the dark areas being mercury. In Figure 43, the very dark areas are either the grid on which the specimen was placed, or thick pieces of graphite through which the electron beam cannot penetrate. Position A appears to be the only impregnated pore in this micrograph.

Figures 44 and 45 are taken of the same area. They show pores of varying shapes, Position B to G, of sizes 500 nm to 3 μm long and 100 nm to 600 nm wide. The area of mercury at Position E has changed shape due to small volumes of mercury vaporizing while the electron beam is focussed on them. In Figure 44 there are several thin pores (below Position C) which appear to connect larger pores together. These thin pores are about 300 nm wide.

Figures 46 and 47 are a stereopair of the same area as Figures 44 and 45. The tilt angle of the stereopair is 10^{o}, with the tilt axis at 45^{o} to the line of viewing, i.e. this stereopair is not set up for correct viewing. Several mercury areas in the second micrograph have vanished due to vaporization. There are several pores which are

circular (400 nm diameter). In Figure 48 several of the mercury areas are spherical, Positions L and M. These could indicate the pore shape, but it is more likely that the mercury has come out of the pores and is lying on the surface, independent of the pore structure. Other areas, Position K, are still held in the pores and have taken up the pore shape.

Figure 49 is a micrograph of a thin slice of Lima graphite impregnated with mercury. There are several mercury areas ~300 nm wide (Position O) and some smaller areas about 60 nm diameter. Superimposition, Position N, is evident here, which is caused by examining a thick sample and so shadowing the lower pores. In Table 3, the different shapes and sizes of some of the pores, that were detected in the size range 200 nm to 3 μm, are given. Most of the pores are long and narrow, or circular.

There were several difficulties encountered when using this microscope. Unfortunately, the microscope was not in good repair. Each image had a slight halo around it. Focussing was difficult because of the required sample thickness which had to ensure that some mercury remained in the pores. A few samples of graphite impregnated with gold were studied using this microscope but difficulties were encountered in distinguishing between the gold and the graphite. Many of the gold particles remained large during grinding and tended to dominate the graphite.

5.3.4. High-Resolution Scanning Electron Microscopy JEM 100C - ASID-4D.

5.3.4.1. Capability.

High-resolution scanning electron microscopy based on the JEM 100C transmission electron microscope was used to study the micropores in graphite, the microscope having a resolution of about 5 nm. The ASID-4D is a scanning attachment which enables secondary electron images and scanning transmission images to be obtained from the specimen. A normal electron microscope filament is used. The spot size is reduced by a standard double condenser system and then further reduced by the pre-field of the objective holder. The JEM 100C - ASID-4D system acts as an ultra-high-resolution scanning electron microscope incorporating four basic SEM functions: field searching, focussing, determining exposure conditions and taking high resolution micrographs.

5.3.4.2. Technique.

Two graphite samples were examined, Lima and AGLHP unipore graphite. They were prepared as described in Section 5.2.4. Micrographs were taken at increasing magnifications, from X 10,000 up to X 200,000. Stereopairs could be taken by tilting the specimen in the microscope, an example is shown in Figures 63 and 64. For each set of micrographs, an area with very small pores or no visible pores was selected, so that at high magnifications, the field of view was not full of large macropores, making viewing difficult.

5.3.4.3. Results.

Some of the micrographs taken using the high-resolution scanning electron microscope are shown in Figures 50 to 67. Figures 50 to 58 are micrographs of Lima graphite, taken at increasing magnifications. Figures 50 to 53 are taken of the same area. In Figure 50 there are many pores, which are circular and elongated, about 50 nm to 100 nm wide. The sample was coarsely polished, which could account for the roughness of the surface seen in Figure 50. In Figure 51 some of these pores can be seen in slightly more detail. The pore in the centre is ~300 nm long and 100 nm wide, with a pointed end. Some of the pores tend to be associated with the roughness of the surface i.e. there is a pore next to each rough area. In several places there are long thin pores, (e.g. halfway down the right-hand-edge of Figure 51), which are about 10 nm wide and 200 nm long. Several of the pores are near circular in shape, 40 nm diameter. Figures 52 and 53 are slightly out of focus, beçause the adhesive used on the stub was non-conductive and although the specimen was coated with Pt/Pd, the specimen charged up during examination.

Figures 54 to 57 are taken of the same area, at increasing magnifications. The adhesive used for these micrographs was changed to a conducting adhesive and so there was no loss of image quality. Figure 54 again shows a rough surface with many small pores (50 nm), just resolvable at this magnification. The pores appear to be either near circular or long and narrow. There is more resolution in Figure 55 where both types of pores are present, of size 5 nm to 30 nm.

There are many very thin cracks visible all over the surface. In Figures 56 and 57, these cracks are seen to be pores, smaller than 10 nm wide. At the highest magnification, Figure 57, the resolution is starting to fall away and is about 5 nm. The roughness of the surface appears in Figure 56 to be a layer type structure similar to platelets, with pores underneath them, and may be associated with platelet flow of the mesophase. Figure 58 is another area of Lima graphite taken at the highest magnification, one pore, (15 nm wide) is visible although the resolution is rather poor.

Figures 59 to 67 are micrographs of AGLHP unipore graphite taken at magnifications from X 10,000 to X 200,000. Figure 59 shows a more rounded structure than the Lima graphite, with pores between 20 nm and 40 nm in diameter. In Figure 60, many of the pores are longer (200 nm to 300 nm) and extend along the rough areas of the surface. Figures 61 to 64 are micrographs taken of the same area, at increasing magnifications. In Figure 61 there are many pores of size 50 nm to 100 nm which are fairly circular. This micrograph shows how high the porosity of this graphite is, (overall open porosity down to 15 nm pores is 22.5%). Lima graphite (Figure 50) also has a high porosity, (21.0% down to 10 nm pores). Figure 62 shows thin pores, 10 nm wide which surround the rounded areas of the structure. Figures 63 and 64 are a stereopair, taken at a tilt 6^{o} either side of the normal to the electron beam, i.e. a total tilt of 12^{o}. The three-dimensional

effect is marred by the graininess of the prints and the high magnification (X 100,000). Hence, very little depth is perceived when viewing them stereoscopically. However, the pores visible are mostly long, narrow pores, 10 nm wide. Figures 65 to 67 are micrographs of another area of AGLHP unipore graphite taken at increasing magnifications. Again, there are pores 20 nm to 40 nm diameter, together with long thin pores, 10 nm wide, which surround rather rounded areas of graphite (Figure 67).

The JEM 100C - ASID-4D produces micrographs from which measurements of macropores and mesopores (down to ~10 nm) can be made. This microscope was used because of its high resolution capability. From the micrographs much can be learnt about the structure inbetween the pores as well as the pores themselves.

5.3.5. Metal Impregnation Methods.

5.3.5.1. Capability.

Graphites can be impregnated with liquid metals, i.e. their accessible pore volumes can be filled, to enable open and closed pores to be distinguished and investigated separately by both optical and scanning electron microscopy. The metal impregnation is such that after the complete oxidation of the graphite there is left a three-dimensional metallic replica of the open porisity which can be studied by scanning electron microscopy, to yield information on the pore shape and inter-connectivity of the pores.

5.3.5.2. Technique.

Four graphites were impregnated with liquid gold; AGLMP, BAEL GCMB, Lima and PGA L18. One graphite, PGA L18, was impregnated with bismuth. The graphites were prepared and impregnated[16] as described in Section 5.2.5. They were polished, cleaned and examined by optical and scanning electron microscopy. Gold was used for impregnation because it fills the pores well, it has a suitable melting point (1338 K) and it is inert to oxidation processes. Bismuth was also used, because of its low melting point, (544 K) i.e. it is easier to impregnate. The samples investigated by SEM did not need to be gold coated.

5.3.5.3. Results.

5.3.5.3.1. Optical Microscopy.

Figures 68 to 71 are examples of optical micrographs taken of impregnated samples using the half-wave plate facility. Figure 68 is a micrograph of AGLMP graphite impregnated with gold at a pressure of 24.2 MPa, to fill the open pores of size down to about 200 nm. In this micrograph there is a large area of pores which has not been filled. These are closed pores in the Gilso-carbon structure. At the bottom of the micrograph (right-of-centre) there is a closed pore (30 μm in diameter) surrounded by a narrow (3 μm wide) strip of gold, i.e. an open pore. This has a narrow off-shoot pore from the top of it, which could be an interconnecting pore.

Figure 69 is a micrograph of BAEL GCMB graphite impregnated at a pressure of 24.2 MPa. This shows an area of closed porosity (the Gilso-carbon structure), similar to AGLMP graphite. The micrograph also shows an isotropic area (left-of-centre, coloured purple), in which there is a long, thin (5 μm to 10 μm) porous system, which looks almost to be independent of the surrounding structure. As seen in the earlier optical micrographs of these Gilso-carbon graphites, (Figures 3 and 4) the Gilso-carbon structure is surrounded by anisotropic mozaics (5 μm to 10 μm diameter).

Figure 70 is an optical micrograph of Lima graphite impregnated with gold at 27.7 MPa pressure. In the centre of the micrograph, there is a pore which is incompletely filled. This could be due to the gold solidifying before it filled up the pore, or there could be a very small constriction into the pore through which the gold entered, but there was not enough pressure or time to fill the pore. Most of the pores filled with gold are slit-shaped (10 μm to 15 μm wide) whereas the unfilled pores are near circular, with varying diameters, (5 μm to 100 μm).

Figure 71 is an optical micrograph of PGA L18 graphite impregnated with gold at 24.2 MPa pressure. The left half of the micrograph shows a large anisotropic area in which there are open and closed pores. Many of the pores are long and thin (3 μm to 15 μm wide) and lie with the pore walls parallel to the basal planes, depicted by the blue colour. The other half of the micrograph has

many small circular pores (5 μm to 20 μm) which are unfilled, and surrounded by mozaic areas. The filled, open pores, tend to be non-circular, e.g. elongated in shape.

5.3.5.3.2. Scanning Electron Microscopy.

Figures 72 to 87 are scanning electron micrographs taken of impregnated samples. Figures 72 to 75 are micrographs (SEM) of AGLMP graphite impregnated with gold at 24.2 MPa pressure. In Figure 72 there are the structures of the Gilso-carbon material at the top and bottom of the micrograph. The bottom area is a closed pore structure and the top area is an open pore structure (filled with gold). This is unusual because the Gilso-carbon structure is generally a closed pore system and thus, does not become impregnated. Figure 73 shows another Gilso-carbon structure which has closed pores, with open pores around the outside of the Gilso-carbon structure ranging from 5 μm to 100 μm in width. Many of the open pores, Figures 74 and 75, are long and thin (0.5 μm to 10 μm wide), and are arranged in groups.

Figures 76 to 78 are micrographs (SEM) of BAEL GCMB graphite impregnated with gold at 24.2 MPa pressure. Figure 76 shows, for the Gilso-carbon, quite separate areas of closed and open porosity. The closed pores are mainly slit-shaped (up to 30 μm wide), whereas the open pores are various shapes, e.g. circular, elongated, slit-shaped. In Figure 77 many of the open pores are short (~ 20 μm),

and more individual than AGLMP graphite. A few closed pores are visible (1 μm to 5 μm diameter). Figure 78 shows irregularly shaped open pores with a small number of closed pores inbetween them.

Figures 79 to 81 are micrographs (SEM) of Lima graphite impregnated with gold at a pressure of 27.7 MPa. In Figure 79 there is a flow area of slit-shaped pores, in which some are open and some closed. The closed pores are about 5 μm wide and 100 μm long, and the open pores are about 1 μm to 5 μm wide and about 50 μm to 150 μm long. Around this flow area, which is associated with flow deformation of the material during the mesophase stage (compare Figure 71) there are many open pores, which are about 10 μm to 20 μm diameter. Figures 80 and 81 show more areas of open and closed porosity with the closed pores generally being slit-shaped (0.5 μm to 5 μm wide) and the open pores generally circular (5 μm to 50 μm diameter) with a few slit-shaped open pores (~ 2 μm wide).

Figures 82 to 84 are micrographs (SEM) of PGA L18 graphite impregnated with gold at a pressure of 24.2 MPa. In Figure 82, most of the pores are open, although some of the pores are incompletely filled. Most of the pores seen in this micrograph are in the size range 5 μm to 20 μm. Figure 83 shows an area in which the pores are long and thin, whereas in Figure 84, the pores are more rounded with diameters up to 30 μm. In Figure 84 there are a few closed pores at the top of the micrograph.

Figures 85 to 87 are micrographs (SEM) of PGA L18 graphite impregnated with bismuth at a pressure of 7.3 MPa, which fills the open pores down to about 0.7 μm. Figures 85 and 86 show that either the bismuth does not fill the pores as completely as the gold, or there is a large amount of closed porosity present in these areas. It is more likely to be the former statement because the open pore volume of PGA L18 graphite is quite high (16.6%); therefore, the closed pore volume will be low (~ 5%). In Figure 87, however, the large pores (above 2 μm) are well-filled, but there are many smaller slit-shaped pores (~ 0.5 μm) (top, left) which have not been impregnated.

5.3.6. Thermal Oxidation in Air.

5.3.6.1. Capability.

Graphites were thermally oxidized in air to investigate the relative rates of growth of pores of different sizes, and to obtain information on the dimensional changes in open and closed porosity during oxidation. Thermal oxidation has also been used by U.K.A.E.A., Springfields[141], to oxidize the graphite from impregnated samples, leaving a three-dimensional pore replica behind for examination of the open porosity.

5.3.6.2. Technique.

Two samples of AGLMP graphite were thermally oxidized in two experiments, in air, to 5.4%, and to 10.5% weight loss.

These samples were prepared and thermally oxidised by U.K.A.E.A. at Springfields, as described in Section 5.2.6. They were polished, cleaned and examined by optical and scanning electron microscopy.

5.3.6.3. Results.

5.3.6.3.1. Optical Microscopy.

Figures 88 to 90 are coloured optical micrographs of the AGLMP graphites. Figures 88(a) and 88(b) are virgin AGLMP graphite. Figure 88(a) is an area between Gilso-carbon structures, where there are several large pores (50 μm to 100 μm) with few smaller pores (2 μm to 30 μm) inbetween them. Figure 88(b) shows a Gilso-carbon structure with the thin crack-like pores measuring 2 μm to 25 μm in width.

Figures 89(a) and 89(b) show AGLMP graphite thermally oxidized to 5.4% weight loss. Figure 89(a) is an area between Gilso-carbon structures, where there are several large pores (50 μm to 100 μm) with many small pores (2 μm to 10 μm) and many pores between 10 μm and 30 μm (compare Figure 88(a)). Figure 89(b) shows a Gilso-carbon structure with the thin crack-like pores measuring 2 μm to 30 μm in width. Comparing Figure 88(b), there are more pores lying with their walls along the basal planes in the oxidised graphite than in the virgin graphite.

Figures 90(a) and 90(b) are optical micrographs of AGLMP graphite thermally oxidized to 10.5% weight loss. Figure 90(a) is an area between Gilso-carbon structures, where there are a large number of pores ranging from 2 μm to 80 μm. When comparing this micrograph with Figures 88(a) and 89(a) there is a progressive increase in the number of pores from the virgin to

the 5.4% weight loss, to the 10.5% weight loss graphite. Figure 90(b) shows a Gilso-carbon pore structure with pores measuring 2 μm to 40 μm in width. When comparing this micrograph with Figures 88(b) and 89(b) there is an increase in pore width from the virgin to the oxidized graphite, and there is also an increase in the number of long, thin pores in the oxidized sample.

5.3.6.3.2. Scanning Electron Microscopy.

Figures 91 to 99 are examples of scanning electron micrographs taken of the virgin and oxidized AGLMP graphites. Figures 91 to 93 are micrographs of a series of virgin AGLMP graphite, AGLMP oxidized to 5.4% weight loss and AGLMP oxidized to 10.5% weight loss, at low magnifications. The oxidized graphite surfaces (Figures 92 and 93) appear more pitted with small pores (~ 10 μm) than the virgin graphite surfaces (Figure 91). The circular Gilso-carbon structure seems more prominent in the oxidized sample i.e. they contain more pores, than in the virgin sample.

Figures 94 to 96 are micrographs of another series of the three AGLMP graphites. Again, (Figure 94) the virgin graphite has a less porous (smoother) surface compared with the oxidized graphites, (Figures 95 and 96). Also, the graphite oxidized to 10.5% weight loss has a much more pitted surface than the graphite oxidized to 5.4% weight loss, with many pores, between 5 μm and 10 μm diameter.

Figures 97 to 99 are stereopairs (SEM) of the virgin and oxidized AGLMP graphites. These stereopairs confirm the observed changes in surface topography from the virgin graphite to the oxidized graphites, i.e. the surfaces of the oxidized samples are more porous (rougher) and more pitted, than the surfaces of the virgin samples. From these stereopairs it is difficult to compare the depth of the pores, as many are narrow and the bottom of the pores are not visible.

5.3.7. Oxidation by Atomic Oxygen.

5.3.7.1. Capability.

Oxidation by atomic oxygen was carried out on graphite samples to investigate the changes introduced to the porosity by this species, which will react at a temperature slightly above room temperature, and could resemble radiolytic oxidation. Graphites, impregnated with metals, were oxidized with atomic oxygen, to leave a three-dimensional metallic replica of the open porosity which was examined by scanning electron microscopy. Oxidation by atomic oxygen enabled a low melting point metal i.e. bismuth, to be used for impregnation, as oxidation can be carried out at a low temperature, ~ 300 K (27^{o}C).

5.3.7.2. Technique.

AGLMP and Lima virgin graphites, AGLMP, BAEL GCMB, Lima and PGA L18 graphites impregnated with gold, and PGA L18 graphite impregnated with bismuth were oxidized with atomic oxygen. Two

types of apparatus were used to generate atomic oxygen. The first was a commercial "Plasmod" which produces atomic oxygen at ~320 K, (47°C). The sample is placed in a chamber which is evacuated and oxygen is drawn over the sample. Radio-frequence power at 13.5 MHz is applied around the chamber causing the gas molecules to atomize and the low concentration of oxygen atoms slowly gasifies the carbonaceous material in the chamber. As this unit was rather slow at oxidizing graphite, it could be used more as a means of etching the surfaces of the graphites, rather than oxidizing metal impregnated graphite samples completely to leave the metal pore shape. Two virgin graphites were oxidized with the "Plasmod", i.e. AGLMP and Lima. The sample of AGLMP graphite was oxidized for 30 minutes, and the sample of Lima for one hour.

The second apparatus was a "Microtron 200", a micro-wave power generator, coupled to a discharge through an air-cooled resonant cavity. The incident power was set at 60 watts with the reflected power set as low as possible. The sample chamber was evacuated and the oxygen passed over the sample, which was placed in the discharge. Four graphites impregnated with gold, i.e. AGLMP, BAEL GCMB, Lima and PGA L18, and one graphite impregnated with bismuth i.e. PGA L18, were oxidized using the "Microtron" leaving a metal pore replica for examination. The samples were oxidized for varying times (30 minutes to four hours), depending on the sample size.

5.3.7.3. Results.

5.3.7.3.1. "Plasmod" Oxidation.

Figures 100 to 107 are scanning electron micrographs of the graphites that were oxidized using the "Plasmod." Figures 100 to 103 are micrographs of a polished sample of AGLMP graphite, oxidized for 30 minutes. In Figure 100, the surface of the graphite has been etched, leaving three distinct types of porosity clearly visible:

(i) the structure of the Gilso-carbon material, with long, thin pores (2 μm to 10 μm wide) radiating from a central pore.

(ii) areas of pores in between the Gilso-carbon structures, consisting of small macropores (2 μm to 10 μm diameter) giving an appearance of a rough pitted surface.

(iii) larger, deeper pores (20 μm to 40 μm wide) seen in the bottom-left-hand corner and the centre-right-hand edge of the micrograph.

Figure 101 is a higher magnification micrograph of a Gilso-carbon structure in the centre of Figure 100. The surface has a flakey appearance with pores in between the flakes (centre-right) of about 100 nm to 200 nm diameter. Figure 102 shows another area with Gilso-carbon structures, together with larger pores (50 μm to 100 μm wide). The surface is quite rough due to the oxidation. Figure 103 shows areas of long, thin pores (~ 5 μm wide) which interconnect along the surface (e.g. bottom-right). These pores may interconnect throughout the graphite, forming part of the open porous system.

Figures 104 to 107 are micrographs (SEM) of an unpolished sample of Lima graphite oxidized in the "Plasmod" for one hour. Figure 104 shows an anisotropic flow area which is characteristic of this graphite, consisting of large slit-shaped pores, (30 μm to 50 μm wide) with many small pores (~ 5 μm wide) in between them. The surface in between the slit-shaped pores is rough. Figure 105 is a higher magnification micrograph of the centre area of Figure 104. It shows a fairly regular, pitted surface with two types of porosity:

(i) the regular pitted surface with pores less than 500 nm diameter, just resolvable at this magnification.

(ii) slit-shaped pores, of size 1 μm wide and about 6 μm long, near the centre of the micrograph.

Figure 106 shows a long flow area, about 500 μm long surrounded by a rough surface (probably associated with petroleum coke and binder) with pores ranging from 30 μm down to about 1 μm wide, consisting of near circular pores and thin, slit-shaped pores. Figure 107 shows a very rough area of Lima graphite, in which there are many slit-shaped pores, some of which appear to be in the walls of the macropores, (pore in the centre of the micrograph, and centre-left-hand edge of the micrograph). This could be due to oxidation (i.e. opening up of pores) as pores were not seen in the pore walls of virgin Lima graphite (Figures 32 to 36). The porous system could be followed through the graphites by etching away the surfaces and examining the graphites by microscopy. This may alleviate handling problems encountered during polishing.

5.3.7.3.2. "Microtron 200" Oxidation.

Figures 108 to 126 are micrographs (SEM) of metal impregnated graphites oxidized by the "Microtron 200", leaving a three-dimensional metal pore replica for examination. Figures 108 to 111 are micrographs of the gold replica, after oxidation of an impregnated sample of AGLMP graphite, for four hours. The pressure used for impregnation (24.2 MPa) should fill pores down to about 200 nm pore entrance diameter. Figure 108, taken at low magnification, gives a very complex structure, with many areas of gold above and below other areas of gold. More information is gained from these micrographs by taking stereopairs which give a three-dimensional image showing whether one gold area is above or below another area. The whole structure is pitted with small holes in the gold, ranging from 1 µm to about 10 µm. These could be small areas of graphite, but it is more likely that they are due to incomplete filling of the pores, during impregnation.

Figure 109 shows thin, plate-like pores in the centre, about 1 µm thick. There are also large areas which have not been impregnated. These are probably the structures of the Gilso-carbon material which contain closed pores and are therefore inpenetrable to the gold. Figure 110 is a stereopair of the gold pore replica. When viewing this stereopair stereoscopically there are several large areas (60 µm to 100 µm wide) with no gold in them, i.e. probably Gilso-carbon structures. The three-dimensional image gives a better idea of the connectivity of the pores through the graphite. Figure 111 is taken at a higher magnification, showing the complexity of the structure.

Figures 112 to 115 are micrographs (SEM) of the gold pore replica, after oxidizing for four hours a sample of BAEL GCMB graphite impregnated with gold. In Figure 112 the large dark areas are graphite which has not completely oxidized. In front of these areas are spaces with no gold or graphite, which could correspond to the structures of the Gilso-carbon material. Many of the pores (centre-left-hand edge) have very thin, plate-like structures (about 5 μm thick). The gold areas here, are not as punctured with holes as the AGLMP graphite. This could be due to the slightly higher open pore volume of BAEL GCMB graphite i.e. the pore entrance diameters are larger. Figure 113 contains mainly large pores i.e. large areas of gold (50 μm to 80 μm wide), with unimpregnated areas between these pores. The stereopair, (Figure 114) shows many interconnected pores with large empty areas in between. The area in the centre (shown also, in Figure 115), consists of many thin plate-like structures (1 μm thick). Some edges of these plate-like pores are very smooth whereas other edges (bottom-right, Figure 115) are very jagged with many holes, as the gold becomes thinner towards the edges of the pores.

Figures 116 to 119 are micrographs (SEM) of the gold pore replica, after oxidizing for 30 minutes a sample of Lima graphite impregnated with gold. Figure 116 is a low magnification micrograph, and shows how complex is the shape, connectivity and structure of the porous system. In Figure 117 there are pores of varying shapes and sizes. There are several long, thin pores (~ 5 μm wide),

in the centre of the micrograph. Most of the other pores are near circular, or slab-shaped. The stereopair, (Figure 118) when viewed with the 'stereo-viewer' reveals a quite different space-filling process, to that in Gilso-carbon graphite (Figure 110). These effects are difficult to quantify. Figure 119 is a higher magnification micrograph of Figure 118. It appears to be dominated by large pores (~ 50 μm) with a few smaller pores (1 μm to 5 μm wide) in the centre of the micrograph.

Figures 120 to 122 are micrographs (SEM) of the gold pore replicas, after oxidizing for two hours, a sample of PGA L18 graphite impregnated with gold. Figure 120 is a low magnification micrograph giving the appearance of a very compact gold structure with many large pores (50 μm to 100 μm wide) with long, needle-like pores (1 μm to 5 μm wide) which are connecting some of the larger pores. A few of the smaller, thin pores are punctured with holes, similar to the AGLMP pore replica. Figure 121 is a stereopair, showing that there are a few areas which are not impregnated. The stereopair also shows that some of the pores are thin plate-like structures (less than 1 μm). Figure 122 is a higher magnification micrograph of Figure 121. This shows several long, thin (2 μm to 5 μm wide) pores connecting up with larger pores (~ 50 μm wide) in the centre of the micrograph. Figure 122 also shows some very small, thin, plate-like pores (centre-right) together with a very large pore (~ 100 μm wide) at the bottom of the micrograph. Figure 122a shows several slab-shaped pores (~5 μm thick) which are quite wide (~ 50 μm).

Figures 123 to 126 are micrographs (SEM) of bismuth pore replica, after oxidizing for three hours a sample of PGA L18 graphite impregnated with bismuth. After oxidation, the bismuth replica had a reddish-brown appearance. The micrographs show large spheres of bismuth on the surface of the sample, which could be due to some oxidation reaction. In Figure 124 a flow area is seen, which is a characteristic feature of this graphite. Pore-shapes and sizes can be picked out in the bismuth replica, but it is not as accurate as the gold pore replica.

5.3.8. Photogrammetry.

5.3.8.1. Capability.

Photogrammetry involves the analysis of stereopairs (in this study, stereomicrographs). From the stereopairs a three-dimensional image of the sample being studied can be developed. Coordinates of one point with respect to another point can be calculated giving their relative positions within the three-dimensional image. Work has been carried out using mirror stereoscopes[19,20] and stereoscopic plotting instruments[145, 146, 147,] which are generally used for surveying work. These instruments can be set up to record various heights across the image. The heights can be plotted on a graph to give a profile of the specimen surface. There are problems, however, when using this technique with stereomicrographs. Geometric distortions are produced when tilting the second micrograph, which give rise to inaccuracies. Also, there are problems in establishing a datum or reference plane for the micrographs. To

overcome these problems a new plotting device has been developed[148, 149] the electron micrograph plotting device, EMPD2 (Figure 126a).

This instrument is designed, specifically, for plotting contours (of equal height or depth) of three-dimensional image surfaces, and for plotting profiles across any section of the image constructed using stereo-pairs. The EMPD2 can take any negative or print up to 130 mm by 100 mm. It is best if the prints are developed to a light grey as more definition can be detected, rather than to a high contrast. The present EMPD2 will take stereo-pairs with a tilt angle of 10^{o}, although other tilts can be used by introducing a correction factor which renders the results very slightly inaccurate. A new design is underway at the moment for the instrument, which will enable the instrument to work with stereo-pairs that are tilted at any angle. A problem arises, however, with very large angles, errors are introduced because, at large angles, the magnification of the foreground will be different from that of the background.

The EMPD2 gives good, visual displays of the surface topographies of three-dimensional images. From these displays, the depths of pores, and the diameters of pores in any direction can be measured. The shapes of pores can be analyzed and visually compared with other pores. This method of pore analysis is quite time consuming if a large number of pores are to be studied. It may be advantageous to classify the shapes of pores by some other method, and use the EMPD2 to display visually the different classes of pores.

5.3.8.2. Technique.

For operation of the instrument, the centres of the stereopairs are marked, to help in aligning them correctly. The stereopairs are placed in position on two rotating tables, ensuring that they are the correct way round. This is necessary because the optical system introduces a correction in scale of the more tilted micrograph and automatically compensates for the geometric distortion produced by the tilt. Two light spots are introduced into the optical system through half-silvered mirrors. These spots fuse together when the micrographs are positioned correctly. The resulting floating spot is fixed on the optical axis, and various parts of the micrographs are moved to this axis for viewing. The height of any feature in the image is adjusted to coincide with the floating spot by altering the separation of the micrographs. This separation is altered by a wheel which is located in the drawing head.

The drawing head controls the movement of the image in the x and y plane and has a drawing pencil placed in it. To obtain a contour the separation of the micrographs is set so that the floating spot lies on a particular point and the image is moved, keeping the spot in contact with the surface at all times. As the image moves, the drawing pencil plots out the movement in the shape of a contour. A counter is operated by the wheel in the drawing head. This measures height differences directly in millimetres. (Real height differences are obviously a function of the magnification of the system being examined). Using this digital counter, suitable contour intervals can be selected to build up a picture of the three-dimensional image.

To obtain profiles across the image, the drawing head is controlled by a profiling arm, which is set in the direction in which the profile is required. The drawing head is slid along this bar while the wheel which alters the separation of the micrographs is adjusted to keep the floating spot in contact with the surface at all times. Profiles can be drawn at set intervals along the image. All the profiles and contours are plotted out at twice the magnification of the micrographs.

5.3.8.3. Results.

Several stereopairs were examined with the EMPD2. The first pair was composed of two micrographs of thermally oxidised AGLMP graphite (Figure 127). The angle of tilt was 6^{o}, ($39^{o}$to 45^{o}). Hence, the correction factor had to be introduced to obtain accurate measurements from the contour or profile plots. The contour heights have been converted into micrometres so that heights can be read directly from the contour plots. The depth of the central pore is 500 µm (i.e. 980 - 480 µm). An arbitrary reference plane was set up at 0 µm, below the bottom of the central pore. One profile was drawn on either side of the pore. The profiles give a visual shape to the pores, enabling different pores to be compared. From the profiles, a width/depth distribution can be drawn, of different pores, showing whether there is any relation between the pore entrance diameter and the pore depth.

The second stereopair was made up of two micrographs of composite wood showing tracheids with bordered pits, (Figure 128).

The two micrographs here were placed inversely on the EMPD2. Consequently a pseudo-stereo effect was obtained. The contours slope in the opposite direction to the three-dimensional image. The contours here were not plotted in such detail as in Figure 127, plots being generally taken between the pits.

Stereopairs of a gold pore replica, after oxidation of the graphite was looked at. At a low magnification (X 12) there was too much information in the image to obtain contour plots. More meaningful plots would be obtained from higher magnification micrographs, (X 100 and higher). These stereopairs still have a large amount of information in them. Profiles would probably give more information than contours, as the shape of each gold particle could be determined.

5.3.9. Stereology.

5.3.9.1. Capability.

Stereology is the development of three-dimensional space from a study of two-dimensional sections through a material. An approach to stereology depends on measuring and classifying a large number of two-dimensional surfaces or images. The number of samples studied, to give meaningful data, depends on the homogeneity of the structure. Enough measurements must be made to represent the samples statistically[150].

Certain parameters and measurements form the basis of a quantitative sterological analysis[151]. These measurements are performed on two-dimensional sections and consist of superimposing a uniform test grid which is made up of a network of points or lines over the image and counting the number of points which lie over the areas of interest i.e. pores, (Figure 129 (a)). The fraction of points lying on transections of the component being studied, is an estimate of the volume fraction of that component. The grid can be repositioned randomly or in a particular direction and the number of points counted again. The volume fraction of a component can also be determined by measuring the area fraction of a random section, (Figure 129 (b)). The area can be estimated by lineal integration determining the lineal fraction of test lines passing through transections of the component being studied, (Figure 129 (c)). Each area is measured using a planimeter. The grid for point counting can be incorporated into a microscope eyepiece and an automatic mechanism used to move the specimen, or, systems ranging from semi-automatic up to fully automatic equipment, such as a Quantimet, can be used.

From these measurements of point counting on two-dimensional sections, the volume fraction, or porosity (if pores are being studied) can be obtained.

$$\text{Volume fraction or porosity} = \frac{\text{Number of points lying on pores}}{\text{Total number of points.}}$$

Similarly, if a grid consisting of a series of uniform short lines is used, the surface density and the volume fraction can be obtained.

$$\text{Surface Density} = \frac{2 \times \text{Number of Intercepts}}{\text{Total length of lines}}$$

$$\text{Volume Fraction} = \frac{\text{Number of end points lying on pores}}{\text{Total number of end points}}$$

There are many other stereological parameters which can be measured this way, including areas, intercept lengths, diameters, size and shape parameters. Relationships are known between measured quantities in two-dimensional sections and calculated quantities in three-dimensional space. Table 4 shows how these parameters are related. These parameters are defined as follows:

P_P = Number of points lying on a phase per unit number of points

P_L = Number of intercepts per unit test line length

P_A = Number of points per unit test area

P_V = Number of points per unit test volume

L_L = Length of lines on a phase per unit length of test lines

L_A = Length of lines per unit test area

L_V = Length of lines per unit test volume

A_A = Area of phase per unit test area

S_V = Surface area per unit test volume

V_V = Volume fraction = Volume of features per unit test volume.

All the parameters per unit volume i.e. V_V, S_V, L_V and P_V can be calculated from the remaining parameters. They are related by the following expressions:

$$V_V = A_A = L_L = P_P$$

$$S_V = (\frac{4}{\pi})\ L_A = 2\ P_L$$

$$L_V = 2\ P_A$$

$$P_V = \tfrac{1}{2}\ L_V\ S_V = 2\ P_A\ P_L$$

These expressions can all be derived from basic principles[152].

Curvature of points on a pore perimeter would be a useful parameter for classifying shape. The curvature of an element of perimeter can be obtained by sweeping test lines, which are uniformly orientated, over the image, and counting the number of lines that form tangents with that element of the perimeter. The mean curvature is related to the number of tangents formed by the following equation:

$$\text{Mean Curvature} = \frac{2 \times \text{Total number of tangents}}{\text{Number of feature intercepts made by the test lines.}}$$

Very little work has been carried out in this field and, as yet, the curvature cannot be measured using a Quantimet.

5.3.9.2. Technique.

The Quantimet, an image analyzing computer, can be used for carrying out stereological analyses. Depending on the attachments available, many stereological parameters, including Feret diameters, i.e. maximum diameters in several directions, and shape factors can be calculated. The Quantimet can be interfaced with an optical microscope, a scanning electron microscope or an epidiascope taking either negatives or prints. It can be programmed to carry out the

required measurements in any order, and programmed to compute and further process the measurements if necessary. For studying the porosity in graphite, the graphite can be impregnated with coloured resin under vacuum, as described in Section 5.2.1. (sample preparation, optical microscopy).

For a given graphite sample about 300 fields of view must be examined to obtain a statistical analysis of the pore system. The parameters measurable on a basic Quantimet are averaged over each field, which is meaningless for pore-shape analyses. For this study, the basic parameters needed from the Quantimet are: perimeters, areas, and diameters, at least in the vertical and horizontal direction, of individual pores. These three can be correlated to obtain a basic shape-factor;

$$\underline{\text{i.e.}}\ \text{Area} : \text{Perimeter}^2$$

$$\text{Perimeter} : \text{Diameter},$$

in order to identify each pore by a set of numbers.

To obtain measurements on individual features, the Quantimet must have a feature data module attached to it. Once the feature data module is attached, a calculator interface or a light pen image editor can be used to obtain individual measurements. The calculator interface slows down the Quantimet so that the output can be processed through a calculator or a computer. Without the calculator interface the data from the individual pores cannot be processed.

The light-pen image editor can be pointed at the particular pore from which information is required. Measurements are made on one pore at a time and printed out. The light pen can be moved onto the next pore by means of a foot switch. This method takes much longer than using a calculator interface.

Preliminary work was carried out on the Quantimet 720 at B.C.R.A. Chesterfield. The Quantimet has a feature data module but until recently had no calculator interface or light-pen image editor. B.C.R.A. have carried out quantitative work on coke structures using the Quantimet 720[153], and were able to carry out preliminary work on graphites. The porosity was compared in eight different graphites, i.e. AGLMP, BAEL GCMB, AGLHP, Morgans EYC 9106, Lima, PGA L18, BAEL VQMB and BAEL VNMC. Each graphite was mounted in resin, with the surface area for analysis with the Quantimet about 300 mm^2. The surfaces were polished, as for optical microscopy Section 5.2.1. but were not vacuum impregnated, i.e. there was no distinction between open and closed porosity.

5.3.9.3. Results.

The graphite samples were studied under an optical microscope attached to a Quantimet, with 200,000 picture points. The resolution was 0.77 μm, and each field studied was 1.2 mm x 1.2 mm. The instrument was programmed to give the total porosity and to categorize the pores and pore walls into eight selected size ranges:

>0 μm, >3 μm, >5 μm, >10 μm, >20 μm, >30 μm, >40 μm and >50 μm. The results obtained were processed through a computer to produce mean values for structural parameters, and standard errors. The results from the Quantimet are given in Table 5. These results give the total i.e. open and closed, porosity of the graphites down to 0.77 μm. The results are in the same order of magnitude, although obviously higher, for most graphite, than the open pore volumes down to 0.7 μm obtained from the pore distribution curves from mercury porosimetry measurements. The Quantimet results give the porosity, the pore and pore-wall sizes, the number of pores per field and the homogeneity of each graphite. Morgans EYC 9106 graphite had the smallest pores, the most pores per unit area, the largest pore surface area per given volume and was the most homogeneous. BAEL VQMB graphite was heterogeneous and gave variable measurements with high standard errors. AGLMP had the least number of pores per unit area.

To calculate the pore distributions, the number of pores that have their longest intercept greater than each size range are counted. These distributions are plotted on Rosin-Rammler paper and are given in Figures 142 to 149. The scale used is a log-log-reciprocal scale where y, the percentage oversize, is given by:

$$y = 100\left[1 - \exp\left(\frac{x}{k}\right)^{n}\right]$$ where n = slope of line

k = intercept when y = 36.79.

x = size in μm.

A log-log scale is used because as the pore size increases, the number of pores oversize decreases exponentially. Hence, a linear relationship between feature size and percentage oversize is obtained. On these graphs, (Figures 142 to 149), the percentage number of pores, pore intercepts and pore walls that are over each size, is given. The gradients of these distributions give a numerical indication of the shape and spread of the size distributions i.e. the greater the gradient, the more uniform the size distribution. It is probable that each distribution is best represented by two straight lines intersecting at an inflection point, rather than one line which would not pass through many points. This indicates that two overlapping size distributions exist which might possibly represent the distribution of the micropores within the wall material, and the distribution of the macropores greater than the size of the inflection point (in general about 10 μm). For two graphites i.e. PGA L18 and AGLHP, the graph representing the pore intercepts has no inflection point and has therefore, been drawn as one straight line.

For studying pores in the Quantimet, of size below 1.0 μm, electron micrographs are needed in conjuction with an epidiascope. Any magnification or size of print or negative can be used. The micrographs must have good contrast to distinguish between the grey levels representing pores and pore walls.

5.3.10. Progressive Polishing.

Progressive polishing was carried out on the two Gilso-carbon graphites in order to follow the pores through the graphite body. The depth of polish was measured using a travelling microscope. Figures 130 to 133 are micrographs (SEM) and stereopairs of AGLMP graphite before and after polishing away 10 μm of graphite. The pore (40 μm long) in the top-left corner of the micrograph, has opened up after polishing, from having a width of ~8 μm, to reveal a pore approximately spherical in shape, with a diameter of 24 μm. This pore has many slit-shaped pores (~2 μm wide) inside it, which, when viewed in three-dimensions (Figure 133), have a flakey appearance, as if the pores have been revealed by a thin sliver being lifted from the pore.

In Figure 130, the pore at the bottom of the micrograph appears to be separated from the large pore by a small (4 μm wide) piece of graphite, but in Figure 131, the two pores are joined together which shows that the pores were probably already joined below the surface in Figure 130. Figures 134 and 135 are micrographs of another area of AGLMP graphite, before and after removing about 6 μm during polishing. Here the two large pores (~80 μm long), are joined by a long, thin pore (40 μm long, 2 μm wide), which becomes more evident after polishing (Figure 135). The long, thin pore (2 μm wide) below this interconnecting pore is also opened up

during polishing and also connects the two larger pores. The slit-shaped pores inside the macropore, again appear to have a thin sliver of graphite down one side.

Figures 136 to 139 are micrographs (SEM) and stereopairs of BAEL GCMB graphite, before and after polishing about 10 μm away. The polishing has closed down several long, thin pores (1 μm to 2 μm wide) and has only opened up about two new pores (Figure 137). The pores within the large pore (100 μm wide) measure between 0.5 μm and 3 μm wide, and 5 μm to 30 μm long. These pores sometimes have smaller pores leading from them measuring about 100 nm (not resolvable at this magnification). These long, thin pores do not have the flakey appearance present in AGLMP graphite. Figures 140 and 141 are micrographs of another area of BAEL GCMB graphite, before and after polishing about 10 μm away. The large pore (500 μm long) has changed very little during polishing, although several small pores (~ 2 μm wide) have been revealed on the graphite surface.

Pores can be followed through the graphite by progressive polishing, but it is a time-consuming tedious process. Gilsocarbon graphites were studied for this process because they have more pores, within large pores, than the other graphites. Hence, the pores can more readily be followed through the graphite body.

5.4. Discussion of Results.

The optical micrographs (Figures 3 to 8) and the low magnification scanning electron micrographs (Figures 10, 12, 17, 22, 27, 32 and 37) show that there are distinct differences between the six graphites. The stereopairs of the virgin graphites (Figures 11,19, 24, 29, 34 and 39) are all taken at the same magnification for comparison and give a three-dimensional image of each graphite.

5.4.1. Optical Microscopy.

Each graphite has a characteristic pore structure which is related to the manufacturing materials and processes. Examination of the optical textures of the graphite enable characteristics of the graphite components to be studied. The six graphites examined fall into three categories: graphites manufactured from Gilso-carbon, unipore graphites and graphites manufactured from petroleum coke. The Gilso-carbon graphites, i.e. AGLMP and BAEL GCMB (Figures 3 and 4) have the characteristic Gilso-carbon structure, with small, individual mozaics of texture compounded into spherules (300 μm to 700 μm diameter) in which there are established super-mozaics. There is a large irregular pore in the centre of the spherule with small pores (< 5 μm) amid the mozaics.

These small pores are shrinkage cracks, which have some relation to the basic units of composition and which will be developed during graphitization, (probably formed at the mesophase - semicoke stage). In general, AGLMP has a macropore size greater than GCMB graphite. This has been confirmed using the Quantimet image analyzer (Table 5) (24.6 μm compared with 16.8 μm for the average pore intercept).

The unipore graphites, i.e. AGLHP and Morgans EYC 9106, (Figures 5 and 6) have a more uniform structure with higher total porosities (Table 5), than the Gilso-carbon graphites. Their optical textures consist of a smaller mozaic size with isotropic areas (smooth purple) between several of the pores (Figure 6).

The petroleum coke graphites, i.e. Lima and PGA L18, (Figures 7 and 8) are heterogeneous and exhibit large isochromatic domains, with associated acicular pores (Figure 8). These acicular pores follow the flow-patterns of the plastic mesophase and are characteristic of this type of graphite. There are also many near-circular pores which could be formed due to bubble formation during the carbonization process.

Optical microscopy thus gives a clear indication of size/shape of polycrystallinity of the different types of graphite and their relative orientations in the material.

5.4.2. Scanning Electron Microscopy.

Scanning electron microscopy is advantageous over optical microscopy in that the scanning electron microscope has a larger depth-of-focus, and can be used at higher magnifications, enabling studies to be made on pores of size 100 nm to several hundred micrometres. The large depth-of-focus was utilized by taking stereopairs to obtain three-dimensional images of the samples. The micrographs, especially at low magnifications, show differences between the six graphites. The Gilso-carbon graphites have a large number of long, thin pores (1 μm to 10 μm wide) in the walls of the macropores, which may be shrinkage cracks produced during manufacture. The unipore graphites are more uniform (compare the standard errors in Table 5), have smaller pores and have more pores per unit area (Figure 27) than the other graphites examined. At higher mangifications, (Figures 25, 26, 30 and 31), as the pores are not very large (maximum 30 μm wide), it is difficult to take micrographs inside the pores, as in AGLMP and GCMB graphites. This is especially true for Morgans EYC 9106 graphite where the average pore intercept is only 8.1 μm (Table 5).

The petroleum coke graphites, i.e. Lima and PGA L18, exhibit irregularly-shaped pores which are not easy to classify. Lima graphite has large pores, (50 μm to 100 μm wide), some of which are

near spheroidal, (Figure 32). It also has small pores (~ 500 nm wide) which are acicular (Figure 36), but there are many different shapes e.g. elliptical, elongated, in between these two extremes (Figures 32 to 35). PGA L18 graphite has an uneven distribution of pores (Figure 37) in which there are flow areas (compare Figure 8) through the graphite bulk. PGA L18 graphite is slightly less heterogeneous in its pore size than Lima graphite (compare Figures 37 and 32). This is confirmed by the Quantimet results (Table 5) (slightly lower standard errors on the pore walls and pore sizes), although when looking at the higher magnification micrographs, (Figures 40 and 41), this fact may not, at first, appear true! PGA L18 is, nevertheless, heterogeneous compared with the unipore graphites, and exhibits different shapes of pores including near circular, elliptical and acicular shapes.

5.4.3. High-Voltage Transmission Electron Microsopy.

The high-voltage electron microscope did not give as much information about the graphite as anticipated. This was due to bad maintenance of the microscope which made focusing and manipulation of the sample difficult. Also, the fact that pieces of mercury vaporized during examination and were not always lying within the porous system, made the micrographs difficult to analyze. However, information on the porosity of Lima graphite was obtained, for pores of sizes 100 nm to 3 μm. The pores were well distributed between near spheroidal pores (100 nm to 800 nm diameter) and long,

thin pores (200 nm to 600 nm wide) (compare the long, thin pores in Figure 36).

5.4.4. High-Resolution Scanning Electron Microscopy.

High-resolution scanning electron microscopy enabled the meso-porosity of the graphites to be examined. Pores examined were in the size range 5 nm to 300 nm. It is difficult to compare these micrographs with micrographs taken using the Cambridge "Stereoscan", because another dimension of surface topographical detail is being examined. However, the high-resolution micrographs are comparable with the high-voltage electron micrographs. In Figure 50 (Lima graphite) spheriodal pores (200 nm to 300 nm diameter) are visible (compare Figures 46 and 49). The AGLHP unipore graphite has a rounded structure (Figures 62 to 64), which is quite different from the macro-structure seen in Figures 22 to 26. Even in the lower magnification high-resolution micrographs (Figure 61) this type of structure cannot be detected.

5.4.5. Metal Impregnation Methods.

The micrographs taken of graphites (non-oxidised) impregnated with metals (namely gold) showed a distinction between the open and closed pores which gave useful information for building up models of the different graphites. The Gilso-carbon graphites had large areas (300 µm to 700 µm diameter) of closed porosity which corresponded to the Gilso-carbon grist particles in the graphite. These areas

were often surrounded by open pores (Figure 76) which may correspond to the pitch binder used to manufacture the graphite.

- The petroleum coke graphites had areas with both open and closed porosity. Figure 79 (Lima graphite) shows a flow area, surrounded by open porosity. In an optical micrograph of Lima graphite impregnated with gold (Figure 70), there are pores which are incompletely filled, probably due to solidification of the gold before complete filling has taken place. There are two distinct types of pores in the micrograph. One, thin acicular pores (shrinkage cracks), which follow the flow-patterns of the plastic mesophase (Chapter 3) are seen in the centre of the micrograph. <u>It is relevant to note that these consist of both open and closed porosity</u>. Two, large near spheroidal pores, which could be due to bubble formation during carbonization of the fluid pitch, are seen on the left of the micrograph. These pores are closed.

5.4.5.1. <u>Oxidation of Impregnated Graphites</u>.

Impregnating the graphites with a metal, enables the graphite to be oxidized completely, having a metal open-pore replica behind for examination by electron microscopy. Micrographs of the gold replica show the shapes of individual open pores, giving a complex inter-connected system, due to the inhomogeneity of the graphites. Quantitative work on the scanning electron micrographs

is difficult because at low magnifications there is so much information present, and at high magnifications the area is so localized, that a large number of micrographs are necessary to obtain a representative picture of the bulk graphite. Stereopairs alleviate this problem to some extent, in that, when viewed stereoscopically, the three-dimensional image is simpler i.e. the positions of the gold particles with respect to each other can be located. Analysis is still difficult but it is possible to obtain shape/size information from instruments such as the EMPD 2, using stereopairs.

In the Gilso-carbon pore replicas, (Figures 108 to 115) there are many areas with no gold present, whereas the pore replicas of Lima and PGA L18 are very compact with gold, showing that these two graphites have a higher open pore volume than the Gilso-carbon graphites. This is confirmed by the open pore volume measurements obtained from mercury porosimetry (Table 1).

From this study of gold impregnated graphite samples, it is interesting to note that the closed pores have essentially the same shape and structure as the open pores.

5.4.6. Thermal Oxidation in Air.

From the micrographs taken of virgin AGLMP graphite, AGLMP oxidized to 5.4% weight loss and 10.5% weight loss, it is obvious

that there is a change in the surface topography of the graphites. The pores have opened up, especially the small pores (< 5 μm) to give a very pitted surface, in between larger pores (compare Figures 91, 92 and 93). The Gilso-carbon structure has also opened up, (Figures 88(b), 89(b) and 90(b)) to produce larger shrinkage cracks, which were probably present before oxidation, but were too small to be resolved at this magnification. From the micrographs (e.g. Figures 88(a), 89(a) and 90(a)), there is a gradual increase in porosity from virgin graphite, through graphite oxidized to 5.4% weight loss, to graphite oxidized to 10.5% weight loss.

5.4.7. Oxidation by Atomic Oxygen.

Oxidation by atomic oxygen is carried out at a low temperature and may resemble radiolytic oxidation. The atomic oxygen etches the graphite surfaces revealing different types of pore structures, (Figure 100). By understanding how atomic oxygen oxidizes the graphite, we can get an insight into how the graphite behaves under radiolytic oxidation, (see Section 3.5). Again, as with thermal oxidation, the pores within the Gilso-carbon structure have opened up during oxidation. The surface appears to have a flakey nature (Figure 101) with pores (100 nm to 200 nm wide) in between the flakes. This flakey appearance could be due to small pieces of graphite (1 μm to 2 μm wide) lifting away from the surface during oxidation. More information and understanding of this effect on

the surface will be gained by taking high-resolution micrographs, (see Section 6.5.3.).

Lima graphite, when oxidised with atomic oxygen, shows up the flow area quite distinctly (especially in the right-hand-side of Figure 104). The direction of oxidation is not random, but is associated with the optical texture and follows the flow anisotropy through the graphite. An area of the oxidised Lima graphite taken at a higher magnification (Figure 105) shows a pitted surface.

Atomic oxygen oxidizes graphitic materials in a different way to molecular oxygen. There are areas of preferential oxidation, i.e. some sections of the surface react at higher oxidation rates than other sections. Examples of the 'etching' processes of atomic oxygen are described in earlier publications[120, 122].

This 'etching' is illustrated by the optical micrograph shown in Figure 153, which is not a graphite surface, but is the surface of a semi-coke (HTT 800 K) from a mixture of 50% Gilsonite pitch and 50% A200 Ashland petroleum pitch. It was oxidized in atomic oxygen for three minutes at 300 K. Inspection of Figure 153, shows that there is preferential oxidation at the disclination centres i.e. Positions 1 and 2, where the oxidation pits occur at right angles across the disclinations, and are parallel to the layer planes.

These etch-pits are further illustrated by the micrographs in Figures 154 to 156. These are scanning electron micrographs, (where the optical texture is unfortunately not seen), taken of the surface of a semi-coke, (HTT 800 K), from a mixture of 75% Ashphaltine and 25% A200 Ashland petroleum pitch. This semi-coke was oxidized in atomic oxygen for fourteen minutes at 300 K. In these micrographs, etching has taken place extensively over the surface. Figures 154 and 155 show deep etch-pits, whereas Figure 156 (in between the deep etch-pits) has an overall rough surface.

These micrographs (Figures 153 to 156) show that attack by atomic oxygen is by no means uniform, but occurs preferentially, probably at disclinations, boundaries and shrinkage fissures. If radiolytic oxidation behaves similarly, porosity may be influenced by channelling as in Figures 153 to 156. This aspect of oxidation will be looked for in radiolytically oxidized specimens.

5.4.8. Photogrammetry.

Photogrammetry can be used for drawing out contours and profiles of the graphite surfaces, and measuring depths of pores, but it is a very time-consuming operation. The best use it can be put to, in this pore analysis problem, is to analyze metal pore replicas, left after oxidation of the graphite. Here, there is too much information to carry out analyses on scanning electron micrographs i.e. using the Quantimet, and therefore, using photogrammetry i.e. the EMPD 2, the shapes, sizes and relative positions

of the gold pieces can be established. Although the pore shapes can be drawn out visually, it may be better to use photogrammetry for drawing out certain classes or types of pores, when they have been classified.

5.4.9. Stereology.

Stereology will provide shape and size parameters for pores in different graphites. The Quantimet has been used to yield: porosities, pore sizes, pore intercepts, pore wall sizes, average perimeter per pore, number of pores per unit area and homogeneity for eight different graphites. The graphites are quite different (as seen from Table 5). Their pore shapes can be compared, e.g. Morgans EYC 9106 is the most homogeneous and has the most pores per unit area.

With suitable attachments, i.e. epidiascope, feature data module, programmable calculator, shape/size factors for individual pores can be measured. Pores can then be classified for each graphite. A large number of measurements are necessary for a statistically significant analyses. Progressive polishing was carried out on the Gilso-carbon graphites, in order to follow the pores through the bulk material. This could be coupled with the Quantimet, so that after each polish, the change in shape of the pores can be monitored. The Quantimet can yield a wealth of information, even from the preliminary test run shown in Table 5.

5.5. Diagrammatic Representation of Porosity.

An initial attempt at the graphic representation of the pore structures, in three types of graphite, i.e. Gilso-carbon, unipore and petroleum coke graphites, has been made in Figures 150 to 152. These diagrammatic models of the graphites give an idea of how the graphites can be distinguished and characterized by their pore structures.

A serious attempt has been made to create representative diagrams of porosity in the three types of graphite examined. The diagrams do not describe porosity in any single, defined volume-element but contain essential features to be found throughout the bulk of the sample. The 'box' representation of porosity facilitates pictorial description. To do otherwise would have presented too difficult a problem.

It is to be noted that the vertical dimensions of the pores are exaggerated by a factor of two to three, in order to create an effective three-dimensional model.

CHAPTER 6.

EXPERIMENTS INTO THE USE OF CO-ORDINATED OPTICAL AND SCANNING ELECTRON MICROSCOPY TO MONITOR THE GASIFICATION OF GRAPHITES

6.1. Introduction.

This Chapter describes experiments performed to study changes induced by gasification in surfaces of graphites using microscopic methods. The study was made in order to have available quantitative data describing changes of topography and porosity of graphite by gasification under controlled conditions.

Nuclear-grade graphites were gasified in air, carbon dioxide, atomic oxygen and atomic hydrogen. Optical and scanning electron microscopy were used to monitor the same area of the surface of the graphite before and after gasification treatments in order to correlate optical texture with the extent and location of gasification. This study studies gasification by carbon dioxide much more extensively than other gases.

The graphites were thermally oxidised, in air and carbon dioxide, in order, specifically, to monitor the further

development of porosity and the topography of the pore walls before and after gasification.

The graphites were oxidised in atomic oxygen to study the rather unique developments in porosity during oxidation with this species; this type of graphitic oxidation may have resemblances to radiolytic oxidation, as occurring in the nuclear reactor.

Gasification with atomic hydrogen was carried out to obtain comparative information on the behaviour of graphite including relative rates of reaction and to build up a knowledge of topographical and porosity changes occurring in this type of reaction.

6.2. Samples and Sample Preparation.

Three types of graphite were studied: Lima (a petroleum-coke graphite), Morgans EYC 9106 (a unipore graphite) and AGLMP (a Gilso-carbon graphite). The properties of these graphites are listed in Table 1 and their mercury pore-size distributions are given in Figures A9, A8 and A5 respectively.

The graphites were polished (without the use of resin) as for optical microscopy using the three grades of alumina powder (see Section 5.2.1.). The graphites were cut into

pieces small enough for scanning electron microscopy, (SEM) i.e. less than 1.0 cm x 1.0 cm x 0.5 cm high, and ultrasonically cleaned to remove any alumina paste, or cutting debris. Microscopy and gasification studies were then undertaken.

6.3. Experimental Methods.

Each sample was placed under the optical microscope and, using a micro-manipulator, a vertical and a horizontal line were made on the sample to correspond with the cross-wires in the eye-piece. This enabled exactly the same position to be located before and after gasification treatments. Two areas were marked with a vertical and horizontal line in case one position was lost during gasification. Optical micrographs were taken of each marked and recognizable area at increasing magnifications. Scanning electron micrographs were taken to characterize the marked areas before treatment. The graphites were not coated with gold for electron microscopy, so ensuring that the graphite surface was not contaminated. Traces of metal on the surface can catalyse the gasification reaction. However, there was some slight loss in resolution in the scanning electron microscope (caused by charging) due to the absence of gold coating.

After microscopy, the samples were placed in a boat, weighed and gasified either thermally, or with an atomic species at room temperature or about 300 K.

6.3.1.Thermal Gasification.

The graphites were thermally gasified in an electrical furnace at temperatures ranging from 800 K to 1,000 K. Air or carbon dioxide was passed through the furnace during the gasification, heating and cooling stages. Samples were gasified for various times dependant on the gas used. The sample was reweighed and optical and scanning electron micrographs taken of the marked areas in order to relate topographical features and porosity developments to original optical texture.

6.3.2.Atomic Gasification.

The atomic gases were produced using a "Microton 200" micro-wave power generator (see Section 5.3.7.3.2). The glass sample chamber which is part of a vacuum-line, was evacuated, and oxygen or hydrogen passed over the sample. The micro-wave cavity was placed directly over the sample. The gasification was carried out at about 300 K, for two to five minutes. After gasification the sample was reweighed and micrographs taken of the known, located areas.

6.3.3.Extended Studies of Gasifications in Carbon Dioxide.

Gasification took place at temperatures between 870 K and 1300 K. The samples were placed in the centre of the furnace; carbon dioxide was passed over the samples during

the heating and cooling stages to ensure that no air was present in the furnace. The samples were reweighed and the marked areas on the surfaces restudied using optical and scanning electron microscopy. Some of the graphites were gasified several times, the surfaces being studied after each gasification . A few flow rates (~400 $mm^3 s^{-1}$ to 700 $mm^3 s^{-1}$) of carbon dioxide were measured using a Meterate flow meter tube.

Ultrasonic testing was carried out on selected graphites. These will be described in Chapter 7.

6.4.Results.

Figure 156.1 is a graph showing the calibration of the hot-zone of the furnace. Table 6 describes gasifications that were carried out on the three graphites and the weight losses sustained during each treatment. Figures 157 to 262 show the micrographs taken at each gasification treatment. Table 7, gives weight losses sustained during further gasification by carbon dioxide carried out on the three graphites and the temperatures of each treatment. These weight losses are for each gasification and also cumulative values where two or more gasifications have been carried out on the same sample. Flow rates are given in Table 8. Table 9 relates each graphite with the figure

numbers of the corresponding micrographs, to facilitate location. In discussing the results, the three different types of graphite studied are compared at each temperature of gasification.

6.5.Discussion of Results.

6.5.1.Thermal Gasification in Air.

Figures 157 to 182 are micrographs of Lima graphite (LG1, LG2 and LG3) before and after gasification in air. Figures 183 to 189 are micrographs of Morgans EYC 9106 (MG1 and MG3) graphite before and after gasification in air. Figures 190 to 195 are micrographs of AGLMP graphite (AG1) before and after gasification in air.

Lima Graphite

Figures 157 to 162 are optical and scanning electron micrographs of one area of Lima graphite (LG1) before and after gasification in air at 973 K for one hour, giving a weight loss of 16.67%. The optical micrographs (Figures 157 and 158) show the optical texture of the graphite. Flow areas can be clearly seen as blue and yellow colours, i.e. they run parallel to the basal planes. A pore structure is marked A, which runs along a flow area. Many shrinkage cracks are associated with these flow areas.

After gasification the surface topography is obviously associated with the optical texture (Figures 159 to 162) revealing many pores lying parallel to the basal planes and following the flow areas. Position A is also marked on the SEM micrograph. Figures 161 and 162 show where the layers gradually bend over from a prismatic edge presentation to a basal plane presentation.

Figures 163 to 178 are optical micrographs and scanning electron micrographs of an area of Lima graphite (LG2) before and after gasification in air at 873 K for one hour, giving a weight loss of 2.35%. Figures 163, 164, 166 and 170 are taken at the same magnification; the scanning electron micrographs appear to be lower in magnification; this is because the sample has a 45^{o} tilt to obtain the best SEM image.

It is interesting to compare the same area before and after gasification with both the optical and the scanning electron microscope (Figures 163, 164, 167 and 171). A reference point is taken as the pore marked B (Figures 163, 164 and 167). To the right, at Position C and also at Position D there are areas of small mozaics as distinct from the flow anisotropy marked E. These types of areas of different optical texture and hence

structure oxidize quite differently as seen in Figure 171. The area beneath the tip of the pore (yellow on Figure 163) marked E, has not oxidized as much as the small mozaic area marked C. In this area C many small near-circular pores (~ 0.5 μm) have developed (compare Figure 167 with Figure 171). The area to the left of the flow area beneath the large pore Position D, also has many small pores (~ 0.5 μm) which have developed during oxidation.

It is interesting to note that at the boundary between Positions D and E (Figures 167 and 171), a gasification crack has developed right down the boundary. Higher magnification micrographs (Figures 173 to 178) were taken to illustrate the topographical differences between the areas of small mozaic, Positions C and D, and the flow anisotropy areas, Position E. In Figure 176, the gasification crack separating the two areas is clearly shown.

Figures 179 to 182 show an area of Lima graphite (LG3) before and after it has been gasified in air at 823 K for one hour, giving a low weight loss of 0.38%. These micrographs illustrate two phenomena; one, the loss of colour contrast after gasification, and two, that clear definition is lost by this small percentage weight

loss. The yellow and blue colours which represent the prismatic edges have faded throughout the surface after gasification, but the purple areas which represent the basal planes are as bright before as after gasification as at Position F. This could be due to the fact that the rate of gasification is higher at the prismatic edges than on the basal planes.

Morgans Unipore Graphite

Figures 183 to 187 show an area of Morgans EYC 9106 unipore graphite (MG1) before and after gasification in air at 973 K for one hour, giving a weight loss of 9.22%. It can be seen in Figures 184 and 185 that oxidation has taken place over most of the surface. In Figure 185 there is an area at the top of the micrograph Position G which has gasified much less than the rest of the graphite surface. This area corresponds to the purple area at the top of Figure 183, also marked G which is optically isotropic. This material could be isotropic in structure or it could be taken as a basal plane area. However, quantitative reflectivity measurements carried out in the optical microscope on this area and similar areas indicate that this is not a basal plane area . The reflectivity value taken at a wavelength of 546 nm, for a basal plane in graphite is about 30%, whereas these isotropic areas gave a reflectivity value of about 15% .

These isotropic areas are present in quite large volumes (~ 5%) in this graphite and may be a binder material which is used in manufacture. Figure 186 shows the two areas that have

gasified at different rates. The prismatic edge area at the bottom of Figure 186 has become very rough and the pore walls have also been oxidized as seen in Figure 187. During gasification many small pores (~ 0.5 μm) have developed both on the surface and inside pores which are open to the surface.

Figures 188 and 189 are micrographs of an area of Morgans unipore graphite (MG3) before and after oxidation in air at 823 K for one hour giving a weight loss of 0.11%. From these micrographs there is no visible change in the oxidized surface at this magnification, either in terms of colour contrast or definition (compare Figures 179 to 182, Lima graphite under the same conditions).

AGLMP Graphite

Figures 190 to 195 show an area of AGLMP graphite (AG1) before and after gasification in air at 873 K for one hour, giving a weight loss of 0.48%. The optical micrographs taken after gasification have lost colour contrast and definition due to the polished surface becoming rough and the reflectivity diminishing. In the micrograph (Figure 191) the blue areas have become white, Position H, and the yellow areas have faded, Position J, as also seen in previous micrographs of Lima graphite (Figures 181 and 182). Most features are lost because of the very low depth-of-focus present in an optical microscope.

The oxidation features are seen best in the scanning electron micrographs. At low magnification (Figure 192) the surface looks fairly smooth and there is little evidence of gasification as the effect is small. The positions of H and J are marked on Figures 192 and 193 to identify them with the optical micrographs. However, at higher magnifications (Figures 194 and 195) the surface is very pitted with many small pores (~0.1 μm wide), many of which are long and thin, and a few nearly circular.

The small pores (1 μm wide) developed during gasification by molecular oxygen are clearly associated with the small mozaic structures of the optical texture of Figure 190. The long, thin pores could be the enlargements of shrinkage cracks already present in the graphitic material.

6.5.2. Thermal Gasification in Carbon Dioxide.

Figures 196 to 215 are micrographs of Lima graphite (LG4 and LG6) before and after gasification in carbon dioxide. Figures 216 to 222 are micrographs of Morgans EYC 9106 graphite (MG4 and MG6) before and after gasification in carbon dioxide. Figures 223 to 232 are micrographs of AGLMP graphite (AG2) before and after gasification in carbon dioxide.

Lima Graphite

Figures 196 to 201 are micrographs of an area of Lima graphite (LG4) before and after gasification in carbon dioxide at 973 K for 16 hours, giving a weight loss of 0.83%. Figures 196 and 198 are taken at about the same magnification. Corresponding positions are marked K in both the optical and SEM micrographs. In these micrographs the complexity of the topographical changes created by gasification with carbon dioxide can be seen. Although corresponding areas can be identified in Figures 196 , 198 and 199, there is a need for a very careful, detailed analysis of each area to relate texture to topography.

The whole surface appears to be etched by the carbon dioxide forming channels (~ 0.5μm wide) which accentuate the texture and run parallel to the basal planes (Figure 201).

Figures 202 to 210 are high-resolution scanning electron micrographs taken using a JEM 100C with the ASID-4D scanning attachment. The micrographs are of Lima graphite (LG4) gasified in carbon dioxide at 973 K for 16 hours, giving a weight loss of 0.83%. Figures 202 to 205 show one area at increasing magnifications. Figure 203 is a similar area to those areas seen in Figures 200 and 201. Channelling of the surface has taken place during gasification. At higher magnifications of this surface, the whole area appears to have a spherical structure (Figures 204 and 205) with pores associated with these spheres.

These spheres may have been formed at the mesophase stage of manufacture. Their diameters are mostly 100 nm and smaller.

Figures 206 to 210 show another area of Lima graphite (LG4) gasified in carbon dioxide. This area is similar to the previous ares, with 100 nm spheres visible in Figures 208 to 210. In Figure 206 the channelling effect can again be seen, due to the gasification on the surface. In Figure 209, a pore with a narrow constricted neck can be seen on the right side of the micrograph, half-way down (marked 1). This is the type of pore known as an 'ink-bottle pore'. The larger pores present in Figures 209 to 210 represent the smallest pores that are being examined in this study (~ 50 nm).

Figures 211 to 215 are micrographs of an area of Lima graphite (LG6) before and after gasification in carbon dioxide at 873 K for 25 hours, giving a weight loss of 0.03%. There is little change in the topography of the surface during gasification, but it can be seen that in the optical micrographs, the blue and yellow colours have faded, Positions L and M. The blue colour appears to have faded more than the yellow, but that may be due to the colour composition, rather than the blue areas becoming more gasified than the yellow areas. The purple colour representing the basal plane areas has remained the same after gasification, Position N. The scanning electron micrographs (Figures 213 to 215) show no sign of gasification attack, even at high magnifications.

The colour sensitivity is more developed than the topographical change induced by oxidation.

Morgans Unipore Graphite

Figures 216 to 220 are micrographs of Morgans EYC 9106 unipore graphite (MG4) before and after gasification in carbon dioxide at 973 K for 16 hours, giving a weight loss of 0.67%. The smooth purple area, Position P, in the optical micrograph is an isotropic material which is only attacked very slightly by oxidation. At low magnifications (Figure 217) the surface appears quite smooth, but at higher magnifications, in a small mozaic area, Position O, (Figures 218 to 220) the surface is quite rough. There are two types of gasification attack, as seen in Figure 218. One is on the isotropic material, Position P, and the other is on the small mozaic area, Position O. The carbon dioxide has attacked the isotropic material to a lesser extent (Figure 219) than the small mozaic area (Figure 220).

Figures 221 and 222 are micrographs of Morgans EYC 9106 graphite (MG6) before and after gasification at 873 K for 25 hours, giving a weight loss of 0.02%. These micrographs show that there is no change in the optical texture, or the surface topography at this magnification. (Compare Figures 211 and 212, which are areas of Lima graphite (LG6) gasified under the same conditions, but giving a loss in the interference colours).

AGLMP Graphite

Figures 223 to 232 are micrographs of AGLMP graphite (AG2) before and after gasification in carbon dioxide at 973 K for sixteen hours giving a weight loss of 0.40%, and 1073 K for sixteen hours giving a further weight loss of 0.76%.

The interference colours (Figure 224) have become quite dull after gasification at 973 K, although the pore structure is quite clear after gasification.

The scanning electron micrographs (Figures 225 to 228) show signs of gasification at high magnification (Figures 227 and 228) where the surface is pitted. The graphite surface has white patches on it, which could be due to irradiation damage in the electron microscope, together with slight charging of the specimen, due to the specimen not being gold coated. The area Q which is marked in both the optical and the scanning electron micrographs lies on a boundary line around the edge of the Gilso-carbon structure. This area is a band of small mozaics as seen in Figure 223. After oxidation the mozaic structure has almost disappeared (Figure 224) and the area has become pitted with pores (~ 100 nm wide) (Figures 227 and 228).

Figures 229 to 232 are scanning electron micrographs of AGLMP graphite (AG2) after gasification at 1073 K for sixteen hours. The surface has become well pitted during gasification giving a very flakey appearance (Figure 232). The area studied at high

magnification, an area between two pores, has collapsed (Figure 232) and the pores have all joined up leaving very thin slivers of graphite on the surface. Many pores (~ 1 μm wide) have appeared around the Gilso-carbon structure, (Figure 232) which lie parallel to the pores already present. These pores may have been created, during gasification or they could be pores which have become enlarged and were beyond the resolution of the microscope before gasification.

6.5.3. Gasification in Atomic Oxygen.

Figures 233 to 257 are micrographs of Lima graphite (LG7 LG8 and LG9) before and after gasification in atomic oxygen at room temperature.

Figures 233 to 242 are micrographs before and after gasification for five minutes (LG7) giving a weight loss of 0.98%. Figures 233 and 234 were taken at similar magnifications. Corresponding Positions R and S are marked. The channelling effect over the whole surface in Figure 234, is associated with the optical texture seen in Figure 233. The area in Figures 235 and 236 is an area of flow-type anisotropy around Position S. Oxidation has taken place inside the pores, as seen in the pore at the top of Figure 235 (above Position S). The structure inside this small pore (~ 5 μm) looks similar to the surface structure, but a higher magnification micrograph is necessary to establish this.

Figures 237 to 242 are high-resolution micrographs taken of Lima graphite (LG7) after gasification in atomic oxygen at about 300 K for five minutes. These micrographs again show the spherical structure with spheres of diameter about 100 nm, many of which have agglomerated to form larger spheres, leaving thin pores (~ 10 nm) in between the individual spheres (Figure 242).

The micrographs (Figures 237 to 242) are taken of an area of Lima graphite (LG7) showing the effect of the gasification (Figure 237). The structure inside the pore in this micrograph is channelled similarly to the surface. The top of Figure 238 shows how rough the pore wall is. This area is magnified in Figures 240 to 242. The pore wall is made up of spheres about 100 nm diameter which have pores associated with them.

Figures 243 to 250 show an area of Lima graphite (LG8) before and after gasification in atomic oxygen at about 300 K for three minutes, giving a weight loss of 0.57%. In the scanning electron micrographs the effect of gasification is seen by comparing Figures 246 and 247 with Figures 249 and 250. Corresponding positions are marked T. The channelling parallel to the basal planes has opened up many long thin pores in Figure 250, of size about 100 nm. In the optical micrographs the texture has become very dull, e.g. Position U, making it difficult to distinguish between the different optical textures.

Figures 251 to 257 are micrographs of Lima graphite (LG9) before and after gasification in atomic oxygen at about 300 K for two minutes, giving a weight loss of 0.15%. The interference colours have again faded, although the yellow colour, Position V, has not faded as much as the blue colour, Position W. Many areas which were originally blue, are yellow after oxidation.

In the scanning electron micrographs (Figures 255 to 257) the gasification effect can be seen at high magnifications (Figures 256 and 257). Many long pores (~ 100 nm wide) have developed on the surface giving a channelling effect which follows the texture of the graphite surface.

6.5.4. Gasification in Atomic Hydrogen.

Figures 258 to 262 show an area of Lima graphite (LG10) before and after gasification with atomic hydrogen at about 300 K for twenty minutes, giving a weight loss of 0.08%. The optical micrographs before gasification (Figure 258) and after gasification (Figure 259) show that the yellow interference colour has faded, Position X, the blue colour has faded to a creamy-white colour, Position Y, and some of the purple areas (basal planes) have remained purple, Position Z_1. Other areas of purple have changed colour, Position Z_2 ; these are the purple areas representing the prismatic edges, half-way between blue and yellow colours.

Figures 260 to 262 are scanning electron micrographs of Lima graphite (LG10) after gasification in atomic hydrogen. The gasification on the surface is only visible at high magnifications (Figure 262). Here the surface pitting can be seen, with small pores about 100 nm diameter developing on the surface.

6.5.5. Extended Studies of Gasifications in Carbon Dioxide.

Figures 263 to 289 show micrographs of the three graphites (LG12, MG7 and AG5) gasified in carbon dioxide at 1073 K for sixteen hours, giving the following weight losses: Lima graphite 1.64%, Morgans unipore graphite 0.60% and AGLMP graphite 1.34%. From both the weight loss and a study of the micrographs, it can be seen that Lima graphite is the most reactive.

Figures 263 to 270 show Lima graphite (LG12) before and after gasification. In the optical micrographs, Figures 263 and 264, the surface has changed so much that the areas are almost uncomparable. With careful study it is possible to relate certain areas, i.e. Position A, which is a pore. The surface in Figure 264 has become very porous. The pores are depicted as black or green areas on the micrograph. The black pores are very shallow pores (~ 1 μm to 2 μm deep) and the green pores are deeper (~ 10 μm to 20 μm deep). Most of the black areas are pores which have appeared during gasification.

Position A is marked on the scanning electron micrographs. Again the surface has changed a great deal during gasification. Many long thin fizzures, ranging from 100 nm to 1 μm wide have appeared over the whole surface (Figures 269 and 270). In Figure 269 below Position A, there is a herring-bone structure of fizzures. This appears to correspond to a yellow area in the optical micrograph (Figure 263), although complete correlation is difficult because the surface has changed so much. Above the herring-bone structure is a smooth non-porous structure which corresponds to a purple area in the optical micrograph. This is a basal-plane area, which has not become heavily oxidised. Figure 270 shows very thin layers of graphite left after gasification, measuring about 200 nm.

At low magnifications (Figures 265 and 268) it can be seen that the larger pores (20 μm to 50 μm diameter) have remained the same size during gasification, whereas smaller pores (1 μm to 10 μm) have become larger, by a factor of two or three. However, the much smaller pores (~ 50 nm to 200 nm) (Figures 266 and 269) have increased their size by ten or more, and many did not appear to exist before gasification.

Figures 271 to 276 show an area of Morgans unipore graphite (MG7) before and after gasification in carbon dioxide at 1073 K.

Again the surface has changed considerably as seen in the optical micrographs (Figures 271 and 272). The area marked B shows a pore at the edge of a purple area and a mozaic area. This area is also marked on the scanning electron micrographs.

The area which is purple in the optical micrographs does not stand out in the scanning electron micrographs (Figures 273 and 274) before gasification, but after gasification (Figure 275) it is very distinct as it does not oxidise to the same extent as the mozaic areas. The purple area is not a basal plane area because of its reflectivity properties which were discussed in Section 6.5.1.(p.154). It is an isotropic material which is found extensively in this graphite, and remains fairly smooth during gasification.

The mozaic areas gasify non-uniformly, leaving short thin pores (~ 1 μm long and 200 nm wide). None of the pores are very long apart from a few along the boundary between the different optical textures, which are about 5 μm long. Again the large pores remain unchanged during gasification.

The scanning electron micrographs give very bright edges to the bottom side of the pores. This is due to charging of the specimen during examination. The samples were not coated with a conducting material, giving rise to slight loss in resolution.

Figures 277 to 284 show an area of AGLMP graphite (AG5) before and after gasification in carbon dioxide at 1073 K. The surface topography has only changed slightly compared with the previous two graphites, as seen in the scanning electron micrographs (Figures 280 and 283). The optical micrograph has changed colour completely (Figure 278) to all purple, but the purple does not have the same intensity as the purple seen in the virgin graphite (Figure 277). The surface features are still present, and stand out through the purple colour i.e. Position C.

This colour could possibly be due to formation of the surface oxygen complex during the following reaction:

$$C + CO_2 \rightarrow CO + C(O)$$

which is an intermediate reaction on the surface during gasification of graphite with carbon dioxide. (This is described in Section 3.2). The surface oxide will alter the electronic structure of the basal planes and may produce the purple colour as seen in the polarized light microscope. The surface complex may be removed by polishing the surface very lightly, and by heating to higher temperatures in vacuum or an inert gas, or by heating in hydrogen. The loss in colour may be due simply to the induced surface roughness following gasification.

In the scanning electron micrographs (Figures 279 and 282) there are signs of slight gasification on the surface. Small pores (~ 500 nm wide) are starting to appear and the long thin pores (~ 100 nm wide) at Position C are becoming more prominent.

This sample was gasified further to a temperature of 1198 K, having a weight loss of 3.44%. Figures 285 to 289 show scanning electron micrographs of the area after further gasification. Optical micrographs could not be taken because the surface was too rough to obtain a clear image.

From the scanning electron micrographs (Figures 285 to 289) it can be seen that the surface topography has changed a great deal during gasification. Many pores have appeared at the surface, which accentuate the surface structure, especially the area shown in Figures 288 and 289. This area is seen in Figure 277 Position C. In this micrograph the area was depicted by a yellow flow area. The pores developed (Figure 288) during gasification run parallel to the layer planes. The long thin pores (~ 2 µm wide) developed during

gasification are quite deep (~ 3 μm). The same pores before gasification had no depth to them at all (Figure 281). Figures 284 and 289 taken of the same area, are difficult to recognize as such, due to the extent of gasification. In Figure 289, thin (100 nm) sheets of graphite are well defined.

Figures 290 to 304, show micrographs of two of the graphites; Lima (LG13) and AGLMP (AG6), before and after gasification in carbon dioxide at 1088 K for forty-eight hours and 1173 K for sixteen hours. The weight losses sustained during the two gasifications are: Lima graphite 1.42% and 2.63% and AGLMP graphite 0.48% and 1.39%. Again, Lima graphite is the most reactive. The flow rate of carbon dioxide was 500 mm^3 s^{-1}.

Figures 290 to 296 show Lima graphite (LG13). Optical micrographs were not taken before gasification but Figure 290 shows the graphite after gasification at a temperature of 1088 K. It is noted that there is no blue colouration in the micrographs. This is due to a colour change during gasification. The blue colour has become a cream colour, Position D, but the yellow colour has remained yellow, Position E. This could be due to a change in the adsorptive properties on the surface of the graphite.

Positions D and E are also shown on the scanning electron micrographs, but they do not stand out in the micrographs taken

before gasification (Figures 291 and 292). After gasification at 1088 K (Figures 293 and 294) many gasification fizzures (~ 200 nm wide) have appeared, following the optical texture of the graphite surface. This is seen clearly in Figure 293. At Position D the gasification fizzures are parallel to a north-east direction up the paper, whereas at Position E the gasification fizzures are paralled to a south-east direction, i.e. they are at right angles to each other. This is consistant with the fact that the gasification fizzures run parallel to the basal planes and that the cream colour (previously blue) indicates basal planes orientated at right angles to the basal planes in the yellow areas.

After further gasification the fizzures have widened to about 500 nm (Figures 295 and 296) and a few more fizzures have appeared. The area below the pore next to Position D (Figure 296) is a purple area and is quite free of gasification fizzures. This could be an area where the basal planes are running parallel to the surface under observation, and none or very little gasification has taken place (see Figure 1. for an analysis of the interference colours). This purple area should not be confused with the area at Position F which is purple and indicates an orientation of the basal planes which is half-way between blue and yellow, hence giving basal planes and gasification fizzures in a north-south direction (Figure 295).

Figures 297 to 304 show AGLMP graphite (AG6) before and after gasification in carbon dioxide at 1088 K and 1173 K. The optical micrographs (Figures 297 and 298) show very little change after gasification. The pore, Position G, has changed appearance, and become more diffused (Figure 298) after gasification. The pore is no longer in focus due to gasification of the pore wall. There were no scanning electron micrographs taken before gasification, but Figures 299 to 301 show the surface after gasification. Around the pore, Position G, there are many fizzures (~ 100 nm wide) which account for the diffused appearance of the pore in Figure 298.

After further gasification more fizzures develop (Figure 303) which are about 150 nm wide. The fizzures already present have become slightly larger (~ 500 nm). The extent of gasification is not quite as great as with Lima graphite under the same conditions (Figures 295 and 296).

Figures 305 to 333 show micrographs of the three graphites (LG14, MG8 and AG7) gasified in carbon dioxide at 1138 K and 1223 K for sixteen hours each. The following weight losses were sustained during gasification: Lima graphite 2.00% and 9.40%, Morgans unipore graphite 0.85% and 7.57%, and AGLMP graphite 0.81% and 2.28%.

Figures 305 to 313 show Lima graphite (LG14) before and after gasification. In the optical micrographs (Figures 305 and 306) there is very little change in the optical texture after

gasification at 1138 K. This is confirmed by studying the scanning electron micrographs (Figures 308 to 311) which show that there is no change in the surface topography apart from the development of an occasional fizzure, below Position H, (Figure 311). The width of the fizzure is about 50 nm.

On further gasification the surface changes a great deal as seen in the optical micrograph (Figure 307) and the scanning electron micrographs (Figures 312 and 313). In Figure 307, the blue and yellow areas, corresponding to prismatic edges have disappeared but the purple colours still remain. The black lines to the right of Position H are shallow pores which have been enlarged during gasification. Their depth is about 1 μm to 2 μm. The green colour represents deeper pores (~ 10 μm to 20 μm deep) which were already present before gasification. The disappearance of the blue and yellow colours could be due to preferential oxidation taking place on the prismatic edges, rather than on the basal planes. The area is difficult to identify because the surface is rough and the depth of focus is low in the optical microscope.

In the scanning electron micrographs (Figures 312 and 313) the gasification fizzures follow the optical texture as in the area to the right of Position H. This area was purple before gasification, representing half-way between blue and yellow orientations. The pores are about 1 μm wide and about 100 μm to 150 μm long.

Many shorter pores, which are about 10 μm long, have also appeared during gasification. Gasification attack on the pore wall can be seen by comparing Figure 313 with Figures 309 or 311.

Figures 314 to 321 are micrographs of Morgans unipore graphite (MG8) before and after gasification. Position J marks the pore which has been observed at higher magnifications. There appears to be no change in the optical texture and the topography before and after gasification at 1138 K. The only observed change was the development of a fizzure seen in Figure 319. In Figure 317 a thin pore was barely visible, Position J, but after gasification the width of the fizzure could be measured as about 70 nm. A pore which was filled with loose graphite particles (above Position J in Figure 316) has lost the loose graphite during gasification (Figure 318) and a piece of debris on the surface above the loose particles has been removed and left a light area on the graphite surface. This debris could have influenced the gasification reaction (e.g. a piece of alumina powder may possibly catalyse the reaction).

After further gasification, the surface topography is completely changed (Figures 320 and 321). The whole surface has become covered with very small pores (~ 100 nm to 200 nm wide). In Figure 321 a large amount of graphite has disappeared, and two pores that were previously linked by a very thin pore (< 100 nm in Figure 317), Position J, are now joined together by a pore about 2 μm wide.

Figures 322 to 333 are micrographs of AGLMP graphite (AG7) before and after gasification giving a weight loss of 0.81%. Again, in Figures 322 to 329, there is very little change in both the optical texture and the topography after gasification at 1138 K. The pore, Position K, is marked for identification. Figure 323 is slightly darker in colour than Figure 322, which could be due to a slight loss in reflectivity of the polished surface. The high-lighted areas in the scanning electron micrographs e.g. Figures 324 and 327, are due to electrostatic charging on the graphite surface, caused by non-coating of the surface with a conducting material.

Figures 330 to 333 are scanning electron micrographs of sample AG7 taken after further gasification at 1223 K. In these micrographs the whole surface is pitted with very small pores, which are less than 100 nm wide and 1 μm long. In Figure 333, the interior of the pore wall can be seen, and small fizzures (100 nm wide) are present running along the wall. The pore wall has gasified in a similar way to the graphite surface.

Figures 334 to 341 are micrographs of Lima graphite (LG15) before and after gasification in carbon dioxide at 1173 K and 1223 K for sixteen hours each. The weight losses sustained during gasification were 3.65% and 9.29%. The flow rate of the carbon dioxide was 700 mm^3 s^{-1}. The optical micrographs (Figures 334 and 335) show a complete colour change after gasification. The surface is isotropic, as shown by the purple colouration.

Although the optical texture of the surface has changed completely, the topography has changed only slightly (compare Figure 336 with Figure 338). Position L has been marked on the micrographs. A few small pores (~ 100 nm wide) have developed on the surface as seen in Figure 338. These pores are very narrow (~ 100nm) and extremely shallow. They are only just detectable as a pore, even at high magnifications (Figure 339).

On further gasification the surface became completely pitted with small pores (Figures 340 and 341) which were not at all evident after the first gasification. Optical micrographs could not be taken at this stage because the surface was too rough. Many of the pores are about 50 μm long and 200 nm wide. The larger pores (20 μm wide) have not changed during gasification but one pore, Position M, has almost disappeared after this further gasification (Figures 338 and 340). This is because it was a shallow pore (~ 2 μm) and it has become incorporated into the roughness of the surface.

The pores at the bottom of Figure 341 (~ 300 nm) were beginning to appear in Figure 399, but many, especially on the pore wall at the top of Figure 341 appeared after the second gasification at 1223 K. They have developed to the same size as the pores at the bottom of Figure 341 (200 nm to 300 nm wide). The pattern of the pores in Figures 340 and 341

are related to the optical textures seen in Figure 334 before gasification. Around the pore Position M, there is a yellow flow area. This area has become covered with long thin pores (~ 200 nm wide) running parallel to the basal planes. There is a mozaic area to the right of this, above a large pore, Position N. After gasification the developed pores in this area are not all in one direction, but change direction many times.

Figures 342 to 367 are micrographs of samples (LG16, MG9 and AG8) after gasification in carbon dioxide at 1198 K and 1273 K for sixteen hours at each temperature. The weight losses sustained were: Lima graphite 5.31% and 37.65%, Morgans unipore graphite 1.40% and 16.19%, and AGLMP graphite 1.07% and 8.12%.

Figures 342 to 351 show Lima graphite (LG16) before and after gasification. The optical micrographs (Figures 342 and 343) have lost the interference colours during gasification. This indicates that the surface topography has changed, together with the adsorptive properties of the surface. The pore shapes are still detectable, although the detailed surface structure has disappeared. Position O, marks the position of a pore seen in most of the micrographs.

In comparing the scanning electron micrographs (Figures 344 to 349) it can be seen that after gasification the surface is rougher, and pores have developed as seen in Figures 348 and 349. Most of the developed pores are less than 50 nm wide, one pore just below Position O is larger (0.5 μm wide).

After further gasification (Figures 350 and 351) the surface has changed a great deal, especially around the centre of Figure 350. The surface was too rough for optical micrographs to be taken. At higher magnifications, the area became barely recognizable (Figure 351) with pieces of graphite (~ 2 μm wide) flaking off the surface. The interior of the pores can be seen in Figure 351. The pore walls contain thin slit-shaped pores which are about 1 μm wide. Higher magnification micrographs were not taken because there were many loose pieces of graphite on the surface which made focussing very difficult.

Figures 352 to 359 show Morgans unipore graphite (MG9) before and after gasification. There was no change in either the optical texture as seen in Figures 352 and 353, or the surface topography as seen in Figures 356 and 357, after 1.4% weight loss. Position P is marked on the micrographs for identification.

Figures 358 and 359 show Morgans graphite (MG9) after further gasification. The whole surface has become covered with very small pores (~ 200 nm to 300 nm wide). There are a few areas which have not become as pitted during gasification as most of the surface. These areas are seen as plain purple areas in the optical micrographs (Figures 352 and 353) i.e. they are pieces of isotropic material which could be inerts present in the starting material. This area is seen in Figure 359, it is much more porous after gasification (compare Figures 355 and 357) having pores about 100 nm in diameter, but it

has not gasified to the same extent as the mozaic surface which is seen at the bottom of Figure 359. This type of area which covers most of the surface has many pores 200 nm wide and 2 μm long.

Figures 360 to 367 show AGLMP graphite (AG8) before and after gasification. The optical texture as seen in Figures 360 and 361 has changed during gasification. Many of the yellow areas have become purple around the pore marked Position Q. This is a surface effect which is not seen in the scanning electron micrographs (Figures 364 and 365). It could be a very thin layer of surface oxide which affects the optical texture but not the topography, giving a change in the adsorptive properties of the surface.

After further gasification the surface has become very rough. Several large pores have developed which are about 5 μm to 10 μm diameter e.g. the pore below Position Q in Figure 366. These pores must have been just below the surface before gasification as it is unusual for pores of this size to develop during gasification. Many smaller pores (~ 300 nm wide) have developed on the surface.

At Position R there is a band going across the micrograph this is seen as a distinct line in the optical micrograph (Figure 360) before gasification, and as a less distinct line after gasification (Figure 361). This is the boundary of the Gilso-carbon

area which is generally not seen on scanning electron micrographs (Figure 362) but after heavy gasification (Figure 366) it is seen as a band which has not oxidised to the same extent as other areas i.e. it is not pitted with pores (500 nm wide) as much as the rest of the surface.

Figures 368 to 385 show micrographs of the three graphites (LG17, MG10 and AG9) before and after gasification at 1243 K for sixteen hours, giving the following weight losses: Lima graphite 5.99%, Morgans unipore graphite 6.04% and AGLMP graphite 3.30%.

Figures 368 to 373 show Lima graphite (LG17) before and after gasification having a weight loss of 5.99%. The optical texture has changed completely and the surface has become isotropic (Figure 369). There are many long, thin pores (~ 1 μm wide) covering the surface, especially along the blue flow areas seen in Figure 368. Position S marks a pore which can be seen in both the optical and scanning electron micrographs. The green colouration in Figure 369 depict most of the larger pores (> 5 μm deep) already present before gasification (Figure 368). The black areas are smaller pores (< 2 μm deep) many of which have developed during gasification.

In the scanning electron micrographs (Figures 370 to 373) the topography is quite different after gasification (Figures 372 and 373). Many long, thin pores (~ 200 nm wide) have developed along the flow areas i.e. parallel to the basal planes.

In Figure 373 there is a 90° change in direction of the pores as the basal planes change direction. This is depicted in the optical micrograph (Figure 368) as a blue flow area, with a yellow area (8 μm wide) adjacent to it, by Position S. The high magnification micrographs (4,300 X) (Figures 371 and 373) show no resemblance to each other, because the surface has changed so much. The flow area can just be detected at the top of Figure 371, before gasification.

Figures 374 to 379 are micrographs of Morgans unipore graphite (MG10) before and after gasification giving a weight loss of 6.04%. Position T marks the area which has been studied. In the optical micrographs the pore structure is well defined after gasification, but the optical texture has become quite dark and ill-defined. Around Position T the optical texture has a mozaic structure. On gasification, this type of structure behaves quite differently from the flow areas in the previous sample. This is seen in Figure 379, where many short, thin pores (200 nm wide) have developed during gasification. The pore in the centre of Figures 377 and 379 has enlarged slightly during gasification from 200 nm to 300 nm, but larger pores (> 1 μm wide) have remained the same size after gasification. Pores of size 100 nm after gasification have opened up from about 50 nm size i.e. above the centre pore in Figure 377.

Figures 380 to 385 are micrographs of AGLMP graphite (AG9) before and after gasification in carbon dioxide at 1243 K for sixteen hours to 3.30% weight loss. The micrographs show one side of a Gilso-carbon pore structure. At a position marked U the Gilso-carbon boundary, can be seen. This may be the 'glue' used for 'glueing' the Gilso-carbon particles during manufacture. In many of the optical micrographs the 'glue' is depicted by a mozaic band around the Gilso-carbon structure (see Figure 360). This structure behaves differently from the adjacent area during gasification. The boundary is still visible in the optical micrograph after gasification (Figure 381) although most of the other optical textures have disappeared.

In the scanning electron micrographs (Figures 382 to 385) many fizzures have appeared during gasification. The Gilso-carbon boundary stands out as having fewer pores after the gasification reaction, than other areas on the graphite surface. In between the large slit-shaped pores (at the top of Figures 382 and 384) small pores (200 nm wide) have developed, which are parallel to the large pores (2 μm to 3 μm wide) already present. A change in direction of the gasification fizzures is indicated by a change in the interference colours in the optical microscope i.e. a change in the optical texture of the graphite surface. In Figure 385, the gasification fizzures are all running in a direction parallel to the pores already present.

Two graphite samples, Lima graphite (LG18) and AGLMP graphite (AG10) were gasified in carbon dioxide at three temperatures (873 K, 973 K and 1073 K) over long periods of time (96 hours) at constant flow rate of carbon dioxide, (700 mm^3 s^{-1}). The purpose was to compare pore development, at increasing weight losses, in graphites oxidised at different temperatures, using the same piece of graphite.

Figures 386 to 400 show micrographs of Lima graphite (LG18) giving weight losses of 0.45%, 3.23%, 1.34% and 4.89% before and after successive gasifications. In the optical micrographs the optical texture has changed after each gasification, as seen in Figures 386 to 388. The surface structure has also changed even after the first gasification, at 873 K for sixteen hours giving a weight loss of 0.45%. This change is seen to the left of Position V in Figures 387 and 393. In Figure 387 many of the blue areas have lost their colour, but the yellow areas remain. At the present moment there is no explanation why the blue colouration should be lost before the yellow colouration, as the structure of these two areas are the same, the only difference being a 90% change in the orientation. The pore structures in Figure 387 are less well defined after gasification due to loss of the polished surface and hence reflectivity around the edges of the pores.

In the scanning electron micrographs (Figures 389 to 394) the surface topography has changed slightly after the first

gasification. Gasification fizzures have appeared in Figures 393 and 394. These are between 50 nm and 100 nm wide, and are visible all over the surface (Figure 394). In Figure 393, certain areas stand out because they are affected by gasification in different ways. These differences are related to the optical textures of the surface as seen in Figure 386.

After further gasification at 873 K, giving a weight loss of 3.23%, the surface has become more porous. Figure 388 shows the same area as Figure 386. Here, the surface structure is more diffuse; it is difficult to see certain pores and certain optical textures. Position V can just be distinguished. The dark areas in Figure 388 consist of fizzures, many of which have developed during gasification, thus making the surface very rough (Figures 395 and 396). Many of the pores (~ 1 μm) that are present in Figure 395 were just visible as small pores (~ 0.5 μm) after the first gasification in Figure 393. In Figure 396, the pore which is about 1 μm wide, across the bottom of the micrograph has become larger on gasification. It was only 100 nm in Figure 394 after the first gasification.

After further gasification now at 973 K, to a further weight loss of 1.34% the surface was too rough for optical micrographs to be taken. The large pore (6 μm wide) at the top of Figure 394, has lost its identity in Figure 398. The surface has become so rough that it has incorporated this pore. The orientation of the graphite layers is seen in Figure 397,

where the etching of the surface runs parallel to the graphitic layers. In the centre of Figure 398, there is a very thin lace-like structure with 400 nm pores held together by thin layers (< 50 nm wide).

After further gasification, now at 1073 K to a further weight loss of 4.89% (Figures 399 and 400) the surface was unrecognisable. The only way that the same area could be found was by locating the marks made using the micromanipulator. These marks were deep so that they would not be lost during the gasification. In Figure 400, sheets of graphitic layers can be seen with fizzures in between the layers. The fizzures vary in size from 200 nm to 10 μm. The edges of the layers are rough where they have been exposed.

Figures 401 to 415 show micrographs of AGLMP graphite before and after successive gasifications at 873 K, 973 K and 1073 K, (Table 7) giving weight losses of 0.67%, 4.29%, 1.83% and 5.23%. Again, as with Lima graphite, the blue colour has disappeared, but the yellow remains. Several pores have developed after the first gasification at 873 K to 0.67% weight loss as seen by comparing Figure 405 with Figure 408. The developed pores are about 400 nm wide. Smaller pores that have developed are seen at the top of Figure 409, these are leas than 50 nm wide.

After further gasification at 873 K to 4.29% weight loss, the surface has become very porous as seen in Figure 410 and 411. The small pores that had developed in Figures 408 and 409 have enlarged to about 1 μm. The central pore W had lost a large piece of graphite from the centre.

In Figure 411 pores have developed which are about 2 μm wide. The internal pore wall seen in the centre of Figure 411 is also very rough, with pores (~ 1 μm) in between the flakes of graphite. In the optical micrograph (Figure 403) the interference colours have almost disappeared completely. A few purple areas remain which are more resistant to oxidation than the prismatic edges depicted by the blue and yellow colours.

After further gasification, now at 973 K with an additional weight loss of 1.83% (total 6.69%) an optical micrograph could not be taken because the surface was too rough. The porosity of the surface has increased as seen in Figure 412, but it is interesting to note that the small pores (< 2 μm) have increased by a factor of up to 5, whereas the large pores i.e. at the top of Figure 412, have only increased by a very small amount (~ 2 μm) around the edges of the pore. i.e. a factor of 1.1. A few pores (~ 2 μm) have developed in the pore wall.

After the final gasification at 1073 K (additional weight loss 5.23%) the surface has completely changed, even the large pores have changed their topography. The area was difficult to find but was located by having marked the graphite, and by locating the Gilso-carbon pore structures, two of which are seen in Figure 404 before gasification. The located area is seen in Figures 414 and 415. Figure 415 is uncomparable with Figure 405. The surface is very rough and flakey, which makes focussing difficult. In the Gilso-carbon areas, the initial pores (~ 5 μm) have become larger by a factor of 4, and many smaller pores (~ 1 μm) have developed parallel to the original pores.

Figures 415.1 to 415.20 are scanning electron micrographs of Lima graphite (LG19) and AGLMP graphite (AG11) before and after gasification in carbon dioxide with a flow rate of 440 $mm^3 s^{-1}$ at 913 K for sixteen hours, giving weight losses of 1.48% and 0.42% respectively. Pores of different sizes are studied at high magnification (Figures 415.4 and 415.5 and Figures 415.14 and 415.15) to distinguish any differences during gasification.

During gasification of Lima graphite (Figures 415.1 to 415.10) many small pores (0.5 μm to 1 μm) develop throughout the whole surface as seen in Figures 415.7 and 415.8. In Figure 415.8 the area (top left of micrograph) has gasified less than the other areas and there is a boundary, Position X, separating these areas. These two distinct areas have different optical textures. The area on the right of the boundary has a fine mozaic texture, whereas the area on the left has a large isochromatic optical texture. The boundary between these two areas is just visible before gasification as an indistinct line, Position X (Figures 415.2 and 415.3). During gasification, the boundary develops many small pores (~ 2 μm diameter) some of which are near-circular, others are long (~ 5 μm) thin cracks (~ 1 μm wide).

Figures 415.4 and 415.5 are micrographs of two different sizes of pores (4 μm wide and 45 μm wide) taken before and after gasification. Figures 415.9 and 415.10 are micrographs of the same pores after gasification. Figure 415.9 is not well focussed because the surface was very rough. Before gasification, the pore in Figure 415.4 measured 4.0 μm and 1.5 μm wide, at two particular positions, after gasification the pore was 4.75 μm and 2.75 μm wide at the same positions. Before gasification the pore in Figure 415.5 was 13 μm and 47 μm wide at two particular positions and after gasification it was 15 μm and 48 μm wide at the same positions. This showed that after gasification the two pores lost the same amount of graphite from their walls (between 0.75 μm and 2 μm). Measurements made on the smaller pores were more accurate because the resolution was higher.

Figures 415.11 to 415.20 are scanning electron micrographs of AGLMP graphite (AG11) before and after gasification having a weight loss of 0.42%. The extent of gasification is not as high in this graphite as seen by comparing Figures 415.8 and 415.18, but the surface is still pitted with many small pores (0.5 μm to 1.0 μm).

Figures 415.14 and 415.15 show two different sized pores The pore in Figure 415.14 is a long, thin fizzure which has become very blurred in Figure 415.19 and is not measurable. However, the pore at the bottom of Figure 415.13 can be measured and is 5.5 μm and 9 μm wide before gasification and 6 μm and 10 μm wide after gasification. The large pore in Figure 415.15 was 26 μm and 11 μm wide before gasification and 26 μm and 11 μm after gasification (weight loss 0.42%). These measurements show that after gasification the smaller pore (~ 5 μm) lost about 1 μm of graphite during gasification whereas the larger pore (~ 25 μm) did not increase its diameter at all during gasification.

Figures 415.21 to 415.30 are scanning electron micrographs of AGLMP graphite (AG12) before and after gasification in carbon dioxide with a flow rate of 530 $mm^3 s^{-1}$ at 1073 K for sixteen hours, giving a weight loss of 1.13%. The surface has become very rough during gasification as seen in Figure 415.28. Gasification has taken place to a greater extent in this sample, due to a higher temperature and a faster flow rate of carbon dioxide. This causes carbon monoxide, which acts as an inhibitor, to be drawn away from the surface of the sample, hence the surface is less inhibited. The very rough surface due to gasification has made pore size measurements very difficult, as seen in Figures 415.29 and 415.30.

Position Y has been inserted for identification. Both pores studied at higher magnifications have increased their diameter, the pore in Figure 415.30 was 4.5 μm wide before gasification and 8 μm wide after gasification. In Figure 415.27, two large circular pores (~ 10 μm wide) have developed. There was no trace of these pores before gasification (Figure 415.22). They may have been just under the surface and been enlarged during gasification.

Figures 415.31 to 415.51 are optical and scanning electron micrographs of Lima graphite (LG20) and AGLMP graphite (AG13) before and after gasification in carbon dioxide, flow rate of 700 $mm^3 s^{-1}$, at 1173 K for sixteen hours, giving weight losses of 6.78% and 3.68%. The optical micrograph (Figure 415.31) shows a mesophase-type sphere (170 μm wide) in the graphite surface with bands of yellow, blue and purple around the edges, and a mozaic structure in the centre.

The scanning electron micrographs of Lima graphite (LG20) (Figures 415.32 to 415.40) show extensive gasification over the entire surface (weight loss 6.78%). Position Z on Figures 415.33 and 415.37 identifies the same area before and after gasification. At higher magnifications, Figure 415.39 it is difficult to identify individual pores. The pore at the

bottom of Figure 415.33 was 20 μm wide before gasification and 26 μm wide after gasification. Figures 415.31 and 415.40 are corresponding micrographs. Gasification has created a fizzure at the edge of the sphere of anisotropic graphite with thin fizzures (~ 2 μm wide) radiating from the centre to the outside of the sphere. The areas with fizzures correspond to the blue and yellow areas inside the sphere in Figure 415.31. The purple area at Position $\underline{A}_1$ does not contain fizzures, but is a smooth surface as in Figure 415.40. This could be a basal plane surface which oxidises to a lesser extent than the prismatic edges, where the fizzures develop.

Figures 415.41 to 415.51 are scanning electron micrographs of AGLMP graphite (AG13) before and after extensive gasification having a weight loss of 3.68%. The pores are easily identifiable (Figure 415.46) but increases in the diameter of the small pores (~ 2 μm) (Figure 415.44) are difficult to measure. Before gasification, the pore in Figure 415.44 was 2.5 μm wide (centre) and 1 μm wide (top). After gasification, the pore was still 2.5 μm wide (centre), but 2 μm to 2.5 μm wide (top), i.e. the shape of the pore has changed on gasification. The large pore in Figure 415.45 remained unchanged in shape after gasification, but increased in size (width: 12.5 μm to 13.5 μm).

6.6. Conclusions.

Different graphites gasify at different rates. Lima, a petroleum-coke graphite, is the most reactive to gasification, as seen in Table 6. Different oxidants attack the same graphites at different rates. Atomic oxygen is the fastest type of oxidation, having an oxidation rate of 12% h^{-1} at 300 K, on Lima graphite. Air is the next most reactive oxidant, having an oxidation rate of 2.5% h^{-1} at 873 K. Carbon dioxide is a very slow oxidant having an oxidation rate of 0.007% h^{-1} at 873 K, on Lima graphite.

In the gasifications carried out where the flow-rates were measured, the rates of gasification of the graphite surface were dependent on the rate of flow of the carbon dioxide. Lima graphites (LG13 and LG15) were gasified at 1173 K, at flow rates of 500 $mm^3 s^{-1}$ and 700 $mm^3 s^{-1}$ to give weight losses of 2.63% and 3.65%. The surface topography also changed to a greater extent when the flow rate was high (700 $mm^3 s^{-1}$). e.g. Lima graphite (LG18). Perhaps accumulated carbon monoxide is inhibiting the gasification.

The topographical changes induced by gasification are related to the optical textures. Surface changes can be predicted from optical textures, e.g. in blue and yellow flow areas gasification fizzures develop running parallel to the flow lines. In mozaic areas, many small near-circular pores develop.

Gasification causes a loss and/or change in the interference colours, as seen in Figures 181 and 212. This loss of colour could be due to a slight roughening of the surface causing a change in the reflectivity of the surface. It is the blue and yellow colours which change, the purple areas remain the same. This could be due to preferential gasification taking place at the prismatic edges. The loss of colour is clearly represented in the samples that have been gasified with atomic hydrogen (Figures 258 and 259).

When studying the gasification behaviour of different sized pores, it is found that the same amount of graphite is being lost from the pore walls whether the pore is 1 μm or 20 μm wide. Small pores (~ 100 nm) which develop during gasification are not seen in the scanning electron micrographs taken before gasification. It is unlikely that the pores do not exist initially, but that they are beyond the resolution of the micrographs taken.

The overall conclusions from this work are:

(1) topographical changes and porosity development can be predicted by studying the optical texture prior to gasification,

(2) similar forms of anisotropy behave similarly when gasified with different gases,

(3) similar forms of anisotropy in different graphites behave similarly when given identical gasification treatments.

CHAPTER 7

NON-DESTRUCTIVE TESTING OF GRAPHITES BY ULTRASONIC PULSE VELOCITY MEASUREMENTS.

7.1. Introduction.

The velocity of ultrasonic pulses travelling in a solid material depends on the density and elastic properties of that material. The measurement of ultrasonic pulse velocities in some materials can be used to indicate their quality, i.e. any flaws or cracks in concrete, as well as to determine elastic properties.

The velocity of a pulse of longitudinal ultrasonic vibrations travelling in an elastic solid is given by:

$$V = \sqrt{\frac{E}{P}\ \frac{(1-\nu)}{(1+\nu)\ (1-2\nu)}}$$

Where E is the dynamic elastic modulus

P is the density

and ν is Poisson's Ratio

This equation can apply to the transmission of longitudinal pulses through a solid of any shape or size, provided that the dimension measured perpendicular to the path of the travelling pulse is not

less than the wavelength of the pulse vibrations. The pulse velocity is independent of the frequency of the pulse; hence the pulse velocity will depend on the properties of the material, and by measuring this velocity, an assessment can be made of the condition of the material.

The pulse velocity is decreased when pores are present in a material. Therefore, the velocity of pulses travelling through a very porous material will be less than the velocity travelling through a less porous material. The time taken for the pulse to travel a certain path length is a function of the size of the pores in the material.

The application of sonic and ultrasonic techniques to the testing and examination of carbon has been carried out and discussed by Davidson[154]. He detected internal stress cracks, and measured non-uniformities which influence the physical and mechanical characteristics, i.e. variations in hardness, density and porosity. He also measured elastic constants using sonic resonance and ultrasonic pulse velocity measurements. The tests were all non-destructive and could be used to replace or supplement standard destructive methods.

Ultrasonic testing can be used to detect changes in the porosity and strength during oxidation. Several investigators have carried out work on the effect of oxidation on the strength[155,156] and mechanical properties of graphite[157]. Board and Squires[158]

investigated the effect of oxidation in carbon dioxide on the tensile, flexural and compressive strength of nuclear graphite. They found that the fall-off in strength with burn-off closely followed the fall-off in flexural moduli, indicating that the graphite fails at constant strain.

Morgan and Becker[159] carried out ultrasonic testing on a particular type of manufactured graphite before and after oxidation in carbon dioxide. They developed relationships between the changes in ultrasonic velocity and the change in strength. These relationships could be used to determine accurately and non-destructively the compressive strength of the graphite.

In this study, ultrasonic pulse velocity measurements were made on graphites before and after gasification to find out if the method gave useful information on porosity changes during gasification.

7.2. Samples and Sample Preparation.

The samples that were tested were Lima graphite, Morgans EYC 9106 graphite and AGLMP graphite, before and after gasification in carbon dioxide. The samples were cut into 1 cm cubes with parallel sides. Each sample was ground with two grades of emery paper to give a smooth surface; there was no need for the samples to be polished for ultrasonic testing. Each side of the sample was marked so that it could be recognised after gasification.

7.3. Experimental Methods.

The instrument used for ultrasonic pulse velocity measurements is a Pundit (Portable Ultrasonic Non-destructive Digital Indicating Tester). It generates ultrasonic pulses and measures the time taken for them to pass from one transducer to the other through the graphite which is interposed between them. The construction and specifications of the Pundit are described in the Pundit Manual[160]. The transducers used for testing the graphite, have a frequency of 500 kHz, which corresponds to a wavelength of 8 mm, i.e. the dimensions of the graphite must be greater than 8 mm in a direction perpendicular to the path travelled by the pulse.

Before using the instrument on a sample, the zero on the instrument is checked by using a reference bar which has the pulse time engraved on it. The transducers are coated in grease, e.g. water pump grease, to ensure a close contact with the sample. They are then placed on opposite sides of the sample, one acting as a transmitter of the pulse and one as a receiver, so that the pulse passes through the material. The instrument will give a direct read-out in microseconds of the time taken for the pulse to travel across the sample. The path length is measured at the test points.

The pulse velocity(V) is given by

$$V = \frac{\text{Path length}}{\text{Transit time}}.$$

If the two transducer leads come into contact with each other while transit time measurements are being made, it is possible for the receiver lead to pick up unwanted signals from the transmitter lead. This must therefore, be avoided.

Pulse velocities were measured in the virgin graphites, which were then weighed, and gasified in carbon dioxide at temperatures ranging from 873 K to 1243 K. Some graphites were gasified several times and velocity measurements made after each gasification. Weight losses were determined and correlated with velocity changes. On each block of graphite, the velocity was measured in three directions to determine the velocities in the longitudinal and transverse directions.

7.4.Results.

Table 10 gives a list of the gasified graphites studied in Chapter 6 corresponding to the graphites tested using the Pundit. The corresponding Figure numbers for the micrographs taken of graphites gasified to the same temperatures as the graphites studied with the Pundit are also given. The graphites were placed together in the gasification furnace, but the graphites for ultrasonic testing had to be larger than the maximum

size which is suitable for the scanning electron microscope. Hence, the same graphite sample could not be used for both tests.

Tables 11 to 13 give the pulse velocities of the three types of graphites tested, and the change in velocity after gasification. Graphs were drawn of the change in velocity per unit percentage weight loss against gasification temperatures. These are given in Figures 416 to 418 for the three types of graphite tested. Figure 419 is a model which was drawn to represent the velocity of the pulse in the three directions.

7.5. Discussion of Results.

Each graphite had two distinct velocities. This is due to bulk anisotropy in each graphite, the properties being quite different in the longitudinal and transverse directions.

For each graphite the velocity was measured in three directions. The velocity in two directions were very similar whereas the velocity in the third direction was either lower or higher than the other two directions. The two similar velocities suggest that the crystallites are aligned such that the pulse is travelling predominantly along the graphite planes rather than across them. This effect results from the extrusion process during manufacture. Porosity also influences the velocity of the pulse through the graphite sample. The time taken for the pulse to travel through a graphite sample is controlled by the size of pores in the graphite.

The orientation of the pores is also important as this changes the time taken for the pulse to pass through the graphite in different directions.

Figure 416, which represents the change in velocity through Lima graphite gasified in carbon dioxide, shows plots of the change in velocity per unit weight loss against gasification temperatures in the three different directions. The curve representing the directions across the layer planes, Direction D_1, shows a continuing decrease in the change in velocity per unit weight loss as the temperature increases, whereas the other two curves, which represent the directions parallel to the layer planes, D_2 and D_3, show an initial increase in the velocity from a temperature of 873 K to 973 K and a decrease from 973 K to 1073 K, followed by an increase from 1073 K up to the maximum temperature reached, 1273 K.

Figure 417, which represents the change in velocity through Morgans EYC 9106 unipore graphite gasified in carbon dioxide, shows that the plots of the change in velocity per unit weight loss against gasification temperature follow a similar trend in all three directions. There is an increase in the velocity from 873 K to 1073 K followed by another increase to 1273 K. In Morgans EYC 9106 graphite the pores do not occur in any particular orientation. Hence, the changes in velocity in the three directions are similar.

In AGLMP graphite, represented in Figure 418, the changes in velocity in the three directions again follow similar trends, indicating that the pores are arranged equally in the three directions. This may be true for the Gilso-carbon pore area which may be a spherical structure. In the plots of change in velocity per unit weight loss against gasification temperature (Figure 418) there is a small increase in velocity up to 1073 K, then a sharp increase in velocity up to 1100 K, followed by a decrease to 1200 K.

Figures 416 to 418 show that there are both positive and negative variations in the change in velocity per unit weight loss measured through the graphites gasified at different temperatures to different weight losses. This indicates that the velocity through the graphite may either decrease or increase following gasification. It is to be expected that the velocity would always decrease as porosity was developed during gasification. If gasification occurred entirely under conditions of chemical control of reaction rate then change in velocity per unit weight loss should be independent of gasification temperature.

However, the increase in velocity associated with gasification at higher temperatures is rather difficult to explain. Possible explanations are listed below together with critical comments:

(1) Carbon monoxide could be trapped in the pores, such that this gas is replacing <u>air</u> of the original, non-gasified graphites.

Different gases have different values of ultrasonic velocity. However, this change of gas is unlikely to have any measurable effect with these graphites, as the velocity of sound through carbon monoxide is 338 $m\,s^{-1}$ whereas the velocity of sound through air is 331 $m\,s^{-1}$ *i.e.* a small difference in the 2000 $m\,s^{-1}$ of graphite.

(2) Small pores (~500 nm) which are initially present may be closed up. This can occur by slip-movement of layer planes. It could be verified experimentally using the ASID-4D scanning attachment on the JEM 100C. Initially, as distinct from surface topography, traces of oxidation may remove 'pinning' structures so allowing some movement of layers within and so closing some of the pores.

(3) Where surface oxygen complexes are formed, the possibility exists of strong ,hydrogen-bonding via chemi-sorbed water molecules on the surface. At room temperature after gasification, water from the atmosphere may condense in the open pores. The velocity of sound through water is greater than through air (1461 $m\,s^{-1}$ compared with 331 $m\,s^{-1}$).

Figure 419 is a simple diagram to illustrate the bulk anisotropy of extruded graphite and explain the equal values of ultrasonic velocities in directions D_2 and D_3 (along the layers) and the different value in direction D_1 (across the layers).

It is not yet possible to elaborate upon the model to show the variations between the graphites, and to show how the ultrasonic velocities change the way they do (both increasing and decreasing) following gasification at different temperatures.

7.6. Conclusions.

The use of ultrasonic pulse velocity measurements was explored as a tentative method to study changes in the internal porosity of graphites during gasification. Changes in pulse velocity could be measured after gasification. Velocity decreases are probably due to increased porosity i.e. decrease in bulk density, whereas velocity increases after gasification are more difficult to explain but may be due to annealing of small fizzures (<500 nm). The PUNDIT is an additional complementary instrument for studying porosity changes but, in order to draw more conclusions from the method, the observations made would need to be examined further by some or all of the following methods:-

a) testing graphites gasified in different gases,

b) degasifying the graphites before testing with the Pundit,

c) carrying out density and pore size distribution measurements before and after gasification,

d) using high resolution scanning electron microscopy to establish whether small pores are being created, enlarged or lost.

CHAPTER 8

ANALYSIS OF POROSITY CHANGES IN RADIOLYTICALLY OXIDISED GRAPHITES

8.1. Introduction.

In a graphite-moderated nuclear reactor, which is cooled by carbon dioxide, the graphite undergoes radiolytic oxidation by oxidising species which are created by irradiation of the carbon dioxide, (Section 3.5.). The study described in this Chapter is a characterization of dimensional changes in pore structures of radiolytically oxidised graphites. This study is made using optical and scanning electron microscopy and quantitative image analysis, with the Quantimet 720.

8.2. Samples and Sample Preparation.

8.2.1. Microscopy and Quantimet Analyses of Radiolytically Oxidised Graphites and their Controls.

Five radiolytically oxidised graphites were studied; details are given in Table 14. Table 15 gives pre- and post-irradiation properties of graphite H24, which had been irradiated in carbon dioxide containing 0.051% carbon monoxide. Properties for other

graphites are not available. Each oxidised graphite had a corresponding non-oxidised control cut from the same block of graphite. The graphites were oxidised, in the DIDO reactor at Harwell, in carbon dioxide with a small amount of carbon monoxide at about 620 K for one to two cycles, each cycle being thirty days. The graphite samples had been out the reactor for several years to 'cool' to a low level of radioactivity.

The samples were cylindrical in shape, 8 mm diameter by 10 mm length. Sections were cut off the length, and polished for optical and scanning electron microscopy. Unpolished samples were also studied in the scanning electron microscope to examine the topography of the surface as it was when it came out of the reactor. For the image analysis, a small block of each graphite was impregnated with gold^{141} to fill the open pores and hence to distinguish between open and closed porosity. The samples were impregnated at a pressure of 14.8 MPa. The minimum pore entrance diameter to be impregnated at this pressure is 300 nm. It can be calculated from the equation:

$$P = \frac{2\ T\ \cos\Theta}{D}$$

where P is the pressure applied,

T is the surface tension of gold,

θ is the contact angle

and D is the diameter of the pore.

radius

After impregnation, a maximum of surface area of graphite was exposed by cutting it into very thin slices. These were mounted in an epoxy resin and the surface roughly polished with four grades of emery paper and finely polished with three grades of alumina powder using a Pellon pad rather than Selvyt cloth to minimise relief. The surface had to be completely scratch-free otherwise each scratch would be counted as a pore on the image analyser. The gold impregnated graphites were more difficult to polish because of differences in hardness between gold and graphite. Finally the resin blocks were ultrasonically cleaned. Unimpregnated graphite samples were also prepared for the Quantimet by cutting very thin slices, mounting them in an epoxy resin and polishing as for optical microscopy.

8.2.2. Microscopy of Radiolytically Oxidised Lima Graphites.

Three samples of Lima graphite, radiolytically oxidised to different extents, were studied by optical microscopy and scanning electron microscopy.

These had been oxidised in the BFB reactor to weight losses of 1.26%, 9.48% and 22.6% (Table 16). They were exposed to 2% carbon monoxide, 200 ppm methane and 400 ppm hydrogen and water. Each sample was cut from a cylindrical rod with a

centre core, and hence had an outside surface and an inside surface (see Diagram 8.1. below).

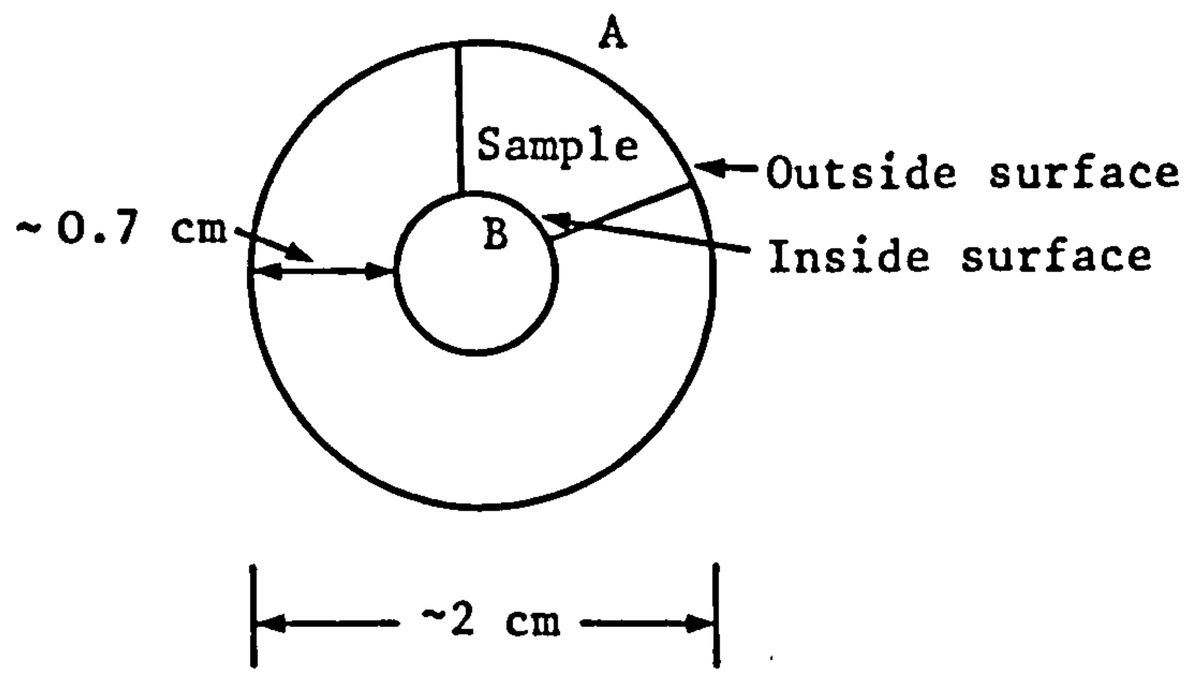

Diagram 8.1. Diagram of shape of radiolytically oxidised Lima graphite as cut from cylinder.

The coolant gas flows perpendicular (upwards) to the plane of the paper i.e. up through the centre of cylinder of the graphite. Thermocouples are present in this central cavity and may cause turbulance of gas over the surface. This turbulance, in turn, may cause unevenness of density of deposit (from the methane) on the surface. For this reason pieces of the specimen were taken from both the outside and inside surfaces (at Positions A and B) and studied 'as received' by scanning electron microscopy. The top or bottom flat surfaces were prepared and polished as for optical microscopy, as normal procedure.

8.3.Experimental Methods.

8.3.1.Microscopy of Radiolytically Oxidised Graphites and their Controls.

The unpolished pieces of graphite were mounted on stubs and studied by scanning electron microscopy. Each radiolytically oxidised sample was compared with its non-oxidised control. Micrographs of similar areas of each sample were taken for comparison. The same areas of polished surfaces were also studied by optical microscopy and scanning electron microscopy. This enables the optical textures to be compared and related to the surface topography. Photo-montages of an area of each graphite were taken at a magnification of 100 X in the scanning electron microscope. This enabled a comparison of the general surface of the graphites to be made.

8.3.2.Quantimet Analyses of Radiolytically Oxidised Graphites.

The radiolytically oxidised graphites, in resin blocks, were studied by an optical microscope attached to the Quantimet 720 (see Section 5.3.9). Three thermally oxidised AGLMP graphite samples (3.1%, 5.4% and 10.5% weightlosses) were also examined. Two of these (5.4% and 10.5% weight losses) are studied in Section 5.3.6. Measurements of percentage porosity, mean intercepts on pores and pore walls (Diagram 8.2(a) below) and perimeters were made initially, but with further experience to remove relief, feature data parameters could be obtained including

number of features (pores), mean area per pore and Feret's diameters (Diagram 8.2(b) below) in four directions at 45° to each other, i.e. longest diameter in four directions.

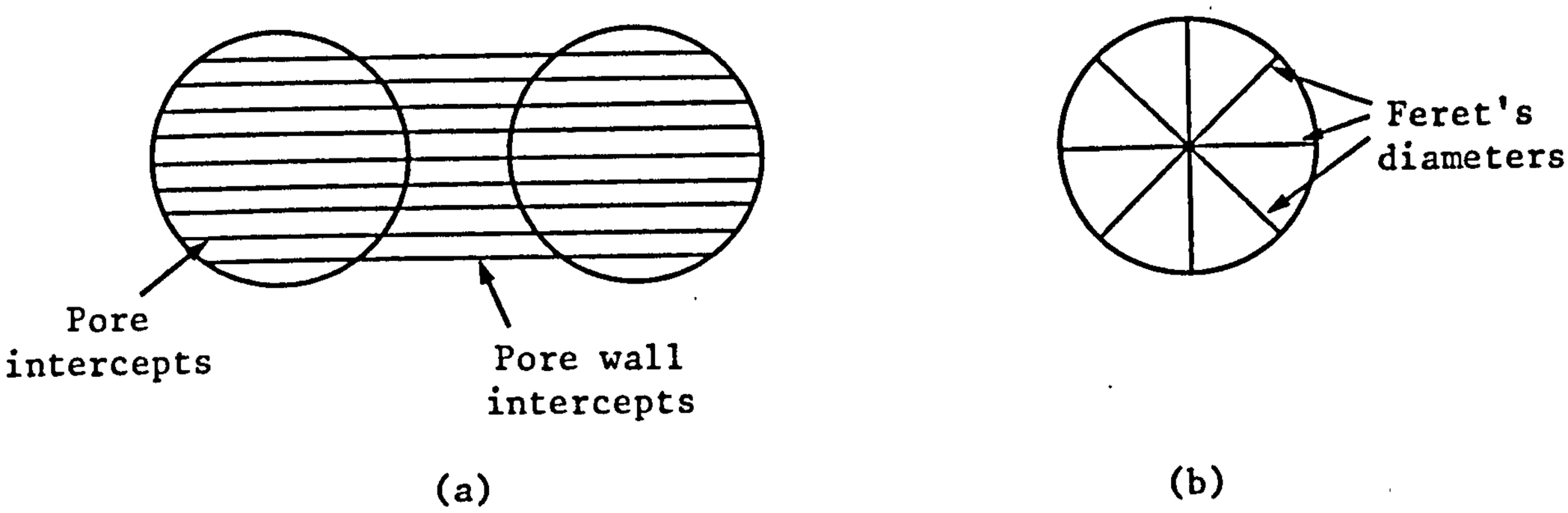

Diagram 8.2. Illustration of a) intercepts and b) Feret's diameters on circular pores as measured on the Quantimet 720.

8.3.3. Microscopy and EDAX Studies of Radiolytically Oxidised Lima Graphite.

The three samples of Lima graphite (Table 16) radiolytically oxidised to different extents were studied using optical microscopy and scanning electron microscopy. The pore size distributions obtained from mercury porosimeter measurements for the virgin, 1.26% and 9.48% weight losses are shown in Figures 510 to 512. The distribution for the 22.6% weight loss sample is not available. For EDAX analyses (energy dispersive

analyses of X-rays)[161, 162] the graphites are mounted as for examination by SEM except that coating by carbon replaces gold coating. When the graphite is scanned by the electron beam the X-rays which originate from the elements in the graphite are analyzed according to the energy of the photon of the characteristic X-ray radiation. A spectrum containing lines associated with the X-ray energies of the elements is displayed on a flourescent screen and this spectrum can be photographed and analyzed.

Analyses were made of the outside and inside edges of the three graphites radiolytically oxidised to different extents, with the exception of the sample oxidised to 9.48%. This had been cut at a very sharp angle and did not exhibit an inside edge. Scanning electron micrographs were taken of all these surfaces to compare topography. The polished faces of the graphites (with control) were studied, using comparable areas, by optical and scanning electron microscopy to study optical texture, pore sizes and the topography of the pore walls.

8.4. Results.

8.4.1. Microscopy of Radiolytically Oxidised Graphites and their Controls.

Figures 420 to 509 are optical, scanning electron micrographs and photo-montages of the radiolytically oxidised graphites and their controls (Table 14).

8.4.2.Quantimet Analyses of Radiolytically Oxidised Graphites.

Table 17 gives preliminary results from the Quantimet obtained on the five radiolytically oxidised graphites and their controls together with some measurements made on three thermally oxidised graphite samples (studied by microscopy in Section 5.3.6.). These results are preliminary because they were obtained when the graphite surfaces still had large amounts of relief. Table 18 gives better field data for pores above ~5 μm after the surfaces were repolished to remove this relief. Table 19 gives feature data (measurements on each recognisable pore above ~100 μm) for the graphite samples.

Figures 513 to 521 are examples of the type of data and distributions which can be obtained from the Quantimet 720. These examples are from the second set of data collected on the five radiolytically oxidised graphites and their controls (Tables 18 and 19). All the computer print-out (raw data) from the Quantimet are in Appendix I .

Table 20 gives the results obtained from the five radiolytically oxidised graphites and their controls which were gold impregnated. The porosity column (Table 20) gives a value for the open porosity whereas the porosity column in Table 18 gives a value for the total porosity (open and closed), i.e. closed porosity can be deduced

from the difference between the porosity in Table 18 and the porosity in Table 20 for a particular graphite. The intercepts in Table 20 give a value for the mean intercept across the open pores and across the rest of the graphite sample i.e. the closed porosity plus the graphite between the pores (pore walls). Field data only was carried out on the gold impregnated radiolytically oxidised graphites and their controls. Tables 21 and 22, and 25 to 27 give size distributions of areas of pores present in Q4/1 and H24 radiolytically oxidised to 8.8% weight loss, and AGLMP graphite thermally oxidised to 3,1%, 5.4% and 10.5% weight loss. Tables 23 and 24 give distributions of Feret's diameters present in Q4/1 and H24. Distributions for the other samples studied are only given in Appendix I because these do not show significant changes in their distributions after oxidation.

8.4.3. Microscopy and EDAX Studies on Radiolytically Oxidised Lima Graphite.

Figures 520 to 552 are scanning electron micrographs of the rough 'as received' inside and outside surfaces of the cylindrical cuts of the radiolytically oxidised Lima graphites (Table 16). Figures 553 to 574 show EDAX data for the inside and outside surfaces of the four Lima graphites (virgin, 1.26%, 9.48% and 22.6% weight losses). Table 28 gives the elements found in the graphites to which the energy peaks correspond in the X-ray spectrum. The figures in brackets are secondary peaks.

Figures 575 to 578 are optical micrographs of the polished surfaces of virgin and radiolytically oxidised Lima graphite samples. Figures 579 to 582 are photo-montages of polished surfaces showing the differences in the general pore structure from virgin to radiolytically oxidised graphite (22.6% weight loss). Figure 583 is a photo-montage of Lima graphite thermally oxidised to 9.2% weight loss, to be compared with Figure 581 which is Lima graphite radiolytically oxidised to 9.48% weight loss.

8.5. Discussion of Results.

8.5.1. Microscopy of Radiolytically Oxidised Graphites and their Controls (Table 14).

Figures 420 to 435 are examples of optical and scanning electron micrographs of BAEL pitch coke graphite H24 and its control Q4/1 (Tables 14 and 15). The weight loss sustained during radiolytic oxidation was 8.8%. Micrographs of the surface were taken before any surface preparation was carried out, in order to look at the topography of the external surface. Figures 420 to 427 show micrographs of the 'as received' surfaces. It was noted that the surfaces were generally smoother after oxidation (Figures 424 to 427) as if the roughness had been preferentially oxidised. The surface of the control sample had many pieces of loose graphite on it (Figures 421 to 422). These are not seen after oxidation (Figures 425 and 426).

The machine cutting marks on the surface were also more prominent after oxidation (compare Figure 420 with Figure 424). The control sample was taken from a position next to the radiolytically oxidised sample. Therefore, assuming the two blocks were machined in an identical way, the sresses and strains incurred on the surface during machining may have been sufficient to produce many active sites on the surface causing preferential oxidation.

After polishing the surface, more differences were seen between the graphites. Figures 428 and 429 are optical micrographs taken of the surface. There was no difference in the optical texture of the two graphites, but the macroporosity of H24, the radiolytically oxidised sample, was greater than that of Q4/1, the control sample (compare Figure 428 with Figure 429). The same areas were studied in the scanning electron microscope (the same areas are marked for identification). Again, (Figures 430 to 433) it can be seen that the macroporosity is higher after radiolytic oxidation (Figure 432). The pores seen here are about 15 μm wide. At high magnifications (Figures 431 and 433) the graphites look similar. Inside the pores, there are long thin pores (~500 nm wide) in both graphites. The area around the pore is fairly smooth, although very small pores (~200 nm) can be seen on the surface after oxidation (Figure 433).

The general macropore structure of the control Q4/1 and H24 are shown in Figures 434 and 435. The porosity in pores above 5 μm has increased by 5.6% (see Table 18). This indicates that most of the increase in the porosity during radiolytic oxidation takes place in the macroporosity, above about 5 μm. From the photo-montages it can be seen that many of the 10 μm pores have expanded and joined together to form pores 20 μm to 50 μm wide. In the control sample (Figure 434) there are several areas where no pores are visible. Here, the size of any pores is below the resolution of these micrographs. Possibly, after radiolytic oxidation, any such pores have developed and become visible (Figure 435).

Figures 436 to 451 are optical and scanning electron micrographs of PGA graphite C79 and its control C7/1, (Table 14). The weight loss sustained during radiolytic oxidation was 6.2%. Figures 436 to 443 are micrographs of the surfaces of the 'as-received' samples. On studying the micrographs, it is evident that the surface is smoother after oxidation. This is seen by comparing Figures 436 and 437 with Figures 440 and 441. It appears that the sharp edges of the surface in Figure 436 have been smoothed. It should be possible to determine the height of these edges and the decrease in height following

oxidation by taking stereopairs and making height measurements. The higher magnification micrographs show a pore wall inside a pore. The internal surface is very jagged in both samples. The area in Figure 443 appears to be under a great strain, as if the graphite is being twisted and pulled apart. Long thin pores (~100 nm wide) are present either side of the central area in Figure 443.

Figures 444 and 445 are optical micrographs of the two PGA graphite surfaces (C7/1 and C79). This graphite (PGA) is very heterogeneous, with many changes in the orientation of the graphite layers across the surface. This is shown by the abrupt changes in the interference colours seen in the optical micrographs. Most of the optical textures are flow-type anisotropy. There are very few fine-mozaic areas as were present in the BAEL pitch coke graphites (Figures 428 and 429).

The same areas were studied in the scanning electron microscope (Figures 446 to 449). The same areas are marked for identification. In between the large pores the surface is not very smooth, but is covered with very small pores down to 500 nm. Pores smaller than 500 nm are not resolvable at this magnification (Figures 446 and 448). There are no smooth areas free from porosity in either the control or the radiolytically oxidised sample. In the higher magnification micrographs (Figures 447 and 449) the inside of the

pore is smooth, but no differences can be detected between the two samples.

Figures 450 and 451 are photo-montages taken in the scanning electron microscope. They show a general area of the two samples. The micrographs are difficult to analyse because the porosity is high and very complex. Although the porosity is high, it is possible to see a slight increase in the porosity after radiolytic oxidation (Figure 451). It is difficult to assess the percentage increase in porosity from the micrographs, but from the Quantimet the increase is 3.2% (Table 18).

Figures 452 to 467 are optical and scanning electron micrographs of AGLMP graphite M38 and its control 10F49, (Table 14). The weight loss sustained during radiolytic oxidation was 3.7%. Figures 452 to 461 are scanning electron micrographs of the surface before any preparation has been carried out. The surfaces do not look significantly rougher in Figures 452 to 456 than in Figures 457 to 461 but in the micrographs taken of the radiolytically oxidised sample the machine lines stand out very prominently as seen in sample H24. This suggests that the machining of the graphite blocks influences oxidation on the machined surface. Scanning electron micrographs were taken inside a pore (Figures 455, 456, 460 and 461). The internal surface of the pore wall is very smooth in both samples. In the control sample 10F49 (Figure 456) there is a rough edge around the pore which is shown in the micrograph.

After polishing the surfaces, optical and scanning electron micrographs were taken (Figures 462 to 467). In the optical micrographs, Gilsocarbon areas are seen, which are made up of small mozaics, predominantly blue and yellow, depending on the orientation of the graphitic layers. The same areas were studied in the scanning electron microscope. There is no significant difference in the polished surfaces of the graphite taken at a magnification of 500 X (Figures 464 and 466). At a higher magnification (Figures 465 and 467) the pore wall is perhaps smoother in the control sample than in the radiolytically oxidised sample.

Figures 468 to 493 are optical, scanning electron and high resolution micrographs taken of AGLMP graphite M28 and its control 584/195 (Table 14). The weight loss sustained during radiolytic oxidation was 3.5%. Figures 468 to 477 are micrographs of the unpolished samples. In Figures 468 and 473 there is no difference in the surface roughness or the grooves made during machining. At high magnifications (Figures 470 and 475) the surface looks slightly smoother after radiolytic oxidation but it is difficult to assess the degree of smoothness by looking at several micrographs. Micrographs taken of the internal pore walls are shown in Figures 471, 472, 476 and 477. The internal surfaces of both samples are very smooth with a few very narrow pores (~200 nm wide) in the pore walls of the control sample and a few larger pores (500 nm wide) in the pore wall of the radiolytically oxidised sample.

After polishing the surface, the optical micrographs (Figures 478 and 479) both show many small pores (2 μm to 4 μm diameter) all over the surface, integrated in fine mozaic areas. The Gilso-carbon boundary can be seen in Figure 479 as an area of slightly larger mozaics. The pores associated with this larger mozaic area are also larger (~5 μm). There is no obvious difference between the two samples. The same area has been studied using the scanning electron microscope (Figures 480 to 483). The surfaces consist of many pores as seen in the optical microscope. At high magnifications (Figures 481 and 483) it is seen that the pores have rough edges in both samples. The edges of the pore walls are slightly rougher in the control sample than in the oxidised sample.

Figures 484 to 491 are high resolution scanning electron micrographs of AGLMP graphite M28, taken using a JEOL 100C - AS1D-4D electron microscope. The sample was not polished prior to examination. Figures 484 to 486 show an area of graphite where the structure appears to twist and turn under strain (Figure 485). In these micrographs pores down to 10 nm in size can be resolved. The strain area in Figure 485 consists of pores that are 20nm to 50nm wide. The strain area appears to form a flowing type of structure through the graphite.

Figures 487 to 491 show a second area of AGLMP graphite M28 which has a large pore about 25 μm wide with a smooth inner surface.

Figure 489 shows the area in the centre of Figure 488. In this area there are some fizzures about 4 μm deep. The walls of these fizzures are quite rough with 100 nm to 200 nm pores in the pore walls. Figure 490 shows the area in the centre of Figure 489. Here many pores (40 nm) are seen which were unresolvable at lower magnifications. The piece of graphite in the centre of Figure 490 appears to be almost loose with a large amount of porosity associated with it. Figure 491 is a porous area, the pores range from 200 nm down to 5 nm. There are many rounded structures which have pores associated with them.

Figures 492 and 493 are photo-montages of AGLMP graphite 584/195 and M28. The area shown is fairly small but it gives a general view of the macroporosity in the two samples. The change in the porosity is small and is difficult to ascertain from the photo-montages shown here, but analyses on the Quantimet confirm a slight increase in the porosity after oxidation (Table 18).

Figures 494 to 509 are scanning electron micrographs of BAEL pitch coke graphite H30 and its control Q6/1 (Table 14). The weight loss sustained during radiolytic oxidation was 0.6%. Figures 494 to 503 are micrographs taken before the surfaces were polished. The two surfaces have the same degree of roughness (Figures 494 and 499). The machining marks are again more prominent in the sample after radiolytic oxidation. In both samples, the surface is very rough

but the pore walls are smooth, with small fizzures ranging from 50 nm to 500 nm wide (Figures 496 and 503). The 50 nm fizzures in Figure 503 appear to have a fold associated with them, where the graphite has buckled. This could be an oxidation effect, or a straining effect during machining.

The scanning electron micrographs taken of the polished surfaces are shown in Figures 504 to 509. The edges of the pores in the control sample are much more jagged than the edges of the pore after oxidation. From the low magnification micrographs (Figures 504 and 507) the macropore structure appears slightly larger in the radiolytically oxidised sample.

8.5.2. Quantimet Analyses of Radiolytically Oxidised Graphites (Table 14).

The preliminary Quantimet results, given in Table 17, serve as a guide-line to the changes in porosity because of problems over the control of surface relief. In Table 17, some porosities from U.K.A.E.A. are given for comparison to ensure that the results obtained are in the right order of magnitude. These apply to both the open and closed pores down to a lower pore size than that studied with the Quantimet. The porosity given by the Quantimet is the total porosity i.e. open and closed porosity, down to 5 μm. Each field studied was 2.5 mm x 2.5 mm. The mean intercept gives an indication of the size of the pores and pore walls. The total perimeter is given for the number of fields studied, and the total number of pores measured is given by the count.

After re-polishing, more reliable data on pores in different size ranges were obtained in order to assess which particular size of pore is being affected most during oxidation. Considerable care was taken not to lose any specimen. The graphites that were impregnated with gold, in order to distinguish between open and closed porosity, were more difficult to polish without relief due to the difference in hardness between gold and graphite. Gold was used because small parts of the sample could be used to study the gold pore shapes after oxidising the graphite completely.

The data obtained from the Quantimet enable distributions of size of pores and thicknesses between the pores (porewalls) to be compared before and after radiolytic oxidation. Figures 513 to 516 are originally from the computer attached to the Quantimet. However, their "y-axes" differed for each sample. Hence, these graphs have been re-drawn. Although for these two graphites (Q4/1 and H24) there was a noticeable difference between the control and the oxidised specimen, for many of the other graphites the weight losses were very low and differences were small. These distributions have not been re-drawn but original graphs are given in Appendix I. For many of the specimens, the mean intercept values and their standard deviations (Table 18) give sufficient information to show that the change in pore sizes after oxidation is not significant.

Figures 513 and 514 are distributions of the number of chords in each size range present in 100 mm^2 area of graphite surface (BAEL pitch-coke Q4/1, (control of H24) and H24, 8.8% weight loss). The chords are measured at intervals across the pores and are a function of the pore size, but they are not direct diameters. The distributions show an increase in the lower size range (up to ~150 μm after oxidation) of the number of both pores and pore walls (graphite between the pores) (compare Figures 513 and 514). The number of pore walls above 150 μm decreases but the number of pores has only a slight increase in the number above 200 μm. After oxidation the change in distribution of the pore walls could be due to the larger pore walls i.e. above ~200 μm, being decreased in size after oxidation due to increases in pore sizes. Table 18 (Q4/1, H24) shows a decrease in the mean intercept of the pore walls, from 410 μm to 267 μm after gasification.

Figures 515 and 516 are histograms representing the areas of pores. Each pore area has been measured and the area converted into an equivalent circular pore. These histograms (Figures 515 and 516) give a measure of the changes in the distribution of pore areas after oxidation. Figures 515 and 516 represent BAEL pitch coke graphite Q4/1, (control for H24) and H24, radiolytically oxidised to 8.8% weight loss.

The distributions show an increase of 850 pores per 100 mm^2 in the number of pores with equivalent circular diameters of between 10 μm and 40 μm after radiolytic oxidation. A smaller increase in the number of pores present (~200 pores per 100 mm^2) is seen between 40 μm and 200 μm. Above 200 μm the number of pores remain approximately the same. This result is consistent with increases in the number of pores seen in Figure 514. The number of counts per field and the total counts per 100 mm^2 are given in Table 18 for each graphite. These are seen to be larger for H24 than Q4/1. Tables 21 and 22 give lists of the distributions from which the histograms were drawn.

Tables 23 and 24 are distributions of Feret's diameters of pores measured on Q4/1 BAEL pitch coke graphite and H24, radiolytically oxidised to 8.8% weight loss. The centre column represents the maximum of the four Feret's diameters measured in four directions on each pore. The right-hand column represents the mean of the four Feret's diameters measured on each pore. The mean of these two distributions are given in the feature data in Table 19. The ratio of the maximum Feret's diameter to the mean Feret's diameter for a pore gives an indication of the shape of the pore. This ratio (shape factor) has been tabulated in Table 19. If the pores were circular then this value would be 1.0. Any variation from this number indicates an elongated pore.

The three thermally oxidised samples of AGLMP graphite (last four lines, Table 18) show a steady increase in the number of pores present per field, and the total number of counts per 100 mm^2. Because of this increase, it is necessary to draw histograms representing the areas of pores, with corrected scales (Figures 517 to 519, AGLMP graphite, thermally oxidised to 3.1%, 5.4% and 10.5% weight losses). The distribution for the virgin graphite was not available. Tables 25 to 27 give lists of distributions from which the histograms were drawn.

The distributions show that from 3.1% weight loss to 5.4% weight loss there is an increase of 700 pores per 100 mm^2 with equivalent circular diameters between 10 μm and 50 μm and between 50 μm and 300 μm there is a slight decrease of about 20 pores per 100 mm^2 after oxidation. From 5.4% weight loss to 10.5% weight loss there is an increase of about 850 pores per 100 mm^2 with equivalent circular diameters between 10 μm and 70 μm, but there is approximately no change in the number of pores with diameters above 70 μm.

These results show that when studying changes in porosity caused by oxidation, the major effect is to create pores in the size range of graphite 10 μm to 70 μm.

The total number of counts per 100 mm^2 (Table 18) show that from 3.1% weight loss to 5.4% weight loss, the increase in the number of pores is 674, and from 5.4% to 10.5% weight loss, the increase in the number of pores is 900. These results are consistent with the distributions in Figures 517 to 519.

The feature data (Table 18) for individual pores, give mean perimeters per pore, mean areas per pore, mean Feret's diameters per pore, and shape factors. The shape factors are derived from two measurements, i.e. the ratio of maximum to mean Feret's diameters and the area divided by perimeter^2. For a circular pore, these shape factors should be 1.0 and 0.0796 respectively. Deviations from these numbers indicate elongated or elliptical shaped pores. A pore shape which approximately fits the second set of shape factors given in Table 19 is shown in Diagram 8.3 (below). This gives a shape factor, area divided by perimeter^2, of ~0.03 but gives a shape factor, maximum Feret's diameter divided by mean Feret's diameter, of ~1.4 which is slightly higher than those given in Table 19. These shape factors are mean values and Diagram 8.3 gives a shape which may be present in many of the graphite samples. It shows also Feret's diameters measured in four directions.

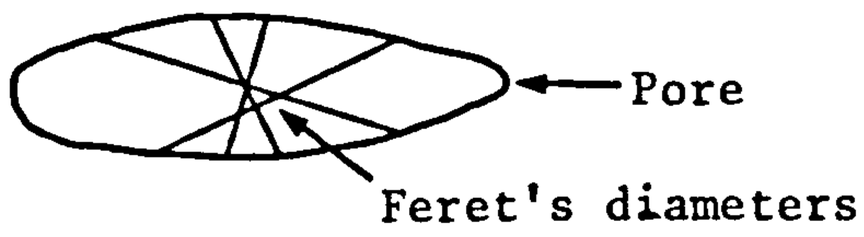

Diagram 8.3 Pore shape giving shape factors similar to those in Table 19.

Table 20 gives field data on the gold impregnated samples. The porosity measurements are those for the open pores now filled with gold. In order to obtain a value for the closed porosity, these values are taken from the porosity values in Table 18. The mean pore intercepts refer only to open pores.

Distributions and Tables for the other samples studied are given in Appendix I. Many of the distributions were so similar for the control and the radiolytically oxidised sample, that it was felt unnecessary to correct all the scales and redraw the graphs for all the samples studied.

8.5.3. Microscopy and EDAX Studies on Radiolytically Oxidised Lima Graphite Samples. (Table 16).

Figures 520 to 523 are scanning electron micrographs of a rough surface of virgin Lima graphite. This was studied as a control for the radiolytically oxidised graphites. The entire area has a very rough appearance with large pores (~30 μm wide) visible in Figure 520.

Figures 524 to 535 are scanning electron micrographs of rough 'as-received' surfaces of Lima graphite radiolytically oxidised to 1.26% weight loss. The inside and outside surfaces are both examined, (see Diagram 8.1, Section 8.2). Figures 524 to 527 are micrographs of the inside surface. The overall

appearance of the surface is rough but at higher magnifications (Figures 526 and 527) many areas of the surface are quite smooth with pieces of loose graphite scattered over the surface.

Figures 528 to 535 are micrographs of two areas of the outside surface. The first area (Figures 528 to 531) shows a large pore (~ 60 μm wide) with very flat smooth pieces of graphite inside the pore. The surface of the graphite is quite rough but inside the pores the walls are relatively smooth, with some loose graphite present (Figure 531). Figures 532 to 535 show a second area of the outside surface of Lima graphite (Table 16) radiolytically oxidised to 1.26% weight loss. This shows a rough area at low magnification (Figure 532) but at higher magnification (Figure 534) the surface is made up of many smooth hillocks with rough areas between them. Figure 535 shows one of these hillocks. The surface is very smooth with flakes having small pores associated with them of ~200 nm wide. The rough areas between these hillocks have loose particles as if flaked from the graphite surface.

Figures 536 to 539 are scanning electron micrographs of Lima graphite (Table 16) (no inside surface) radiolytically oxidised to 9.48% weight loss. The outside surface is rough but with smaller hillocks than in Figures 532 to 535. The hillocks have smooth surfaces with loose flakes between the hillocks.

Figures 540 to 552 are scanning electron micrographs of the 'as-received' surface of Lima graphite (Table 16) radiolytically oxidised to 22.6% weight loss. Figures 540 to 548 are micrographs of the inside surface. These micrographs show a deposit which has accumulated on the surface. Between the areas of deposit is a very rough, speckled surface seen in Figure 542. This deposit may be a protective layer which builds up when methane is used as an inhibitor. The C_4 molecules present in the coolant gas could crack under the conditions of temperature, pressure and radiation to produce this deposit. The deposit is shapeless in appearance. The surface of the deposit looks smooth at low magnification (Figure 541) but at higher magnification the surface is covered with small circular pieces of material about 200 nm to 300 nm in diameter. This deposit only appears on the inside surface of the graphite specimen and not on the outside surface (see Figures 549 to 552). It is possible that thermocouples and other controls present in the annulus could introduce a micro-diffusion environment, which facilitates the accumulation of the deposit. (For EDAX analysis, see below).

Figures 545 to 548 show a second area of the inside surface of Lima graphite radiolytically oxidised to 22.6% weight loss (Table 16). The deposit in certain areas is present at the pore entrances i.e. Position 9 in Figure 545. Figures 546 to 548 show

areas between the deposits. These areas have very 'fluffy-like' surfaces with many loose circular areas of material ranging from 200 nm to 5 μm in diameter.

Figures 549 to 552 are micrographs of the outside surface of the above Lima graphite. This surface is quite different from the inside surface with no deposits and no flakey areas (cf. Figure 547). The surface is generally rough at low magnification but certain areas are smooth at higher magnifications, Figure 552, which shows many small pieces of material on the surface about 100 nm to 200 nm in diameter. The surface in Figure 549 looks as if it has been etched by gases flowing over it giving flow patterns towards the bottom of the micrograph. The topography of Figure 550 also appears to flow from the top of the micrograph to the bottom. This topography could be induced by gasification.

Figures 553 to 574 are EDAX studies of the four Lima graphites (Table 16). Each 'as-received' inside and outside surface has been examined. Figures 553 to 555 are X-ray spectra of virgin Lima graphite. The X-ray spectrum in Figure 553 shows aluminium, silicon, chlorine and iron. Table 28 shows which energy peaks correspond with the elements present in graphite. Aluminium is always detected because of the aluminium stub on which the sample is mounted and because of the use of alumina powder in polishing. Iron is always detected from the

final lens in the electron microscope. Figure 554 shows positions where silicon is present in the area shown in Figure 555. Some areas may be shadowed from the electron beam, i.e. no spectra are possible (cf. Figures 554 and 555) The whole sample has a low concentration of silicon distributed across it (Figure 554).

Figures 556 to 559 show X-ray analyses of the inside surface of Lima graphite radiolytically oxidised to 1.26% weight loss (Table 16). The X-ray spectrum (Figure 556) shows aluminium, nickel, silicon, and low concentrations of sulphur, chlorine, potassium, calcium, and iron. The silicon EDAX analysis (Figure 557) shows perhaps, a higher concentration of silicon than in the virgin sample (cf. Figure 554). The analysis for nickel was carried out and reproduced because nickel was not present in the virgin sample. Figure 558 shows that the concentration is small and uniform over the whole area.

Figures 560 and 562 show X-ray analyses of the outside surface of Lima graphite radiolytically oxidised to 1.26% weight loss (Table 16). The X-ray spectrum (Figure 560) shows aluminium, silicon, (sulphur, chlorine and iron in low concentrations) present on the surface. The silicon analysis

shows similar concentrations on inside and outside surfaces (Figures 557 and 561) with a uniform distribution of silicon. Figures 563 to 566 show X-ray analyses of the outside surface of Lima graphite radiolytically oxidised to 9.48% weight loss (Table 16). The X-ray spectrum (Figure 563) and analyses are very similar to those of the graphite oxidised to 1.26% weight loss.

Figures 567 to 570 show X-ray analyses of the inside surface of Lima graphite radiolytically oxidised to 22.6% weight loss (Table 16). In this sample there is a higher concentration of silicon and nickel present than in the other radiolytically oxidised graphites. There are also aluminium and small concentrations of sulphur, chlorine and iron present.

The X-ray analyses for silicon and nickel in the deposit (Figures 568 to 570) show a lower concentration of these elements present in the deposit than elsewhere (see Figure 570 (the area analysed)). The X-ray analyses of this inside surface (Figure 570) for aluminium, sulphur, chlorine and iron show low concentrations of each element distributed uniformly over the deposit and elsewhere. It would therefore appear that the deposit consists essentially of carbonaceous material and contains no large concentration of elements that could be detected using the EDAX system.

Figures 571 to 574 show X-ray analyses of the outside surface of Lima graphite radiolytically oxidised to 22.6% weight loss (Table 16). These analyses are similar to those reported for the Lima graphite radiolytically oxidised to 1.26% weight loss.

Figures 575 to 578 are optical micrographs of porous areas of the four Lima graphites (Table 16) showing their optical textures. Figure 575 (virgin Lima graphite) shows flow-type anisotropy 50 μm to 100 μm long with pores, e.g. Position 10, alongside the flow areas, with walls consisting predominantly of basal planes. Figure 576 (Lima graphite radiolytically oxidised to 1.26% weight loss) is similar to Figure 575 with flow-type anisotropy, and mozaics (Position 11).

Figure 577 is an optical micrograph of Lima graphite radiolytically oxidised to 9.48% weight loss. This is more porous than shown in Figures 575 and 576, with a similar optical texture. Figure 578 is an optical micrograph of Lima graphite radiolytically oxidised to 22.6% weight loss and shows an evident increase in porosity. Flow-type anisotropy and mozaics are present. Figures 575 to 578 indicate that radiolytic oxidation does not change the optical texture of the graphite, even when the porosity is considerably increased.

Figures 579 to 582 are photo-montages of similar areas of the four graphites (Table 16), each taken at the same magnification. The montages represent an area of about 3.5 mm by 2.0 mm. Figure 579 is a photo-montage of virgin Lima graphite. In this montage there are several areas which are non-porous or contain a few almost unresolvable pores at the magnification shown. In general, the pores are ~30 μm wide with a few larger pores ~50 μm wide. Figure 580 is a photo-montage of Lima graphite radiolytically oxidised to 1.26% weight loss. The whole surface is more porous than the virgin sample. There are less non-porous areas and many more pores between 10 μm and 20 μm than in the virgin sample.

Figure 581 is a photo-montage of Lima graphite radiolytically oxidised to 9.48% weight loss. This photo-montage shows the number of pores above 10 μm to have increased and non-porous areas to be less than 100 μm wide. In the virgin sample (Figure 579) there are several non-porous areas, about 300 μm wide and in the 1.26% weight loss sample (Figure 580) there are areas about 200 μm wide which are non-porous.

Figure 582 is a photo-montage of Lima graphite radiolytically oxidised to 22.6% weight loss. In this montage there are no non-porous areas. The porosity has increased and there are more larger pores present, about 50 μm wide, than seen in the less oxidised or virgin graphites. The number of smaller pores between 10 μm and 20 μm has increased and these cover a large area of the surface. With these radiolytically oxidised samples it was not practical to gold impregnate and use the Quantimet.

Figure 583 is a photo-montage of Lima graphite thermally gasified in carbon dioxide to 9.18% weight loss (Table 7 (LG18)) and can be compared with Figure 581 (radiolytic oxidation). The surfaces are quite different, the radiolytically oxidised sample being covered with small pores between 10 μm and 20 μm, whereas the thermally oxidised sample still has many non-porous areas as seen in the virgin sample. There are many large pores between 50 μm and 150 μm, which are not seen in the radiolytically oxidised sample, even at a higher weight loss (Figure 582). Although only a small area was studied for each sample (about 3.5 mm by 2.0 mm) an area typical of the sample was photographed.

8.6. Conclusions.

Scanning electron microscopy of the radiolytically oxidised graphites shows that the 'as-received' surfaces are similar whether or not methane is present in the carbon dioxide during radiolytic oxidation (i.e. Tables 16 and 14 respectively). Where machining grooves are present before oxidation, they become more prominent after radiolytic oxidation.

Although it is difficult (because of different extents of oxidation) to compare directly the porosity of the graphites radiolytically oxidized with and without the inhibitor methane in the coolant carbon dioxide it would appear that the modes of radiolytic oxidation are comparable. Even though rates of oxidation must have been lower in the presence of methane the mechanisms of increase of pore volume are comparable.

The radiolytically oxidised graphite oxidised in the presence of methane (Table 16) to a weight loss of 22.6% exhibits a carbonaceous deposit on the inside surface. This deposit is without crystalline structure, is irregular in shape and contains a lower concentration of nickel and silicon than is present on the surface surrounding the deposit. Such deposits are not observed in the absence of methane.

Photo-montages (SEM) of the virgin and radiolytically oxidised graphites (Table 16) (in the presence of methane) show the expected increase in porosity with increase in weight loss. The increase is mainly in the pore size range 10 μm to 50 μm. Non-porous areas are present in the virgin graphite but not in the radiolytically oxidised graphites (at low magnification).

A comparison of radiolytic and thermal oxidation of graphite (weight losses of about 9%) shows that small pores between 10 μm and 20 μm diameter develop uniformly over the surface during radiolytic oxidation. The average distance between pores is about 75 μm. During thermal oxidation larger pores between 50 μm and 150 μm diameter develop. The distances between the pores is about 200 μm. No porosity or change in the graphite surface could be detected in the areas of surface between the porosity. The origins of porosity in radiolytic oxidation remain obscure.

The Quantimet data show that for the H24, BAEL pitch-coke graphite (radiolytically oxidised to 8.8% weight loss, Table 14), there is an increase in the frequency of all pores in the size range 10 μm to 150 μm when compared with the control. The extent of increase in frequency declines from 10 μm to 150 μm

as shown below. The frequency is expressed as the number of chords measured across the pores.

Size	Increase in Frequency
10 µm	17,000
30 µm	11,000
50 µm	6,000
70 µm	4,500
90 µm	2,500
110 µm	2,000
130 µm	1,000
150 µm	700

The number of chords measured across the pore walls behaves comparably to changes in pore diameter, but the number of chords measured above 200 µm decreases by 30% after oxidation. This decrease is due to existing pores increasing in size; hence, increasing the number of smaller pore walls (10 µm to 50 µm).

For H24, BAEL pitch-coke graphite (radiolytically oxidised to 8.8% weight loss, Table 14) the number of pores with equivalent circle diameters in the range 10 µm to 40 µm increases by 850 pores per 100 mm^2 and in the range 40 µm to 200 µm by 200 pores per 100 mm^2. Shape factors show that the majority of pores are elliptical.

CHAPTER 9

MICROSCOPIC EXAMINATION OF NEUTRON - IRRADIATED GRAPHITE

9.1. Introduction.

Microscopic examinations are made of neutron-irradiated graphites to monitor changes in topography and pore structure of the graphites caused by neutron-irradiation. A pitch-coke based graphite (VQMB) and a Gilso-carbon based graphite (AGLMP) were irradiated in the Dounreay FAST REACTOR (623 K to 823 K) to compare their behaviour under irradiation[163].

The individual crystallites grow parallel to the hexagonal c axis and shrink parallel to the basal planes at practically constant rate and constant volume[164] under irradiation at temperatures around 623 K to 823 K.

Until the present time, Gilso-carbon graphite has been used in the Advanced Gas-cooled Reactors but because of the uncertainty of obtaining quantities of Gilso-coke, alternative graphites for future Reactors are being considered i.e. a pitch-coke graphite.

9.2. Samples and Sample Preparation.

Six samples of two graphites were studied, details of which are given in Table 29. The graphites were VQMB, a pitch-coke graphite and AGLMP, a Gilso-carbon graphite. Two of the samples were controls without irradiation. The samples of graphites were cylindrical in shape, 4 mm diameter by 10 mm length. One thin sliver from each cylinder was cut off and examined by scanning electron microscopy before polishing. This enabled the topography of the 'as received' surface (the end surface, not the cut surface) to be studied. In order to prepare a polished surface of the graphite samples a further sliver of each sample was cut off from the cylinder and the sliver mounted in resin. The surface was initially abraided with emery paper and then finally polished using three grades of alumina powder.

9.3. Experimental Methods.

The unpolished samples were mounted on stubs for scanning electron microscopy. Each irradiated sample was compared with its control. Energy dispersive analysis of X-rays (EDAX) was carried out on each surface in order to find out if any inorganic elements were present in the graphite (see Section 8.3.3.).

The polished samples were studied using both the optical and scanning electron microscope. The same area of the polished surface of graphite was studied by each instrument. This enabled the optical textures (in colour) obtained via the optical microscope to be compared and related to the surface topography of a particular area as photographed by scanning electron microscopy.

9.4.Results.

Figures 584 to 589 are photographs of the X-ray spectra and scanning electron micrographs of the 'as received' surfaces from which the spectra were taken for samples of the non-irradiated (control) and of the irradiated VQMB graphite. Figures 590 to 608 are scanning electron micrographs of the 'as received' surface (before polishing) of samples of the non-irradiated (control) and of the irradiated VQMB graphite. Figures 609 to 614 are photographs of the X-ray spectra and scanning electron micrographs of the 'as received' surfaces (before polishing) from which the spectra were taken for samples of the non-irradiated (control) and of irradiated AGLMP graphite.

Figures 615 to 629 are scanning electron micrographs of the 'as received' surfaces (before polishing) of samples of the non-irradiated (control) and of irradiated AGLMP graphite.

Figures 630 to 671 are optical and scanning electron micrographs of polished surfaces of VQMB graphite and AGLMP graphite, both non-irradiated and irradiated.

Table 28 gives the elements to which the peaks correspond in the X-ray spectra. The figures in brackets are secondary peaks.

9.5. Discussion of Results.

9.5.1. Edax Spectra. VQMB Graphite.

The X-ray spectra in Figures 584, 586 and 588 show that aluminium, silicon and iron are present in both the virgin and the neutron-irradiated samples of VQMB graphite. A small amount of aluminium is generally detected because of the aluminium stub on which the sample is mounted. Iron is always present because it is in the final lens in the electron microscope. Figure 586 which represents LZAA (-1.99% linear growth) has a larger amount of iron present than is expected from the lens. This must be present in the graphite together with the silicon which is present in all the graphite samples.

9.5.2. VQMB Graphite. Non-polished Surfaces.

Figures 590 to 594 are scanning electron micrographs of an 'as received' surface of virgin VQMB pitch-coke graphite. The

graphite has a very smooth, almost polished surface, with scratch marks across it. The large pores on the surface (Figure 590) are about 30 μm to 50 μm wide. The smoother areas in Figure 590 contain much smaller pores, about 2 μm wide.

Figures 595 to 601 are scanning electron micrographs of an 'as received' surface of the pitch-coke graphite (LZAA) after neutron-irradiation (-1.99% linear growth). The graphite has a slightly rougher surface than the control, although the large pores present are still about 50 μm wide. The surface roughness extends right across the whole sample. In some areas there occur hillocks (Figure 597). A stereo-pair of this hillock is shown in Figure 601. The height of the hillock is about 15 μm, as measured from the stereo-pair.

Figures 602 to 608 are scanning electron micrographs of an 'as received' surface of pitch-coke graphite (SBO) after neutron-irradiation (+3.99% linear growth). The graphite has a very rough surface with many large pores about 100 μm wide (Figure 602). The surface has a few small protrusions on it as seen in Figure 604. The stereo-pair in Figure 608 shows the height of this protrusion to be about 20 μm. At high magnification (Figure 607) the surface is seen to be very rough when compared with the same magnification micrographs of LZAA (Figure 600) and virgin VQMB graphite (Figure 594). The irradiation has also

removed the machining marks on the side of the graphite cylinder (as seen in Figure 602). The overall surface is quite smooth; the peaks of the machining marks have been removed.

9.5.3. Edax Spectra. AGLMP Graphite.

The X-ray spectra in Figures 609, 611 and 613 show that aluminium, silicon and iron are present in both the virgin and the neutron-irradiated samples of AGLMP graphite. Small amounts of sulphur, chlorine, potassium and calcium are also present in the virgin sample but not the neutron-irradiated samples. The areas which are photographed (Figures 610, 612 and 614) show the differences in surface roughness between the three samples.

9.5.4. AGLMP Graphite. Non-polished Surfaces.

Figures 615 to 619 are scanning electron micrographs of an 'as received' surface of the virgin AGLMP Gilso-carbon (NA) graphite. The graphite has a fairly smooth surface but there are many scratch marks and rough areas to be seen (Figure 617). There are many pores about 30 μm to 50 μm on the surface (Figure 615).

Figures 620 to 624 are scanning electron micrographs of an 'as received' surface of Gilso-carbon (NA) graphite (FRC) after neutron-irradiation (-0.00% linear growth). The graphite

has been severely damaged as seen in Figure 620. The surface has become very rough with hillocks protruding on the surface. The main hillock seen in Figure 621 is about 40 μm high. There is no distinct edge around the hillock (Figure 622), its surface has a roughness comparable to all of the graphite surface i.e. a rough surface over the entire sample. The large pores (50 μm) are not as distinct as in the control sample (compare Figure 620 with Figure 615); the roughness has made the pore less easily detectable in the scanning electron microscope.

Figures 625 to 629 are scanning electron micrographs of an 'as received' surface of Gilso-carbon (NA) graphite (HAB) after neutron-irradiation (+4.0% linear growth). Again the graphite has been severely damaged as seen in Figure 625 and similar hillocks have appeared on the surface. The hillocks are of various sizes ranging from 500 μm (in the centre of Figure 626) to 70 μm (below and to the left of the large hillock in Figure 626). The surfaces of these hillocks are quite smooth when compared with the rest of the graphite surface. Many shrinkage cracks have appeared on the surface after neutron-irradiation; in Figure 625 cracks of 30 μm have appeared and in Figure 626 there is a shrinkage crack of 20 μm leading away from the central hillock.

9.5.5. VQMB Graphite. Polished Surfaces.

Figures 630 to 636 are optical and scanning electron micrographs of a polished surface of virgin VQMB pitch-coke graphite.

Figure 630 shows the optical texture of this graphite to possess a fine-mozaic structure containing little porosity. Figure 631 shows an anisotropic flow area with many long thin pores (5 μm to 10 μm wide) and flow-type anisotropy down the centre of the micrograph. This area has been studied by scanning electron microscopy as seen in Figures 633 to 636. Position A has been marked on the micrograph to identify the same area photographed using the optical and scanning electron microscopes. Figure 632 shows an overall picture of the graphite surface. The pore sizes have two distinct catagories; ~150 μm and ~10 μm wide. Figure 633 shows an area of these smaller pores.

Figures 637 to 643 are optical and scanning electron micrographs of a polished surface of pitch-coke graphite (LZAA) after neutron-irradiation (~1.99% linear growth). Figure 637 shows the optical texture to be of fine mozaics (see Section 1.4.) with low porosity very similar to Figure 630 which is a micrograph of the control sample. Figure 638 shows flow-type anisotropy with long thin pores (5 μm to 10 μm wide). The area selected here is not as porous as the area selected in the control sample (Figure 631). The same area is shown in Figures 640 to 643; Position B has been marked on the micrographs for ease of identification. Figure 639 shows an overall low magnification

micrograph of the graphite surface. Again, as in the control sample, there are two distinct pore sizes; ~150 μm and ~10 μm wide. The surface shown here is very similar to the control sample (Figure 632). This type of surface is observed when the rough 'as received' end-surface of the sliver is studied (Figures 590 and 595) by scanning electron microscopy. There was little change in the surface topography. Even at high magnification (Figure 643) the topography of the surface is very similar to that of the control.

Figures 644 to 650 are optical and scanning electron micrographs of a polished surface of pitch-coke graphite (SBO) after neutron-irradiation (+3.01% linear growth). Figure 644 shows an optical texture of fine-mozaics with many small pores (~2 μm wide) across the entire surface. This is quite different to the area seen in the previous two samples; there are many small pores present. Figure 645 shows an area with larger pores (~20 μm to ~50 μm) and many small pores (~2 μm) covering the surface. This is more clearly seen in Figures 647 and 648 which are scanning electron micrographs of the same area. Position C is marked on the micrograph for identification. The shaded areas, i.e. around the 50 μm pore at the top of Figure 647, are the resin in which the sample was embedded for polishing. Figure 646 shows an overall low magnification micrograph of the surface. The pores are very similar in size to those of the control sample, although

there appear to be more small pores (~10 μm) present than there are in the control. At high magnifications (Figure 650) the whole surface is seen to be pitted with very small pores (~0.3 μm) which are quite different from those in the previous two samples, as already seen by comparing Figure 602 with Figures 590 and 595.

9.5.6. AGLMP Graphite. Polished Surfaces.

Figures 651 to 657 are optical and scanning electron micrographs of a polished surface of virgin AGLMP Gilso-carbon (NA) graphite. Figure 651 shows an area with many long thin pores (~1 μm to 5 μm wide). This area is also seen in Figures 654 to 657. Position D is marked on the micrographs for identification. Figure 652 is an optical micrograph of an area showing the characteristic concentric pore structure of Gilso-carbon graphite with an optical texture of small size. Figure 653 shows an overall picture of the area of the surface. Many of the pores are about 50 μm and about 10 μm in size. There are smaller pores present which are not visible at this magnification. Figures 654 to 657 show long, thin pores which are interconnecting. At high magnification (Figure 657) the surface is smooth and free from very small pores (~0.5 μm).

Figures 658 to 664 are optical and scanning electron micrographs of polished surfaces of Gilso-carbon graphite (FRC) after neutron-

irradiation (-0.00% linear growth). Figure 658 shows an area which is quite heterogeneous in terms of optical texture with many anisotropic areas of different sizes. The same area is seen by scanning electron microscopy in Figures 660 to 664. Position E is marked on the micrographs for identification. Figure 659 is an optical micrograph of a Gilso-carbon pore area and shows the characteristic circular anisotropic structure. Some of the concentric pores have been filled in with anisotropic material (notethe blue and yellow areas). Figure 660 shows an overall micrograph of the surface at low magnification. The large pores are slightly larger than in the control sample i.e. about 100 μm. The area shown in Figure 661 has many small pores about 2 μm wide. Some of the pores on the surface have been filled with resin when the sample was embedded for polishing. At high magnification (Figure 664) the surface is found to be more porous than the surface of the control graphite.

Figures 665 to 671 are optical and scanning electron micrographs of a polished surface of Gilso-carbon graphite (HAB) after neutron-irradiation (+4.0% linear growth). Figure 665 shows an area with several pores ranging from about 2 μm to 60 μm. The plain, dark purple areas on this micrograph are surfaces of resin. This graphite has many areas filled with resin, as seen in Figure 668. Position F is marked on the micrographs to identify the

same positions. The characteristic Gilso-carbon pore areas are difficult to find in this irradiated graphite; they have apparently disappeared during irradiation. Figure 666 shows structures which are the nearest that could be found to the concentric pore structure. Despite the irradiation damage, most of the optical texture is retained. Figure 667 shows the overall surface at low magnification. Gilso-carbon pore structures cannot be seen in this micrograph. This irradiated sample differs from the control in that there are less small pores (cf. Figure 653). The large pores (80 μm to 100 μm) are slightly larger than those present in the control. There are also long, thin pores (10 μm to 20 μm) which are filled with resin. Many of these pores are interconnecting as seen in Figure 668. At high magnification (Figure 671) the surface is free from small pores, unlike the previous sample (Figure 664), where the surface was pitted with pores about 0.2 μm wide.

9.6. Conclusions.

From the EDAX analysis the irradiated samples did not contain any elements that were different from the control samples.

From studying the topography of the 'as received' surfaces, the two pitch-coke irradiated samples (VQMB graphite) showed different topographical features. LZAA (-1.99% linear growth)

has a slightly roughened surface with a few quite smooth hillocks present (Figure 597). SBO (+ 3.99% linear growth) has a very roughened surface as if it had been severely damaged. There were a few protrusions which were quite rough (Figure 604) on the surface of the graphite.

The two Gilso-carbon irradiated samples (AGLMP graphite) have surfaces of similar topography. Both surfaces are rough compared with the control and both have hillocks present on the surface. FRC (- 0.00% linear growth) has hillocks with rough surfaces (Figure 621) which merge gradually into the surface of the rest of the sample. HAB (+ 4.0% linear growth) has hillocks with quite smooth surfaces (Figure 626) which have a distinct edge to them, adjoining the rest of the surface. These hillocks vary in size from 50 μm to 500 μm and have shrinkage cracks running from the centre outwards.

From studies of polished surfaces, the two pitch-coke irradiated samples (VQMB graphite) were different. LZAA (- 1.99% linear growth) shows little difference from the control; there are a few larger pores present (50 μm to 100 μm). SBO (+ 3.01% linear growth) is more porous and has many small pores (~10 μm wide) on the surface. In studies of the two Gilso-carbon irradiated samples (AGLMP graphite), the characteristic Gilso-carbon pore structure has almost disappeared in the FRC (0.00% linear

growth) sample and has completely disappeared in the HAB (+4.0% linear growth) sample. In the FRC sample, the large pores are slightly larger than the control (about 100 μm). In the HAB sample the large pores are about 80 μm to 100 μm, but there do not appear to be as many small pores (~5 μm) on the surface. Some long, thin pores (10 μm to 20 μm wide) have become filled with resin during preparation for polishing.

Neutron-irradiation appears to completely change the topography of surfaces of the graphite samples inducing roughness and causing hillocks to grow on the surface. However, polished surfaces show little changes in the optical texture apart from increases in porosity. This non-destruction of the optical texture indicates that the main 'crystallinity' (size and orientation of the 'crystals') of the graphites withstands the irradiation. It was not possible to monitor the optical texture of the hillocks. The pitch-coke and Gilso-carbon graphites behaved similarly under irradiation conditions.

Although the size of, and the bulk orientation of the constituent units within the crystals remains unchanged as shown by the optical texture, there must occur changes in structure at dimensions <50 nm. These changes in the orientation and size of the constituent units (layers or molecules) may be revealed by phase-contrast electron microscopy.

CHAPTER 10

FURTHER STUDIES OF POROSITY BY PROGRESSIVE POLISHING OF VIRGIN GRAPHITES

10.1. Introduction.

In order to ascertain the feasibility of analysis of pore structure in the bulk material, optical and scanning electron microscopy studies are made of virgin graphites, using progressive polishing, i.e. the study is a progressive one. It is a requirement to know if the interconnectivities of pores and their relative positions can be monitored by progressively polishing into the bulk of the graphite. Photo-montages are constructed from scanning electron micrographs of each progressive layer exposed by polishing, and porosity in these successive photo-montages is analyzed to create a three-dimensional model.

10.2. Samples and Sample Preparation.

The samples studied by microscopy were:

VQMB
VNMC } pitch-coke graphites
VNEA

AGLCP a unipore cold - pressed graphite

UMP unimpregnated AGLMP gilso-carbon graphite

GG a German natural graphite

Figure 672 is a mercury pore-size distribution for AGLCP graphite. Pore-size distributions for VQMB and VNMC are shown in Figures A11 and A12. Progressive polishing was carried out on AGLMP and VQMB graphite. The graphite surfaces were prepared and polished for optical microscopy (see Section 5.2.1.). The graphites for progressive polishing were marked with a clear, well-defined notch down one edge of the piece of graphite so that each area could be related to the notch after each polish in order to correlate, precisely the tortuosity of the porous system.

10.3. Experimental Methods.

10.3.1. Microscopy of Virgin Graphites.

Typical areas of the six virgin graphites were located. Optical and scanning electron micrographs of these areas were taken and studied.

10.3.2. Point-counting on AGLMP Graphite.

Point-counting was carried out on AGLMP graphite in order to find out what percentage of graphite was present in the characteristic Gilso-carbon structure. A Swift point-counter was used which consists of a stage (attached to the microscope

stage) movable in two directions which holds the sample. The surface of the graphite is viewed using the cross-wires of the eyepiece. The sample surface is scanned at 50 μm intervals by displacement using the point-counter. At each interval the position of the surface lying on the cross-wire is described using one of the four classifications; porous and non-porous in a characteristic Gilso-carbon structure, and porous and non-porous in any other area. Each point is counted on a register by pressing down a button on the counter which automatically moves the specimen by one interval. Three adjacent faces of the AGLMP graphite were so classified. Three thousand counts were made on each face and the average value calculated for each classification.

10.3.3. Progressive Polishing of Graphites.

Photo-montages were taken of two areas on the AGLMP graphite and two areas on the VQMB graphite. The depth of polish was measured by focussing onto the polished surface in the optical microscope and then focussing on an easily recognisable area down the pore wall, or at the bottom of the pore. The distance travelled by the optical stage was calibrated in the optical microscope and gave (in micrometres) the depth of the pore and hence depth of surface polished away. Six to eight measurements were made on each graphite before and after each polish.

In the electron microscope the x and y positions of the notch and the x and y positions of each micrograph were recorded. During polishing the sample was not removed from the microscope stub. This helped in correctly aligning the sample in the microscope. Overlapping micrographs were taken of each area in order to build up complete photo-montages.

10.4. Results.

Figures 673 to 709 are optical and scanning electron micrographs of virgin VQMB, VNMC, VNEA, AGLCP, and UMP graphites and a German natural graphite.

Figure 30 gives the average values obtained from point counting studies made in each direction on virgin AGLMP graphite.

Figures 710, 711, 716 and 717 are photo-montages showing a large area (~2 mm^2) of AGLMP and VQMB graphites before and after progressive polishing.

Figures 712.1 to 715.10 are photo-montages of progressive polishing through ten layers of two areas of AGLMP graphite and two areas of VQMB graphite.

Table 31 shows the extent of graphite removal after each polish. Table 32 gives reference positions for each photomontage from the well-defined notch made on the two graphites.

10.5. Discussion of Results.

10.5.1. Microscopy of Virgin Graphites .

Figures 673 to 680 are optical and scanning electron micrographs of virgin VQMB pitch-coke graphite. The optical texture seen in Figures 673 and 674 shows large areas of fine-mozaics which contain little or no porosity (centre area of Figure 674, around Position H). These fine-mosaics have coarse-mozaics surrounding them, as seen in both Figures 673 and 674. The area in Figure 673 (optical micrograph) is shown in Figures 675 and 676, (scanning electron micrographs). Position G is marked in order to identify the same area. At low magnification (Figure 675) this area is seen to contain pores about 10 μm to 20 μm. The area of the optical texture (Figure 674) is shown in Figures 677 to 680 (scanning electron micrographs). The two areas shown are both typical areas seen in VQMB graphite. Figure 677 shows several areas of low porosity (around Position H and at the top of the micrograph) of fine-mozaics. Around the circumference of these fine-mozaics (Position H) is a series of small pores, about 1 μm to 5 μm wide (Figure 677). This area

is the area of coarse-mozaics (Figure 674). Even at a higher magnification (Figure 679) the fine-mozaics are non-porous.

Figures 681 to 688 are optical and scanning electron micrographs of virgin VNMC, pitch-coke graphite. This graphite has a more heterogeneous optical texture than the above VQMB graphite. Figure 681 shows coarse-mozaics and near-circular pores, 20 μm to 30 μm diameter. Figure 682 shows flow-type anisotropy with long, thin pores, running parallel to the flow-type anisotropy. These pores are about 10 μm wide. The scanning electron micrographs (Figures 683 to 688) show two typical areas; the second of which is seen in Figure 682. Figure 683 contains large pores (50 μm wide) surrounded by non-porous areas, or areas with pores beyond the resolution of the micrograph. Figure 685 shows flow-type anisotropy with pores (10 μm to 20 μm diameter). Position J identifies the same area of Figure 682. This graphite VNMC is highly porous with a heterogeneous range of pore sizes contained within flow-type anisotropy of similar appearance to the petroleum-coke graphites, e.g. Lima and PGA L18 graphites.

Figures 689 to 696 are optical and scanning electron micrographs of VNEA pitch-coke graphite. Figure 689 shows an optical texture (medium and large mozaics) similar to the graphite

VNMC (Figures 681) but with smaller curved pores (5 μm to 10 μm width). In Figure 690 a central, isotropic, non-porous purple area is surrounded on three sides by a long, thin pore varying in width from 5 μm to 40 μm. This central area is probably carbon from the resin which is used as an impregnant during graphite manufacture. Figures 691 to 696 are scanning electron micrographs of the two areas in Figures 689 and 690. Figures 691 and 692 show that the pore structure consists of two size ranges; 1 μm to 5 μm and 20 μm to 30 μm. There may also be pores present below the resolution of these micrographs. Figure 695 and 696 show the boundary between the resin and the graphite with a fizzure to the left but continuous to the right. In Figure 695, the upper smooth carbon from the resin is distinguishable from the lower porous (~1 μm) surface of the graphite. The pore structure in VNEA is fairly uniform, the majority of pores being about 5 μm wide.

Figures 697 to 701 are optical and scanning electron micrographs of AGLCP unipore graphite. The optical micrograph, Figure 697, shows fine-grain mozaics and isotropic material about 40 μm wide seen in the centre of the micrograph. The polished surface shows uniform pores of ~20 μm width. The scanning electron micrographs (Figures 698 to 701) show this uniformity of pore size (similar to Morgans EYC 9106 graphite, Figures 27 and 28).

Figures 702 to 708 are optical and scanning electron micrographs of UMP, unimpregnated AGLMP graphite. This graphite was studied in order to determine where the impregnant goes in AGLMP graphite. However, the optical texture and pore structure were indistinguishable from AGLMP graphite.

Figure 709 is an optical micrograph of the German natural graphite. This graphite is difficult to polish. It produced a surface which scratched easily. This graphite is homogeneous with an optical texture of large mozaics and low porosity 5 μm to 10 μm in width.

10.5.2. Point-Counting on AGLMP Graphite.

Table 30 lists percentages of a) porosity in the two structural components to this graphite and b) the contents of these two components. These percentages are given for surfaces polished in three directions through the graphite and are taken from three thousand counts on each surface. In the characteristic Gilso-carbon area the percentages in the first and second direction (Table 30) are closer in value than the percentages in the third direction which indicates that this structure is not symmetrical in all three directions i.e. it is not spherical in shape.

10.5.3.Progressive Polishing of Graphites.

Figure 710 is a photo-montage from scanning electron micrographs of AGLMP graphite with the two areas of study (Area 1, Area 2) marked as A1 and A2, these areas being of the circular Gilso-carbon found in AGLMP graphite.

Figure 711 is a photo-montage from scanning electron micrographs of VQMB graphite with the two areas of study (Area 1, Area 2) marked as V1 and V2 with different pore structures. Area 1 has many individual pores with one large pore in the centre whereas Area 2 has a series of interconnecting transport pores.

Figures 712.1 to 712.10 are photo-montages from scanning electron micrographs of Area 1(A1) of AGLMP graphite (Figure 710) through ten polishes. Position X is marked on Figures 712.3 to 712.10 at equal distances from the notch made on the sample edge. These positions mark the reference point for each photo-montage. The pores were traced from the SEM photo-montages onto transparent acetate paper for each layer to enable the porosity to be superimposed and visible. This technique indicates how the porosity changes direction and shape within the three dimensions of the graphite i.e. the tortuosity of the pores.

These acetate overlays are in an envelope in the rear cover of this Thesis.

The transparent photo-montages show, for the porosity, changes in shape, the appearances and disappearances with distance and the interconnectivities in the graphite.

The photo-montage (Figure 712.1) shows the initial area of study of the Gilso-carbon constituent of the AGLMP graphite. Figure 712.5. i.e. the 'surface' 29 μm below that of Figure 712.1 shows that the pore, Position M, has disappeared and the concentric pores, Position N, around the centre pore are becomming very shallow. The pore, Position O, has become narrower (~60 μm to 40 μm) from Figure 712.1 to Figure 712.5. In Figure 712.7 a new pore is present in the centre of the Gilso-carbon area, but in Figure 712.10 (26 μm below the 'surface' of Figure 712.7) the pore has disappeared.

Figures 713.1 to 713.10 are photo-montages from scanning electron micrographs of the surface of AGLMP graphite taken of an area (A2) larger than in the series of Figures 712.1 to 712.10. The characteristic porosity of Gilso-carbon is seen together with larger open pores at the top of the photo-montage. These two large pores are connected by very thin pores (<1 μm),

Position P in Figure 713.1. In Figure 713.2 these thin pores, Position P, have disappeared and the large pores are no longer connected. As polishing continues (Figure 713.4, 19 μm below the 'surface' of Figure 713.1) the pore to the right of Position P has split into two pores. By following these pores through the graphite the irregularity in the pore shapes can be seen.

Figures 713.1 to 713.10 show that the central pore of the Gilso-carbon becomes both wider and longer from ~15 μm wide and ~130 μm long (Figure 713.1) to ~20 μm wide and ~200 μm long (Figure 713.4). The width decreases with constant length to ~8 μm in Figure 713.10. By measuring the distance of the pore from Position X it is found that the position of the pore moves down away from the centre of the Gilso-carbon area in Figure 713.10.

A circular pore (80 μm wide), Position Q, has appeared in Figure 713.9 (not visible in Figure 713.8). This pore must be shallow (~10 μm) as it appeared after removing only 5 μm of graphite. In Figure 713.10, the base of the pore is now level with the polished surface.

Figures 714.1 to 714.10 are photo-montages from scanning electron micrographs of Area 1 (V1) of VQMB graphite through ten polishes. Figure 714.1 shows a large pore (~150 μm wide)

in the centre which enlargens (~200 µm wide) as polishing progresses. A pore Position R, has appeared after the second polish (Figure 714.2). This is a shallow pore (Figure 714.3) with a depth of ~15 µm and a width of ~75 µm. The curved pore, Position S, (~50 µm long after the first, initial, polish) gradually increases in length to ~250 µm (Figure 714.10) by coalescing with other pores. This pore could be classed as a transport pore, because it connects pores together.

Figures 715.1 to 715.10 are photo-montages from scanning electron micrographs of Area 2 (V2) of VQMB graphite. This area shows a transport pore system, Position T, at the top of the photo-montage. By following these pores through the polished layers they are seen to connect with pores in Figure 715.6 and link a large pore, Position U, with a pore, Position V, in Figure 715.10; the pores are connected from one side to the other side of the photo-montage.

Figures 716 and 717 are the areas shown in Figures 710 and 711 after the tenth (final) polish. After the final polish the two areas V1 and V2 in Figure 717 are almost connected together by pores, whereas in Figure 711 after the first (initial) polish, there were few pores between them. In Figure 716, the Gilso-carbon areas that were present in Figure 710 are all still distinct after the ten polishes.

10.6. Conclusions.

Point-counting on AGLMP graphite shows that the characteristic Gilso-carbon structure accounts for 23% to 30% of the total area, but only 2% to 3% of the total porosity.

Progressive polishing is a new technique for visually following the pore system through the three-dimensions of the graphite and studying interconnectivities between pores. Transport pores were identified when pores gradually connected up across the piece of graphite.

CHAPTER 11

CONCLUSIONS

1. Optical and scanning electron microscopy, coupled with Quantimet analyses have proved to be the best methods of assessment of porosity in the graphites of this study.

2. By correlating the optical texture of polished surfaces of graphites with surface topography following gasification, it is shown that fizzures develop in directions parallel to the basal planes in flow-type anisotropy and near-circular pores develop at the position of mozaics. Similar forms of optical texture behave similarly when oxidised with molecular oxygen, carbon dioxide and atomic oxygen, to comparable weight losses.

3. Non-destructive ultrasonic testing of graphites can detect changes in porosity following gasification. It has another advantage, that with progressive polishing the uniformity of gasification within the graphite can be assessed. But, it is not yet feasible to relate, quantitatively, changes in pulse velocity to pore-size and shape and to extent of porosity.

4. Comparisons are made between the radiolytically oxidised graphites (BAEL pitch-coke graphites) and their controls. Porosity increases are mainly in the pore-size range 10 μm to 50 μm. It is difficult, because of different extents of oxidation, to ascertain precisely the effect of methane on the development of porosity during radiolytic oxidation of graphites, but it would appear that the mechanisms of increase in pore volume are comparable. A comparison of a polished surface of radiolytically oxidised Lima graphite with thermally oxidised Lima graphite (~9% weight loss) shows that during radiolytic oxidation pores between 10 μm and 20 μm develop evenly over the surface. During thermal oxidation, many non-porous areas (~200 μm wide) remain and large pores develop 50 μm to 150 μm in diameter. It has not been possible to ascertain those factors which are responsible for the origin of a pore, in radiolytic oxidation, in the graphite surface.

5. Quantimet data has been processed to give the number of pores present in each size range, for the radiolytically oxidised samples and their controls. There is an increase of 850 pores in the size range 10 μm to 40 μm per 100 mm^2 of area after radiolytic oxidation of BAEL pitch-coke graphite to

8.8% weight loss. Field data show increases in: porosity, mean chords (intercepts) per pore (up to 150 μm), mean chords (intercepts) per pore walls (up to 150 μm), but a decrease in chords per pore walls above 150 μm. Shape factors show that the majority of pores are elliptical.

6. Neutron-irradiation of graphites completely changes the topographical features of the graphite surface and results in bulk damage within the graphite. Hillocks are produced which could be caused by differences in density between filler and binder. Neutron-irradiation does not destroy the optical texture. This indicates that the size and orientation of the 'crystallites' in the graphite remain unaffected during irradiation.

7. Progressive polishing and Quantimet analysis of each surface is a new approach to the study of porosity in graphites. It gives an assessment of porosity in three-dimensions within graphite. The application of this method to the problem of ventilation of porosity in graphites is possible. The presentation of a three-dimensional approach to the UKAEA was a major objective of this study. This has been accomplished and the method and data are now being applied by the staff of the UKAEA at Springfields.

REFERENCES

1. Bernal J.D., The Structure of Graphite, Proc. of Roy. Soc. A106 pp. 749-773, 1924.
2. Lipson H. and Stokes A.R., The Structure of Graphite, Proc. of Roy. Soc. A181 pp. 101-105, 1942.
3. Finch G.J. and Wilman H., The Diffraction of Electrons by Graphite, Proc. of Roy. Soc. A155 pp. 345-365, 1936.
4. Bacon G.E., A Note on the Rhombohedral Modification of Graphite, Acta. Cryst. 3 p.320, 1950.
5. Bacon G.E., The Reduction of the Crystallite Perfection of Graphite by Grinding, Acta Cryst. 5 p.392, 1952.
6. Boehm H.P. and Coughlin R.W., Enthalpy Difference of Hexagonal and Rhombohedral Graphite, Carbon 2 pp.1-6, 1964.
7. Laidler D. and Taylor A, Anomolous Diffractions in the Hull Debye-Scherrer Spectrum of Graphite, Nature 146 p.130, 1940.
8. Ubbelohde A.R. and Lewis F.A., Graphite and Its Crystal Compounds, Oxford Clarendon Press, Ch. 1, 1960.
9. Hull D., Introduction to Dislocations, Chapters 1 and 6, Pergamon Press, 1965.
10. Amelinckx S., Delavignette P, and Heerschap M., Dislocations and Stacking Faults in Graphite, Chem. and Phys. of Carbon, Ed. Walker P.L. Jr., 1 pp. 1-71, 1965.

11. Amelinckx S. and Delavignette P., Electron Optical Study of Basal Dislocations in Graphite, J. Appl. Phys 31 pp. 2126-2135, 1960.

12. Williamson G.K., Electron Microscope Studies of Dislocation Structures in Graphite, Proc. Roy. Soc. A257 pp. 457-463, 1960.

13. Horn F.H., Spiral Growth on Graphite, Nature 170 p.581, 1952.

14. Ban L.L., Crawford D. and Marsh H., Lattice-Resolution Electron Microscopy in Structural Studies of Non-Graphitizing Carbons from Polyvinylidene Chloride (PVDC), J. of Appl. Cryst. 8 pp. 415-420, 1975.

15. Franklin R.E., Crystallite Growth in Graphitizing and Non-Graphitizing Carbons, Proc. Roy. Soc. A209 pp. 196-218, 1951.

16. Mrozowski S., Mechanical Strength, Thermal Expansion and Structure of Cokes and Carbons , Proc. of 1st and 2nd Conf. on Carbon pp. 31-45, Buffalo, 1956.

17. Kipling J.J., Sherwood J.N., Shooter P.V. and Thompson N.R., Factors Influencing the Graphitization of Polymer Carbons, Carbon 1 pp. 315-320, 1964.

18. Kipling J.J. and Shooter P.V., Factors Affecting the Graphitization of Carbon: Evidence from Polarized Light Microscopy, Carbon 4 pp. 1-4, 1966.

19. Fitzer E., Mueller K. and Schaefer W., The Chemistry of the Pyrolytic Conversion of Organic Compounds to Carbon, Chem. and Phys. of Carbon, Ed. Walker P.L. Jr., 7 pp. 237-383, 1971.

20. Lewis R.T., Hot Stage Microscopy of Mesophase Pitches, Proc. of 12th Conf. on Carbon, pp. 215-216, Pittsburgh, 1975.

21. Brooks J.D. and Taylor G.H., the Formation of some Graphitizing Carbons, Chem. and Phys. of Carbon, Ed. Walker P.L. Jr., 4 pp. 243-286, 1968.

22. Marsh H., A Review of the Growth and Coalescence of Mesophase (Nematic Liquid Crystals) to form Anisotropic Carbon and its Relevance to Coking and Graphitization, Proc. of 4th Conf. on Ind. Carbon and Graphite, London pp. 2-38, 1974.

23. Marsh H. and Cornford C., Mesophase: The Precursor to Graphitizable Carbon, Petroleum Derived Carbons, Ed. Deviney M.L. and O'Grady T.M., A.C.S. Symposium Series, Washington, 1976.

24. White J.L., Mesophase Mechanisms in the Formation of the Microstructure of Petroleum Coke, Petroleum Derived Carbons, Ed. Deviney M.L. and O'Grady T.M., A.C.S. Symposium Series, Washington, 1976.

25. Marsh H., Carbonization and Liquid-Crystal (Mesophase). Development: Part 1. The Significance of Mesophase During Carbonization of Coking Coals, Fuel, 52 pp. 205-212, 1973.

26. Marsh H., Foster J.M., Hermon G. and Iley M., Carbonization and Liquid-Crystal (Mesophase) Development: Part 2. Co-Carbonization of Armoatic and Organic Dye Compounds and Influence of Inerts, Fuel, 52 pp. 234-242, 1973.

27. Marsh H., Foster J.M., Hermon G., Iley M. and Melvin J.N., Carbonization and Liquid-Crystal (Mesophase) Development, Part 3. Co-Carbonization of Aromatic and Heterocyclic Compounds containing Oxygen, Nitrogen and Sulphur, Fuel, 52 pp. 243-252, 1973.

28. Marsh H., Dachille F., Iley M., Walker P.L. Jr. and Whang P.W., Carbonization and Liquid-Crystal (Mesophase) Development, Part 4. Carbonization of Coal-Tar Pitches and Coals of Increasing Rank, Fuel, 52 pp. 253-261, 1973.

29. Honda H., Kimura H. and Sanada Y., Changes in Pleochroism and Extinction Contours in Carbonaceous Mesophase, Carbon 9 pp. 695-697, 1971.

30. Forrest R.A., and Marsh H., Reflection Interference Colours in Optical Microscopy of Carbons, Carbon, 15 pp. 348-349, 1977.

31. Forrest R.A., Structural Studies of Carbons, M.Sc. Thesis, University of Newcastle upon Tyne, 1977.

32. White J.L., and Zimmer J.E., Surface and Defect Properties of Solids, The Chemical Society, 5 pp. 16-35, 1976.

33. Marsh H., Akitt J.W., Hurley J.M., Melvin J. and Warburton A.P., Formation of Graphitizable Carbons from Gilsonite Pitch and Polyvinyl Chloride - A Mass Spectrometric and N.M.R. Study, J. Appl. Chem. 21 pp. 251-260, 1971.

34. De Gennes P., The Physics of Liquid-Crystals, Oxford Clarendon Press, 1974.

35. Pacault A., The Kinetics of Graphitization, Chem. and Phys. of Carbon, Ed. Walker P.L. Jr., 7 pp. 107-154, 1971.

36. Franklin R.E., The Structure of Graphitic Carbons, Acta Cryst. 4 pp. 253-261, 1951.

37. Maire J. and Méring J., Graphitization of Soft Carbons, Chem. and Phys. of Carbon, Ed. Walker P.L. Jr., 6 pp. 125-190 1970.

38. Pacault A., Marchand A., Gasparoux H., Flandrois S. and Rouillon J.-C., Étude Cinétique de la Graphitation, J. Chim. Phys. (Special Issue, April) pp. 104-120, 1969.

39. Fischbach D.B., The Kinetics and Mechanism of Graphitization, Chem. and Phys. of Carbon, Ed. Walker P.L. Jr., 7 pp. 1-105, 1971.

40. Ruland W., X-Ray Diffraction Studies on Carbon and Graphite, Chem. and Phys. of Carbon, Ed. Walker P.L. Jr., 4 pp. 1-84, 1968.

41. Marsh H. and WarburtonA.P.,The Catalysis of Graphitisation, J. Appl. Chem. 20 pp. 133-142, 1970.

42. Beine T. and Hutcheon J.M., The Shape of Ground Petroleum Coke Particles, Proc. of 1st and 2nd Conf. on Carbon, Buffalo, pp. 167-176, 1956.

43. Rusinko F. and Parker W.E., The Shape of Ground Petroleum Coke, Fuel 41 pp. 275-278, 1962.

44. Amstein E.H. and Watson C., The Shape of Carbon Grist Particles in the Manufacture of Carbon Electrodes, Proc. of 1st Conf. on Ind. Carbon and Graphite, London, pp. 125-131, 1958.

45. Darney A., Pitch Binder for Carbon Electrodes, Proc. of 1st Conf. on Ind. Carbon and Graphite, London, pp. 152-161,1958.

46. Eatherly W.P. and Piper E.L., Manufacture, Nuclear Graphite, Ed. Nightingale R.E., Ch. 2, Academic Press, 1962.

47. Hutcheon J.M., Manufacturing Technology of Baked and Graphitized Carbon Bodies, Modern Aspects of Graphite Technology, Ed. Blackman L.C.F., Ch. 2, pp. 49-78 Academic Press, 1970.

48. Price M.S.T. and Yeats F.W., Harwell Experimental Graphite Plant, Proc. of 1st Conf. on Ind. Carbon and Graphite, London, pp. 111-124, 1958.

49. Kopelman B., Materials for Nuclear Reactors, Ch. 8, McGraw Hill, 1959.

50. Nichols P.F. and Woodruff,E.M., Nuclear Properties, Nuclear Graphite, Ed. Nightingale R.E., Ch. 4, Academic Press, 1962.

51. Reynolds W.N., Physical Properties of Graphite, Ch. 7, Elsevier Publishing Co. Ltd., London, 1968.

52. Simmons J.H.W., Radiation Damage in Graphite, Pergamon Press, 1965.

53. De Halas D.R., Theory of Radiation Effect in Graphite, Nuclear Graphite, Ed. Nightingale R.E., Ch. 7, Academic Press, 1962.

54. Reynolds W.N., Physical Properties of Graphite, Ch. 1, Elsevier Publishing Co. Ltd., 1968.

55. IUPAC Appendices on Provisional Nomenclature, Symbols Units and Standards - Number 39. Definition, Terminology and Symbols in Colloid and Surface Chemistry - Part II Heterogeneous Catalysis, August 1974.

56. Nightingale R.E., Structure, Nuclear Graphite, Ed. Nightingale R.E., Ch. 5, Academic Press, 1962.

57. Reynolds W.N., Physical Properties of Graphite, Ch. 5, Elsevier Publishing Co. Ltd., 1968.

58. Crawford D. and Marsh H., High-Resolution Electron Microscopy in the Elucidation of Structure in Carbonaceous Materials, Proc. of 4th Conf. on Ind. Carbon and Graphite London, pp. 498-501, 1974.

59. Marsh H., The Kinetics of Formation of Mesophase, Chem. and Phys. of Carbon, Ed. Walker P.L. Jr., Marcel Dekker, 14. To be published.

60. Marsh H. and Crawford D., Progress Report 99, Northern Carbon Research Laboratories, School of Chemistry, University of Newcastle upon Tyne, 1975.

61. Trapnell B.M.W., Chemisorption, Ch. I, Butterworths, 1955.

62. Young D.M. and Crowell A.D., Physical Adsorption of Gases, Butterworths, 1962.

63. Brunauer S., Deming L.S., Deming W.S. and Teller E., On the Theory of the van der Waals Adsorption of Gases, J. Am. Chem. Soc. 62 pp. 1723-1732, 1940.

64. Brunauer S., Emmett P.H. and Teller E., Adsorption of Gases in Multimolecular Layers. J. Am. Chem. Soc. 60 pp. 309-319, 1938.

65. Langmuir I., The Adsorption of Gases on Plane Surfaces of Glass, Mica and Platinum, J. Am. Chem. Soc., 40 pp. 1361-1403, 1918.

66. Dubinin M.M., The Potential Theory of Adsorption of Gases and Vapors for Adsorbents with Energetically Non-uniform Surfaces, Chem. Rev. 60 pp. 235-241, 1960.

67. Dubinin M.M., Porous Structure and Adsorption Properties of Active Carbons, Chem. and Phys. of Carbon, Ed. Walker P.L. Jr., 2 pp. 51-120, 1966.

68. Gregg S.J. and Sing K.S.W., Adsorption, Surface Area and Porosity, Academic Press, 1967.

69. Scholten J.J.F., Mercury Porosimetry and Allied Techniques, Porous Carbon Solids, Ed. Bond R.L., Ch. VI Academic Press, 1967.

70. Washburn E.W., The Dynamics of Capillary Flow, Phys. Rev., 17 pp. 273-283, 1921.

71. Ritter H.L. and Drake L.C., Pore-Size Distribution in Porous Materials, - Pressure Porosimeter and Determination of Complete Macropore Size Distributions, Ind. Engng. Chem. Analyt. Edn. 17 pp. 782-786, 1945.

72. Drake L.C., Pore-Size Distribution in Porus Materials,- Application of High Pressure Mercury Porosimeter to Cracking Catalysts, Ind. Engng. Chem. 41 pp. 780-785, 1949.

73. Bikerman J.J., Surface Chemistry, Ch. 5, Academic Press, 1947.

74. Dickinson J.M. and Shore J.W., Observations Concerning the Determination of Porosities in Graphites, Carbon 6 pp. 937-941, 1968.

75. Baker D.J. and Morris J.B., Structural Damage in Graphite occurring during Pore Size Measurements by High Pressure Mercury, Carbon 9 pp. 687-690, 1971.

76. Lang F.M. and Magnier P., Studies of the Macroporosity of Carbons by use of Silver Impregnation and Soft X-Rays, Porous Carbon Solids, Ed. Bond R.L., Ch. VII Acadamic Press, 1967.

77. Jackson R. and Sharpe R.S., Radiographic Techniques applied to Carbons, Porous Carbon Solids, Ed. Bond R.L., Ch. VIII Academic Press, 1967.

78. Thomas J., Microscopic Studies of Graphite Oxidation, Chem.and Phys. of Carbon, Ed. Walker P.O. Jr., 1. pp. 121-202, 1965.

79. Rhead T.F.E. and Wheeler R.V., The Mode of Combustion of Carbon, J. Chem. Soc. 103 pp. 461-489, 1913.

80. Lowry H.H. and Huelett C.A., Studies in the Adsorption by Charcoal. II. Relation of Oxygen to Charcoal, J. Am. Chem. Soc. 42, pp. 1408-1419, 1920.

81. Marsh H. and Foord A.D., Mechanisms of Oxidation of Carbon by Molecular Oxygen, Carbon 11 pp. 421-424, 1973.

82. Phillips R., Vastola F.J. and Walker P.L. Jr., Factors affecting the Product Ratio of the Carbon-Oxygen Reaction.- II. Reaction Temperature, Carbon 8 pp. 205-210, 1970.

83. Puri B.R., Surface Complexes on Carbons, Chem. and Phys. of Carbon, Ed. Walker P.L. Jr., 6 pp. 191-282, 1970.

84. Ubbelohde A.R. and Lewis F.A., Graphite and its Crystal Compounds, Ch. 9, Oxford University Press, 1960.

85. Lobenstein W.R. and Deitz V.R., Oxygen Chemisorption on Carbon Adsorbents, J. Phys. Chem. 59 pp. 481-487, 1953.

86. Medalia A.I., Pothiawala H.V. and Hagopian E., Oxidation of Carbon Black (ISAF grade) with Oxygen, Proc. of 7th Conf. on Carbon, Cleveland, 1965 . Abstract: Carbon 3 p. 352, 1965.

87. Walker P.L. Jr., Austin L.G. and Tietjen J.J., Oxygen Chemisorption Effects on Graphite Thermoelectric Power, Chem. and Phys. of Carbon, Ed. Walker P.L. Jr. 1. pp. 327-365, 1965.

88. Vastola F.J., Hart P.J. and Walker P.L. Jr., A Study of Carbon-Oxygen Surface Complexes using O^{18} as a Tracer, Carbon 2 pp. 65-71, 1964.

89. Thomas J.M. and Roscoe C., Non-Basal Dislocations in Graphite, Chem. and Phys. of Carbon, Ed. Walker P.L. Jr., 3 pp. 1-44, 1968.

90. Lewis J.B., Thermal Gas Reactions of Graphite, Modern Aspects of Graphite Technology, Ed. Blackman L.C.F., Ch. 4 Academic Press, 1970.

91. Langmuir I., Chemical Reactions at Low Pressures, J. Am. Chem. Soc. 37 pp. 1139-1167, 1915.

92. Ramachandra Rao P.V.N. and Petersen E.E., Effect of CO_2 Concentration on Gasification of Artificial Graphites, Ind. and Engng. Chem. 50 No. 3 pp. 331-336, 1958.

93. McKee D.W. and McCarrol B., Reactivity of Graphite Surfaces with Atoms and Molecules of Hydrogen, Oxygen and Nitrogen, Proc. of 10th Conf. on Carbon, Bethlehem, Pennsylvania, pp. 16-17, 1971.

94. Thomas J.M., Topographical Studies of Oxidised Graphite Surfaces: A Summary of the Present Position, Carbon 7 pp. 359-364, 1969.

95. Lind R. and Wright J., Gas Reactions with Graphite in the AGR, J. Brit. Nucl. Energy Soc. 2 pp. 287-294, 1963.

96. Walker P.L. Jr., Rusinko F. and Austin L.G., Gas Reactions of Carbon, Adv. in Catalysis 11 pp. 133-221, 1959.

97. Long F.J. and Sykes K.W., The Catalysis of Oxidation of Carbon, J. Chim. Phys. 47 pp. 361-378, 1950.

98. Gadsby J., Long F.J., Sleightholm P. and Sykes K.W., The Mechanism of the Carbon Dioxide-Carbon Reaction, Proc. Roy. Soc. (A) 193 pp. 357-376, 1948.

99. Ergun S. and Mentser M., Reactions of Carbon with Carbon Dioxide and Steam, Chem. and Phys. of Carbon, Ed. Walker P.L. Jr., 1, Chap. 4, 1965.

100. Ergun S., Kinetics of the Reaction of Carbon Dioxide with Carbon, J. Phys. Chem. 60 pp. 480-485, 1956.

101. Bonner F. and Turkevich J., Study of the Carbon Dioxide-Carbon Reaction using C-14 as a Tracer, J. Am. Chem. Soc. 73 pp. 561-564, 1951.

102. Harker H., Marsh H. and Wynne Jones W.F.K., The Carbon-Carbon Dioxide Reaction, Proc. of 1st Conf. on Ind. Carbon and Graphite London, pp. 291-301, 1958.

103. Reif A.E., The Mechanism of the Carbon Dioxide-Carbon Reaction, J. Phys. Chem. 56 pp. 785-788, 1952.

104. Turkdogan E.T. and Vinters J.V., Effect of Carbon Monoxide on the Rate of Oxidation of Charcoal, Graphite and Coke in Carbon Dioxide, Carbon 8 pp. 39-53, 1970.

105. Grabke H.J., Oxygen Transfer and Carbon Gasification in the Reaction of Different Carbons with CO_2, Carbon 10 pp. 587-599, 1972.

106. Gulbransen E.A. and Andrew K.F., Reaction of Carbon Dioxide with Pure Artificial Graphite at Temperatures of 500° to 900°C. Ind. Engng. Chem. 44 pp. 1048-1051, 1952.

107. Lang F.M., May S. and Chenion J., Etude des Composés Formés au-dessous de 600°C par Action de CO_2, sur du Graphite, Proc. of 7th Conf. on Carbon, Cleveland, Abstract Carbon 3 p. 349, 1965.

108. Sykes K.W. and Thomas J.M., The Effects of Catalysts on the Gasification of Graphite and Diamond by Carbon Dioxide, J. Chim. Phys. 58 pp. 70-76, 1961.

109. Board J.A., The Thermal Oxidation of Nuclear Graphite in Carbon Dioxide, Proc. of 2nd Conf. on Ind. Carbon and Graphite, London, pp. 277-288, 1965.

110. Grabke H.J., Zer Kinetik der Reaktionem von Graphit mit CO_2 - CO - und H_2O - H_2 - Gemischen, Berichte der Bunsen Gesellschaft, 70 pp. 664-674, 1966.

111. Dubinin M.M, Plavnik G.M. and Zaverina E.D., Integrated Study of the Porous Structure of Active Carbons from Carbonized Sucrose, Carbon 2 pp. 261-268, 1964.

112. Kalback W.M., Brown L.F. and West R.E., The Growth of Pores in Graphitized Carbon Reacted with Carbon Dioxide, Carbon 8 pp. 117-124, 1970.

113. Walker P.L. Jr. and Raats E., Changes in Physical Properties of Graphitized Carbon Rods upon Gasification with Carbon Dioxide, J. Phys. Chem. 60 pp. 364-369, 1956.

114. Marsh H. and Rand B., The Process of Activation of Carbon by Gasification with CO_2 - 1. Gasification of Pure Polyfurfuryl Alcohol Carbon, Carbon 9 pp. 47-61, 1971.

115. Streznewski J. and Turkevich J., The Reaction of Carbon with Oxygen Atoms, Proc. of 3rd Conf. on Carbon, Buffalo, pp. 273-278, 1958.

116. Otterbein M. and Bonnetain L., Reaction du Carbone avec 1'Oxygen Atomique, Carbon 7 pp. 539-554, 1969.

117. Blackwood J.D. and McTaggart F.K., Reaction of Carbon with Atomic Gases, Aust. J. Chem. 12 pp. 533-542, 1959.

118. Vastola F.J., Walker P.L. Jr. and Wightman J.P., The Reaction between Carbon and the Products of Hydrogen, Oxygen and Water Microwave Discharges, Carbon 1 pp. 11-16, 1963.

119. Marsh H. and O'Hair T.E., The Formation of Surface Oxide by Carbons during Oxidation by Atomic Oxygen at different Temperatures, Proc. of 8th Conf. on Carbon, Buffalo, New York, 1967. Abstract: Carbon 6 p. 230, 1968.

120. Marsh H., O'Hair T.E. and Lord Wynne-Jones, The Carbon-Atomic Oxygen Reaction - Surface Oxide Formation on Paracrystalline Carbon and Graphite, Carbon 7 pp. 555-556, 1969.

121. Marsh H., O'Hair T.E., and Wynne-Jones W.F.K., Oxidation of Carbons and Graphites by Atomic Oxygen, Kinetic Studies, Trans. Far. Soc. 61 pp. 274-284, 1965.

122. Marsh H., O'Hair T.E. and Reed R., Oxidation of Carbons and Graphites by Atomic Oxygen. An Electron Microscope Study of Surface Changes, Trans. Far. Soc. 61 pp. 285-293, 1965.

123. Marsh H., Northern Coke Research Laboratories,Univeristy of Newcastle upon Tyne Progress Report 75, 1964.

124. Lang F.M., Magnier P. and Brie M., Oxydation a Pression Atmospherique du Graphite par l'Oxygene Atomique obtenu par Decomposition d'Ozone, Proc. of 2nd Conf. on Ind. Carbon and Graphite, London, pp. 243-247, 1965.

125. Rosner D.E. and Allendorf H.D., High Temperature Oxidation of Carbon by Atomic Oxygen. Carbon 3 pp. 153-156, 1965.

126. Foord A.D., Ph.D. Thesis, University of Newcastle upon Tyne, 1972.

127. Shahin M.M., Reaction of Elementary Carbon and Hydrogen in High Frequency Discharge, Nature Lond. 195 pp. 992-993, 1962.

128. King A.B. and Wise H., Reaction Kinetics of Hydrogen Atoms with Carbon Films, J. Phys. Chem. 67 pp. 1163-1170, 1963.

129. Clark T.J., Woodley R.E. and De Halas D.R., Gas-Graphite Systems, Nuclear Graphite, Ed. Nightingale R.E., Ch. 14 Academic Press, 1962.

130. Tonge B.L., A Preliminary Study of Surface Oxide produced by Reaction of Carbon and Carbon Dioxide, Proc. of 4th Conf. on Carbon, Buffalo, pp. 87-93, 1959.

131. Anderson A.R., Davidson H.W., Lind R., Stranks D.R., Tyzack C. and Wright J., Chemical Studies of Carbon Dioxide and Graphite under Reactor Conditions, Proc. of 2nd U.N. Int. Conf. on the Peaceful Uses of Atomic Energy, Geneva. Vol. 7 pp. 335-373, 1958.

132. Hutcheon J.M., Cowen H.C. and Godwin N.F., The Role of Pore Structure in the Oxidation of Graphite by Irradiated Carbon Dioxide, Proc. of 5th Conf. on Carbon, Pennsylvania. Vol. 2 pp. 379-386, Pergamon Press, 1963.

133. Campion P., Lind R., Blanchard R.J. and Koch C., The Influence of Pore Structure on the Radiolytic Carbon Dioxide/Graphite Reaction. Proc. of 4th Conf. on Ind. Carbon and Graphite, London pp. 459-468, 1974.

134. Standring J. and Ashton B.W., The Effect of Radiolytic Oxidation by Carbon Dioxide on the Porosity of Graphite, Carbon 3 pp. 157-165, 1965.

135. Feates F.S. and Walker F.A., The Radiolytic Reaction between Graphite and Carbon Dioxide - I. Primary Gasification Products, Carbon 9 pp. 11-18, 1971.

136. Feates F.S. and Fryer J.R., The Radiolytic Reaction between Graphite and Carbon Dioxide - III. Surface Complexes, Carbon 9 pp. 511-516, 1971.

137. Copestake T.B., Davidson H.W. and Tonge B.L., A Study of the Reactions of Graphite with Carbon Dioxide with Reference to Gas-Cooled Nuclear Reactors, J. Appl. Chem. 9 pp. 74-84, 1959.

138. Dominey D.A. and Morley H., The Radiolytic Reaction between Graphite and Carbon Dioxide. IV. The Influence of Carbon Monoxide, Carbon 9 pp. 725-732, 1971.

139. Best J.V., Dominey D.A. and Wood C.J., The Radiolytic Graphite/Carbon Dioxide Reaction : The Effect of Carbon Monoxide at 225-375°C, Carbon 10 pp. 317-322, 1972.

140. Campion P., Blanchard A., Lind R., Blanchard R.J. and Koch C., The Effect of Coolant Composition on the Radiolytic Carbon Dioxide/Graphite Reaction. Proc. of 4th Conf. on Ind. Carbon and Graphite, pp. 452-458, 1974.

141. Parsons P.D., Hand K. and Schofield P., Microscopic Observations of Pore Structure of Graphites using Metal Impregnation, U.K.A.E.A. TRG Report 2830(S), 1976.

142. British Steel Corporation, Internal Report, OPER/2/73/C, Feb. 1973.

143. Wells O.C., Scanning Electron Microscopy, McGraw Hill, New York, 1974.

144. Hearle J.W.S., Sparrow J.T. and Cross P.M., The Use of the S.E.M., Ch. 11, 1971.

145. Boyde A., The Single-Stage Carbon-Replica Method and some Related Techniques for the Analysis of the Electron Microscope Image, J. of Roy. Micros. Soc. 86, pp. 359-370, 1966.

146. Butler D.W., A Stereo Electron Microscope Technique for Microtopographic Measurements, Micron 4 pp. 410-424, 1973.

147. Oshima K., Kimoto S. and Suganuma T., Stereomicrography with a Scanning Electron Microscope, Photogrammetric Engineering. 36 pp. 874-879, 1970.

148. Boyde A., Ross H.F. and Bucknall W.B., Plotting Instruments for use with Images Produced by Scanning Electron Microscopy, Biostereometrics, Ed. Karara H.M. and Herron R.E., Am. Soc. of Photogramm., Falls Church, Virginia, 1974.

149. Boyde A. and Ross H.F., Photogrammetry and the Scanning Electron Microscope, Photogramm. Record., 46 pp. 408-457, 1975.

150. Underwood E.E., Quantitative Stereology, Ch. 1, Addison Wesley, Reading, Mass., 1970

151. Weibel E.R., Kistler G.S. and Scherle W.F., Practical Stereological Methods for Morphometric Cytology, Journal of Cell Biology, 30 pp.23-27, 1966.

152. Underwood E.E., Quantitative Stereology, Ch. 2, Addison Wesley, Reading, Mass., 1970.

153. British Steel Corporation, Coke Structural Analysis The Use of Quantimet 720, Report OPER/502/2/74/C, June, 1974.

154. Davidson T.D., Application of Sonic, Ultrasonic and Inductive Techniques to the Non-Destructive Testing of Carbon. Proc. of 1st Conf. on Ind. Carbon and Graphite, London, pp. 585-593, 1958.

155. Thrower P.A. and Bognet J.C., The Effect of Oxidation on the Compressive Strength of Graphite. Proc. of 13th Conf. on Carbon, Irvine, California, pp. 265-266, 1977.

156. Rounthwaite C., Lyons G.A. and Snowdon R.A., Influence of Thermal Corrosion on the Strength, Permeability and Frictional Properties of Nuclear Graphite, Proc. of 2nd Conf. on Ind. Carbon and Graphite. London, pp. 299-319, 1965.

157. Peng T.C., Effects of Oxidation on the Mechanical Properties of Carbon/Graphite, Proc. of 13th Conf. on Carbon, Irvine, California, pp. 263-264, 1977.

158. Board J.A. and Squires R.L., The Effect of Oxidation in CO_2 on Graphite Strength, Proc. of 2nd Conf. on Ind. Carbon and Graphite, London, pp. 289-297, 1965.

159. Morgan W.C. and Becker F.L., Correlation of Strength with Physical Properties, Proc. of 13th Conf. on Carbon, Irvine, California, pp. 261-262, 1977.

160. PUNDIT Manual for use with the Portable Ultrasonic Non-Destructive Digital Indicating Tester. C.N.S. Instruments Ltd., London, 1976.

161. Marsh H., Iley M., Berger J. and Siemieniewska T., The Adsorptive Properties of Activated Plum Stone Chars, Carbon 13 pp. 103-109, 1975.

162. Augustyn D., Iley M. and Marsh H., Optical and Scanning Electron Microscope Study of Brown Coals, Fuel 55 pp. 25-38, 1976.

163. O'Conner M.F., Brocklehurst J.E. and Kelly B.T., Structural Integrity of Nuclear Graphites at High Fast Neutron Doses, Proc. of 5th Int. Carbon and Graphite Conf. London, pp. 898-903, 1978.

164. Kelly B.T. and Brocklehurst J.E., High Dose Fast Neutron Irradiation of Highly Oriented Pyrolytic Graphite, Carbon 9 pp. 783-789, 1971.

Properties	AGLMP	BAEL GCMB	AGLHP	MORGANS EYC 9106	LIMA	PGA L18	BAEL VQMB	BAEL VNMC
Density g cm^{-3}	1.82	1.81	1.56	1.65	1.68	-	1.85	1.76
Total O.P.V.	11.7	12.9	22.5	12.8	21.0	16.6	10.8	16.3
O.P.V. down to 50 μm	0.8	0.8	0.5	0.2	0.6	0.0	1.5	0.7
O.P.V. down to 10 μm	4.3	8.3	15.7	0.7	4.3	3.4	4.3	9.3
O.P.V. down to 5 μm	5.7	8.8	17.7	3.0	6.2	6.6	5.0	10.4
O.P.V. down to 1 μm	8.1	10.2	20.0	10.5	13.2	12.5	6.7	12.7
O.P.V. down to 0.5 μm	8.7	10.5	20.3	11.3	14.5	13.2	7.0	13.1
O.P.V. down to 0.1 μm	9.7	11.3	20.8	12.3	15.6	14.9	7.7	13.7
O.P.V. down to 0.05 μm	10.0	11.5	21.0	12.5	16.3	15.3	8.4	14.5
O.P.V. down to 0.02 μm	11.0	12.4	22.0	12.7	19.0	16.6	10.3	15.9

Table 1. Properties of the Graphites that were studied.

TYPE OF AGLMP GRAPHITE	BULK DENSITY g cm^{-3}	O.P.V. %	C.P.V. %	DIFFUSIVITY RATIO
Virgin	1.78	11.70	8.10	0.039
5.4% oxidized	1.72	20.17	3.81	0.019
10.5% oxidized	1.62	25.69	2.89	0.003

Table 2. Pore Structure Data of AGLMP Graphite.

FIGURE	POSITION	PORE SHAPE
43	A	Circular pore 300 nm diameter.
44	B	L-shaped pore, 900 nm long, 300 nm wide.
44	C	Thin, curved pore.
44	D	Triangular-shaped pore.
44	E	Long, thin pore 3 μm long, 600 nm wide, forming two channels at one side.
45	F	Heart-shaped pore, 700 nm wide.
45	G	Circular pore, 800 nm diameter
45	H	Long, thin pore 3 μm long 200 nm wide.
46	I	Long, thin pore 1 μm long 200 nm wide.
46	J	Circular pore 400 nm diameter.
48	K	Pore 800 nm long, 300 nm wide.
48	L	Spherical piece of mercury lying on the surface.
48	M	Spherical piece of mercury lying independent of the pore structure.
49	N	Superimposition of a circular pore, 300 nm diameter above another pore.
49	O	Pore, 1.5 μm long, 300 nm wide.

Table 3. Pore Shapes detected in Lima Graphite using the High-Voltage Electron Microscope.

FEATURES	DIMENSIONS			
	mm^0	mm^{-1}	mm^{-2}	mm^{-3}
Points	P_P	P_L	P_A	P_V
Lines	L_L	L_A	L_V	
Areas	A_A	S_V		
Volumes	V_V			

Table 4. Relationship between Two Dimensional and Three Dimensional Parameters.

TYPE OF GRAPHITE	O.P.V. FROM MERCURY POROSIMETRY DOWN TO 0.7μm %	QUANTIMET DATA								
		OPEN AND CLOSED POROSITY %	STANDARD ERROR	MEAN INTERCEPT		STANDARD ERROR		AVERAGE PERIMETER PER FIELD mm	AVERAGE COUNT PER FIELD	AVERAGE PERIMETER PER PORE μm
				WALL μm	PORE μm	WALL	PORE			
AGLMP	8.5	12.04	0.73	213.5	24.6	9.4	1.3	1.90	47	41
BAEL GCMB	10.2	8.21	0.69	238.6	16.8	15.7	1.4	1.88	55	34
AGLHP	20.2	14.16	0.39	83.3	13.4	1.3	0.3	4.15	97	43
MORGANS EYC 9106	11.0	13.42	0.29	53.2	8.1	0.8	0.2	6.59	152	43
LIMA	14.1	15.09	0.61	119.0	19.3	4.1	0.7	3.12	71	44
PGA L18	13.0	18.33	0.67	80.9	17.1	2.7	0.6	4.50	108	43
BAEL VQMB	6.9	11.81	1.50	302.3	39.1	26.7	12.6	1.66	62	27
BAEL VNMC	12.9	14.54	0.80	152.4	24.9	4.1	1.4	2.43	65	37

Table 5. Results obtained from the Quantimet 720.

Gasification Treatment	Temp/ K	Time	Weight losses/ % LIMA GRAPHITE		MORGANS EYC 9106 GRAPHITE		AGLMP GRAPHITE	
Air	973	1 hour	LG1	16.67	MG1	9.22	-	-
Air	873	1 hour	LG2	2.35	MG2	0.77	AG1	0.48
Air	823	1 hour	LG3	0.38	MG3	0.11	-	-
CO_2	973	16 hours	LG4	0.83	MG4	0.67	AG2	0.40
CO_2	1073	16 hours	-	-	-	-	AG2	0.76
CO_2	873	16 hours	LG5	0.11	MG5	0.04	AG3	0.27
CO_2	873	25 hours	LG6	0.03	MG6	0.02	-	-
$O^{\bullet}$	300	5 mins	LG7	0.98	-	-	-	-
$O^{\bullet}$	300	3 mins	LG8	0.57	-	-	AG4	0.32
$O^{\bullet}$	300	2 mins	LG9	0.15	-	-	-	-
$H^{\bullet}$	300	20 mins	LG10	0.08	-	-	-	-
$H^{\bullet}$	300	105 mins	LG11	0.12	-	-	-	-

Table 6. Description of Thermal and Atomic Gasification Treatments.

Temp/ K	Time / hours	Weight losses / %								
		LIMA GRAPHITE			MORGANS EYC 9106 GRAPHITE			AGLMP GRAPHITE		
		Sample	Partial	Total *	Sample	Partial	Total	Sample	Partial	Total
1073	16	LG12	1.64	-	MG7	0.60	-	AG5	1.34	-
1198	16	-	-	-	-	-	-	AG5	3.44	4.74
1088	48	LG13	1.42	-	-	-	-	AG6	0.48	-
1173	16	LG13	2.63	4.00	-	-	-	AG6	1.39	1.86
1138	16	LG14	2.00	-	MG8	0.85	-	AG7	0.81	-
1223	16	LG14	9.40	11.29	MG8	7.57	8.31	AG7	2.28	3.07
1173	16	LG15	3.65	-	-	-	-	-	-	-
1223	16	LG15	9.29	12.69	-	-	-	-	-	-
1198	16	LG16	5.31	-	MG9	1.40	-	AG8	1.07	-
1273	16	LG16	37.65	41.24	MG9	16.19	17.42	AG8	8.12	9.11
1243	16	LG17	5.99	-	MG10	6.04	-	AG9	3.30	-
873	16	LG18	0.45	-	-	-	-	AG10	0.67	-
873	80	LG18	3.23	3.62	-	-	-	AG10	4.29	4.90
973	96	LG18	1.34	5.93	-	-	-	AG10	1.83	6.69
1073	96	LG18	4.89	9.19	-	-	-	AG10	5.23	10.75
913	16	LG19	1.48	-	-	-	-	AG11	0.42	-
1073	16	-	-	-	-	-	-	AG12	1.13	-
1173	16	LG20	6.78	-	-	-	-	AG13	3.68	-

* Totals are calculated to include weight losses of previous runs (as a percentage)

Table 7. Description of Graphites Gasified in Carbon Dioxide.

Samples		Flow Rate / $mm^3 s^{-1}$	Temperature / K
LG13	AG6	500	1173
LG15		700	1173
LG18	AG10	700	873
LG19	AG11	440	913
	AG12	630	1073
LG20	AG13	700	1173

Table 8. Flow Rates of Carbon Dioxide during Gasification Treatments.

LIMA GRAPHITE	FIGURES	MORGANS GRAPHITE	FIGURES	AGLMP GRAPHITE	FIGURES
LG1	157-162	MG1	183-187	AG1	190-195
LG2	163-178	MG2	-	AG2	223-232
LG3	179-182	MG3	188-189	AG3	-
LG4	196-210	MG4	216-220	AG4	-
LG5	-	MG5	_	AG5	277-289
LG6	211-215	MG6	221-222	AG6	297-304
LG7	233-242	MG7	271-276	AG7	322-333
LG8	243-250	MG8	314-321	AG8	360-367
LG9	251-257	MG9	352-359	AG9	380-385
LG10	258-262	MG10	374-379	AG10	401-415
LG11	-			AG11	415.11-415.20
LG12	263-270			AG12	415.21-415.30
LG13	290-296			AG13	415.41-415.51
LG14	305-313				
LG15	334-341				
LG16	342-351				
LG17	368-373				
LG18	386-400				
LG19	415.1-415.10				
LG20	415.31-415.40				

Table 9. Relationship between Gasification Samples and Figure Numbers.

Pundit Samples	Gasification Samples	Figure Nos.
LP1	LG13	290-296
LP2	LG16	342-351
LP3	LG17	368-373
LP4	LG18	386-400
MP1	MG9	352-352
MP2	MG10	374-379
MP3	-	-
AP1	AG6	297-304
AP2	AG8	360-367
AP3	AG9	380-385
AP4	AG10	401-415

Table 10. Corresponding Pundit and Gasification Samples.

SAMPLE	TEMP / K	TOTAL WEIGHT LOSS / %	VELOCITY/km s^{-1}			VELOCITY CHANGE/km s^{-1}			$\frac{\text{VELOCITY CHANGE}}{\text{WEIGHT LOSS}}$ / km s^{-1} $\%^{-1}$		
			D_1	D_2	D_3	D_1	D_2	D_3	D_1	D_2	D_3
LP1	Virgin	0	2.535	2.210	2.001	-	-	-	-	-	-
LP1	1088	1.21	2.519	2.002	1.963	-0.016	-0.208	-0.038	-0.013	-0.172	-0.031
LP1	1173	2.75	2.478	1.983	1.935	-0.057	-0.227	-0.066	-0.021	-0.083	-0.024
LP1	Virgin	0	2.670	2.124	2.045	-	-	-	-	-	-
LP2	1198	2.40	2.455	1.998	1.910	-0.215	-0.126	-0.135	-0.090	-0.053	-0.056
LP2	1273	31.39	1.465	1.147	1.048	-1.205	-0.977	-0.977	-0.038	-0-031	-0.031
LP3	Virgin	0	2.588	2.156	2.100	-	-	-	-	-	-
LP3	1243	9.52	2.307	1.795	1.691	-0.281	-0.361	-0.409	-0.030	-0.038	-0.043
LP4	Virgin	0	2.454	2.169	2.050	-	-	-	-	-	-
LP4	873	1.07	2.556	2.087	1.854	+0.102	-0.082	-0.196	+0.095	-0.077	-0.183
LP4	973	3.05	2.535	2.154	2.010	+0.081	-0.015	-0.040	+0.027	-0.005	-0.013
LP4	1073	4.27	2.483	2.116	1.907	+0.029	-0.053	-0.143	+0.007	-0.012	-0.034

Table 11. Ultrasonic Velocities through Lima Graphite gasified in Carbon Dioxide.

SAMPLE	TEMP/ K	TOTAL WEIGHT LOSS / %	VELOCITY/ km s^{-1}			VELOCITY CHANGE/ km s^{-1}			$\frac{\text{VELOCITY CHANGE}}{\text{WEIGHT LOSS}}$ / km s^{-1} $\%^{-1}$		
			D_1	D_2	D_3	D_1	D_2	D_3	D_1	D_2	D_3
MP1	Virgin	0	2.049	2.082	1.802	-	-	-	-	-	-
MP1	1198	0.53	2.049	2.037	1.741	0	-0.045	-0.061	0	-0.085	-0.115
MP1	1273	5.95	2.006	1.930	1.593	-0.043	-0.152	-0.209	-0.007	-0.026	-0.035
MP2	Virgin	0	2.125	2.014	1.738	-	-	-	-	-	-
MP2	1243	2.05	1.937	1.778	1.615	-0.188	-0.236	-0.123	-0.092	-0.115	-0.060
MP3	Virgin	0	2.071	2.075	1.739	-	-	-	-	-	-
MP3	873	1.33	2.042	2.054	1.649	-0.029	-0.021	-0.090	-0.022	-0.016	-0.068
MP3	973	1.83	2.076	2.052	1.645	+0.005	-0.023	-0.094	+0.003	-0.013	-0.051
MP3	1073	2.45	2.081	2.073	1.648	+0.010	-0.002	-0.091	+0.004	-0.001	-0.037

Table 12. Ultrasonic Velocities through Morgans EYC 9106 Unipore Graphite gasified in Carbon Dioxide.

SAMPLE	TEMP / K	TOTAL WEIGHT LOSS / %	VELOCITY / km s^{-1}			VELOCITY CHANGE / km s^{-1}			$\frac{\text{VELOCITY CHANGE}}{\text{WEIGHT LOSS}}$ / km s^{-1} $\%^{-1}$		
			D_1	D_2	D_3	D_1	D_2	D_3	D_1	D_2	D_3
AP1	Virgin	0	2.300	2.221	2.211	-	-	-	-	-	-
AP1	1088	0.33	2.358	2.300	2.319	+0.058	+0.079	+0.108	+0.176	+0.239	+0.327
AP1	1173	0.75	2.311	2.273	2.415	+0.011	+0.052	+0.204	+0.015	+0.069	+0.272
AP2	Virgin	0	2.430	2.399	2.228	-	-	-	-	-	-
AP2	1198	0.46	2.295	2.342	2.111	-0.135	-0.057	-0.117	-0.294	-0.124	-0.254
AP2	1273	3.40	2.246	2.272	2.150	-0.184	-0.127	-0.078	-0.054	-0.037	-0.023
AP3	Virgin	0	2.294	2.283	2.215	-	-	-	-	-	-
AP3	1243	1.58	2.338	2.272	2.191	+0.044	-0.011	-0.034	+0.028	-0.007	-0.022
AP4	Virgin	0	2.379	2.176	2.112	-	-	-	-	-	-
AP4	873	1.14	2.161	2.135	2.100	-0.218	-0.041	-0.012	-0.191	-0.036	-0.011
AP4	973	1.64	2.204	2.156	2.094	-0.175	-0.020	-0.018	-0.107	-0.012	-0.011
AP4	1073	2.11	2.170	2.135	2.104	0.205	0.041	0.008	-0.097	-0.019	-0.004

Table 13. Ultrasonic Velocities through AGLMP Graphite gasified in Carbon Dioxide.

Graphite Code	Weight loss/ %	Graphite	Original Graphite Block	Control Graphite Code
H24	8.8	BAEL Pitch Coke	D7	Q4/1 and Q5/4
C79	6.2	PGA	106A	C7/1 and C6/3
M38	3.7	AGLMP	10F49	P(10F49)
M28	3.5	AGLMP	584/195	O(584/195)
H30	0.6	BAEL Pitch Coke	D7	Q6/1

Table 14. Radiolytically Oxidised Graphite Samples and their Corresponding Controls.

	Pre-irradiation	Post-irradiation
Bulk Density/g cm^{-3}	1.848	1.714
Helium Density/g cm^{-3}	2.096	2.082
O.P.V./$cm^3(100\ cm^3)^{-1}$	11.8	17.6
O.P.V./$cm^3(100\ g)^{-1}$	6.4	10.3
C.P.V./$cm^3(100\ cm^3)^{-1}$	6.5	6.7
Surface area/$m^2 g^{-1}$	0.265	0.218

Table 15. Properties of Sample H.24, Before and After Radiolytic Oxidation to 8.8% Weight Loss.

	Pre-	Post-1.26%	Post-9.48%	Pre-	Post-22.6%
Bulk Density/g cm^{-3}	1.698	1.669	1.521	1.679	1.305
Helium Density/ g cm^{-3}	2.135	2.164	2.218	2.125	2.230
O.P.V./cm^3 $(100\ cm^3)^{-1}$	20.49	22.84	31.41	20.98	41.45
C.P.V./cm^3 $(100\ cm^3)^{-1}$	4.48	3.37	1.35	4.81	0.85
Viscous Flow Coefficient/ $10^{-13}\ m^2$	0.28	0.23	0.55	0.29	0.54
Slip Flow Coefficient/ 10^{-8} m	1.34	1.59	1.77	1.68	3.08
Diffusivity Ratio/10^{-3}	-	4.6	16.1	4.3	49.8

Table 16. Properties of Lima Graphite, Before and After Radiolytic Oxidation to 1.26%, 9.48% and 22.6% Weight Losses in the Presence of Methane.

Graphite	Total Porosity/% from U.K.A.E.A.	Quantimet Data					
		No. of fields	Porosity/ %	Mean Intercept/μm Pore	Wall	Perimeter /mm	Count
Q4/1	18.3	10	14.2	54.9	331.0	53.7	223
H24	24.3	10	23.9	63.8	203.5	77.8	227
C7/1	-	11	34.6	57.6	108.7	125.4	333
C79	-	9	51.8	72.6	78.1	137.1	148
10F49	19.9	15	19.4	61.4	255.9	63.7	245
M38	-	10	23.5	60.9	198.4	81.8	314
584/195	19.9	11	21.9	61.8	220.9	72.2	288
M28	-	10	25.3	60.0	177.1	88.0	354
Q6/1	-	9	13.8	46.2	288.8	63.2	309
H30	-	8	18.9	51.8	222.1	79.9	367
AGLMP							
Virgin	19.9	70	20.0	59.3	236.8	72.4	297
3.1%b.o	21.7	30	21.4	60.6	222.3	74.9	328
5.4%b.o	23.9	50	22.7	56.7	192.9	85.6	404
10.5%b.o	28.6	50	32.1	60.1	127.2	118.3	434

Table 17. Preliminary Data Obtained From Graphite Samples Using the Quantimet 720.

Sample	No. of fields	Porosity /%	Standard Deviation	Mean Intercept/μm		Standard Deviation		Perimeter /mm	Standard Deviation	No. of Counts per field	Total Counts/ (100 mm^2)-1
				Pore	Wall	Pore	Wall				
Q4/1	10	13.0	2.04	61.4	410.2	9.03	36.59	43.9	2.87	198	3331
H24	10	18.6	2.75	61.1	267.3	7.36	38.36	65.0	8.60	262	4409
C7/1	10	31.0	5.53	56.3	125.6	7.25	17.39	116.8	8.60	359	6031
C79	10	34.2	4.13	61.9	119.0	5.92	14.60	113.6	7.39	304	5113
10F49	15	14.5	2.34	59.5	350.1	4.65	57.17	52.0	6.71	230	3871
M38	10	19.1	1.88	59.9	254.1	4.29	23.79	66.6	4.54	282	4745
584/195	8/7	19.2	2.80	67.8	285.3	6.68	28.54	58.6	5.40	232	3901
M28	10	19.4	2.63	71.6	297.6	5.12	35.51	57.5	5.85	211	3540
Q6/1	9	10.1	1.68	51.5	459.3	7.22	56.34	41.9	4.25	221	3716
H30	10	9.3	1.15	52.0	508.0	4.63	68.83	37.4	4.36	181	3038
AGIMP											
Virgin	70	15.2	2.06	58.9	327.4	5.57	36.17	53.8	4.53	221	-
3.1%b.o	30	17.5	1.95	71.2	336.3	6.83	35.05	53.2	4.98	200	3370
5.4%b.o	50	16.3	2.92	63.7	327.7	8.75	49.40	54.1	5.49	238	4044
10.5%b.o	50	17.8	3.65	62.7	290.3	9.98	48.45	61.4	8.63	278	4944

Table 18. Field Data Obtained from Graphite Samples Using the Quantimet 720.

Samples	No. of features	Mean Perimeter /mm	Standard Deviation	Mean Area /mm^2	Standard Deviation	Feret's Diameter/μm		Standard Deviation		Shape Factor	Shape Factor $A/P2$	Standard Deviation
						Max	Mean	Max	Mean	max/mean		
Q4/1	85	1.32	0.08	0.046	0.004	429.0	338.9	23.61	17.46	1.266	0.029	0.001
H24	129	1.62	0.12	0.049	0.005	452.0	361.8	24.94	19.71	1.249	0.023	0.001
C7/1	227	2.53	0.25	0.060	0.007	457.8	375.8	18.11	15.19	1.218	0.019	0.002
C79	216	2.28	0.32	0.055	0.008	440.5	351.6	24.26	19.45	1.253	0.028	0.005
10F49	218	1.02	0.04	0.031	0.001	320.3	261.6	8.64	6.87	1.221	0.035	0.002
M38	185	1.13	0.04	0.033	0.002	353.3	286.0	10.75	7.95	1.234	0.030	0.001
584/195	122	1.39	0.11	0.048	0.005	394.2	319.7	19.39	14.32	1.231	0.031	0.001
M28	178	1.20	0.07	0.040	0.003	371.8	300.0	14.17	11.12	1.240	0.033	0.001
Q6/1	76	1.08	0.06	0.034	0.002	360.4	292.9	15.90	11.49	1.229	0.034	0.002
H30	75	1.14	0.06	0.035	0.003	378.3	301.2	17.12	13.03	1.256	0.033	0.002
AGLMP												
virgin	960	1.20	0.03	0.034	0.001	343.8	282.5	5.18	4.12	1.220	0.029	0.001
3.1%b.o.	477	1.30	0.04	0.041	0.002	367.1	300.3	8.58	6.39	1.223	0.030	0.001
5.4%b.o.	753	1.29	0.04	0.041	0.002	354.8	294.1	6.73	5.39	1.208	0.029	0.001
10.5%b.o.	727	1.40	0.05	0.042	0.002	370.9	304.3	7.39	5.81	1.220	0.027	0.001

Table 19. Feature Data Obtained from Graphite Samples Using the Quantimet 720.

Sample	No. of Fields	Porosity /%	Standard Deviation	Mean Intercept/µm Open Pores	Mean Intercept/µm Wall and Closed Pores	Standard Deviation Open Pores	Standard Deviation Wall and Closed Pores	Perimeter /mm	Standard Deviation
Q4/1	10	8.3	1.08	45.5	505.5	3.15	62.47	36.4	4.26
H24	7	9.5	2.67	49.1	466.1	14.34	90.01	38.1	7.06
C7/1	10	20.7	2.32	42.4	162.7	1.72	18.37	98.2	7.48
C79	10	21.6	1.77	44.0	159.6	1.46	13.68	98.3	7.20
10F49	9	10.3	1.25	59.6	519.3	4.24	49.09	34.4	2.63
M38	6	9.6	1.90	51.0	481.3	2.96	96.81	37.4	6.42
584/195	10	9.3	1.68	58.3	566.6	5.20	97.52	31.1	4.02
M28	9	8.1	1.50	56.4	639.1	4.53	163.04	28.0	5.80
Q6/1	9	6.2	1.47	41.9	631.7	6.43	222.20	29.1	8.05
H30	7	5.6	1.38	42.4	716.9	5.46	103.54	26.0	3.51

Table 20. Field Data Obtained From Gold Impregnated Graphite Samples Using the Quantimet 720.

Eqivalent circle diameter /μm	Number/ $(100\ mm^2)^{-1}$
10.2	70.9
12.1	196.4
14.3	155.2
17.0	187.0
20.1	269.0
23.7	350.7
28.1	314.7
33.2	293.4
39.3	291.3
46.5	256.8
55.0	251.5
65.0	190.5
76.9	141.9
91.0	95.4
107.7	64.7
127.4	56.5
150.7	40.8
178.2	22.5
210.9	16.8
249.5	21.9
295.1	25.4
349.1	8.1
413.0	8.1
488.6	1.6
578.0	1.4
683.8	0.0
808.9	0.0
956.9	0.0
1132.0	0.0
1339.2	0.0
1584.2	0.0
1874.2	0.0
2217.1	0.0

Table 21. Corrected Differential Distribution of Areas of Pores for BAEL Pitch Coke Graphite Q4/1 (Control for H24).

Eqivalent circle diameter /μm	Number/ (100 mm^2)$^{-1}$
10.2	116.1
12.1	283.2
14.3	190.6
17.0	300.9
20.1	263.3
23.7	401.3
28.1	443.8
33.2	410.4
39.3	393.4
46.5	370.8
55.0	272.4
65.0	231.4
76.9	198.0
91.0	145.4
107.7	113.7
127.4	87.2
150.7	60.4
178.2	32.8
210.9	42.0
249.5	26.7
295.1	11.9
349.1	13.0
413.0	4.9
488.6	11.4
578.0	4.3
683.8	0.0
808.9	0.0
956.9	0.0
1132.0	0.0
1339.2	0.0
1584.2	0.0
1874.2	0.0
2217.1	0.0

Table 22. Corrected Differential Distribution of Areas of Pores for BAEL Pitch Coke Graphite H24, Radiolytically Oxidised to 8.8% Weight Loss.

Size/ µm	Distribution of maximum Feret's diameters	Distribution of mean Feret's diameters
10.0	0	0
12.0	0	0
14.4	0	0
17.3	0	0
20.8	0	0
25.0	0	0
30.0	0	0
36.1	0	0
43.3	0	0
52.1	0	0
62.5	0	0
75.1	1	1
90.2	0	0
108.4	0	0
130.2	0	0
156.4	2	6
187.9	6	16
225.7	12	16
271.1	16	11
325.6	9	9
391.1	10	10
469.8	11	5
564.3	5	8
677.9	6	2
814.3	6	1
978.1	1	0
1174.9	0	0
1411.3	0	0
1695.2	0	0
2036.3	0	0
2446.0	0	0
2938.2	0	0
3529.3	0	0

Table 23. Distribution of Feret's Diameters in BAEL Pitch Coke Graphite Q4/1 (Control for H24).

Size /μm	Distribution of maximum Feret's diameters	Distribution of mean Feret's diameters
10.0	1	0
12.0	0	0
14.4	0	1
17.3	0	0
20.8	1	0
25.0	0	0
30.0	0	0
36.1	0	0
43.3	0	0
52.1	0	0
62.5	0	0
75.1	0	1
90.2	0	0
108.4	0	0
130.2	1	0
156.4	0	2
187.9	3	16
225.7	13	37
271.1	33	24
325.6	27	14
391.1	15	12
469.8	11	3
564.3	4	7
677.9	7	3
814.3	4	4
978.1	3	2
1174.9	4	2
1411.3	2	0
1695.2	0	0
2036.3	0	0
2446.0	0	0
2938.2	0	0
3529.3	0	0

Table 24. Distributions of Feret's Diameters in BAEL Pitch Coke Graphite H24, Radiolytically Oxidised to 8.8% Weight Loss.

Equivalent circle diameter /μm	Number/ (100 mm^2)$^{-1}$
10.2	141.3
12.1	210.1
14.3	209.4
17.0	252.2
20.1	256.4
23.7	253.7
28.1	263.9
33.2	242.8
39.3	238.3
46.5	201.7
55.0	175.2
65.0	181.0
76.9	141.3
91.0	132.3
107.7	119.5
127.4	104.4
150.7	72.4
178.2	66.8
210.9	45.9
249.5	36.6
295.1	24.9
349.1	9.7
413.0	7.6
488.6	1.6
578.0	1.9
683.8	0.7
808.9	0.0
956.9	0.0
1132.0	0.0
1339.2	0.0
1584.2	0.0
1874.2	0.0
2217.1	0.0

Table 25. Corrected Differential Distribution of Areas of Pores for AGLMP Graphite Thermally Oxidised to 3.1% Weight Loss.

Equivalent circle diameter /μm	Number/ (100 mm^2)-1
10.2	219.8
12.1	359.8
14.3	307.1
17.0	383.8
20.1	368.5
23.7	348.6
28.1	312.5
33.2	288.5
39.3	245.1
46.5	227.9
55.0	185.7
65.0	157.7
76.9	145.4
91.0	120.2
107.7	114.5
127.4	93.2
150.7	75.8
178.2	59.3
210.9	36.6
249.5	32.0
295.1	18.1
349.1	9.5
413.0	6.2
488.6	3.0
578.0	0.6
683.8	0.8
808.9	0.0
956.9	0.3
1132.0	0.0
1339.2	0.0
1584.2	0.0
1874.2	0.0
2217.1	0.0

Table 26. Corrected Differential Distribution of Areas of Pores for AGLMP Graphite, Thermally Oxidised to 5.4% Weight Loss.

Equivalent circle diameter /μm	Number/ $(100\ mm^2)^{-1}$
10.2	247.0
12.1	439.4
14.3	417.0
17.0	475.9
20.1	484.1
23.7	447.2
28.1	417.7
33.2	374.1
39.3	307.0
46.5	281.2
55.0	213.1
65.0	185.4
76.9	150.3
91.0	138.7
107.7	113.7
127.4	85.9
150.7	76.1
178.2	63.3
210.9	45.7
249.5	25.4
295.1	19.4
349.1	13.0
413.0	6.5
488.6	4.9
578.0	2.3
683.8	1.6
808.9	0.3
956.9	0.0
1132.0	0.0
1339.2	0.0
1584.2	0.0
1874.2	0.0
2217.1	0.0

Table 27. Corrected Differential Distribution of Areas of Pores for AGLMP Graphite, Thermally Oxidised to 10.5% Weight Loss.

Element	X-ray energy/kev
Aluminium	1.486
Silicon	1.739
Sulphur	2.307 (2.322)
Chlorine	2.621 (2.631)
Potassium	3.312 (3.589)
Calcium	3.690 (4.012)
Iron	6.398 (7.057)
Nickel	7.471 (8.263)

Table 28. X-ray Emission Energies.

Graphite	Sample Code	Linear Growth/ %
BAEL VQMB (NM)	Control	0
(Pitch-coke	LZAA	- 1.99
	SBO	+ 3.01
AGLMP	Control	0
(Gilso-carbon (NA))	FRC	- 0.00
	HAB	+ 4.0

Table 29. Details of Irradiated Graphite Samples.

	Area of Gilso-Carbon Graphite		Area of Other Graphite	
	Pores/ %	Pore Walls/ %	Pores/ %	Pore Walls/ %
1st Direction	2.50	20.50	18.50	58.5
2nd Direction	2.45	22.60	20.75	54.2
3rd Direction	3.55	26.30	17.75	52.4

Table 30. Point-Counting Data on AGLMP Graphite.

Polish	Depth removed/μm	
	AGLMP Graphite	VQMB Graphite
After 1st	5.5	5.5
" 2nd	4.5	4.5
" 3rd	9.0	9.0
" 4th	10.0	10.0
" 5th	9.0	9.0
" 6th	5.5	5.5
" 7th	10.0	10.0
" 8th	5.0	5.0
" 9th	11.0	11.0
Total removed	71.5	69.5

Table 31. Depth of Graphite Removed After Each Polish.

No. of Polishes	AGLMP Graphite				VQMB Graphite			
	Area A1		Area A2		Area V1		Area V2	
	x/ µm	y/ µm	x/ µm	y/ µm	x/ µm	y/ µm	x/ µm	y/ µm
3	1,099	86	1,231	97	3,408	1,104	1,209	38
4	1,089	80	1,286	90	3,348	1,092	1,153	25
5	1,080	72	1,224	82	3,361	1,096	1,166	31
6	1,087	65	1,230	72	3,334	1,094	1,142	25
7	1,100	82	1,232	92	3,336	1,100	1,141	33
8	1,109	75	1,243	86	3,347	1,081	1,154	17
9	1,118	73	1,255	81	3,330	1,092	1,142	29
10	980	76	1,232	83	3,347	1,090	1,152	25

Table 32. Distance of Each Photo-montage from the Notch on the Samples.